SERPENTINIZATION-ASSISTED DEFORMATION PROCESSES AND

CHARACTERIZATION OF HYDROTHERMAL FLUXES AT MID-OCEAN RIDGES

A Dissertation
Presented to
The Academic Faculty

By

Gence Genc

In Partial Fulfillment
Of the Requirements for the Degree
Doctor of Philosophy in the
School of Civil and Environmental Engineering

Georgia Institute of Technology

May 2012

SERPENTINIZATION-ASSISTED DEFORMATION PROCESSES AND

CHARACTERIZATION OF HYDROTHERMAL FLUXES AT MID-OCEAN RIDGES

Approved by:

Dr. Leonid N. Germanovich, Advisor
School of Civil and Environmental Engineering
Georgia Institute of Technology

Dr. Haiying Huang
School of Civil and Environmental Engineering
Georgia Institute of Technology

Dr. Robert P. Lowell
Department of Geosciences
Virginia Polytechnic Institute and State University

Dr. Philip J. Roberts
School of Civil and Environmental Engineering
Georgia Institute of Technology

Dr. Daniela Di Iorio
Department of Marine Sciences
University of Georgia

Dr. Josef Dufek
School of Earth and Atmosmepheric Sciences
Georgia Institute of Technology

Date Approved: April 2, 2012

To my babişko

ACKNOWLEDGEMENTS

I would like to express my gratitude to my advisor Dr. Leonid N. Germanovich and Dr. Robert P. Lowell for their patience, enthusiastic support, and guidance throughout this study.

I also would like to thank my thesis committee members: Dr. Daniela Di Iorio, Dr. Haiying Huang, Dr. Philip J. Roberts, and Dr. Josef Dufek for their advice and contributions.

I would like to extend my thanks to Dr. Scott Wankel, Dr. Peter Girguis at the Harvard University, Dr. Peter Rona at the Rutgers University for valuable advice and discussions; Robert S. Hurt at the Georgia Institute of Technology, for his invaluable help in the design, fabrication and calibration of heat flow measuring devices.

This study was supported by the National Science Foundation, NSF OCE 0937057 and 1131355. This support is gratefully acknowledged.

I would like to present my deepest thanks to my mother Halise Genc, and my brother Sinan Genc for their unconditional love and continuous support during all hard days of life abroad and this scientific journey. Your existence on my left shoulder even away from home has been the sole reason of my academic motivation. Thanks for being the best family of the entire Middle East! Thanks are also due to my dear friends who have made my life in Atlanta enjoyable and cheerful: *Gulum*, my cute little genius for being an impeccable “elder sister”, and always a serious hope to my fuzzy problems; *Sabi* for providing constant fun-filled BFF time together and a fabulous bud smile which

melts my stress right away, *Hansel* and *Gretel* for serving a “second home”, tasteful long nights (it was well worth for 7 extra pounds), never-ending conversations on the meditation sofa, and an unforgettable company to us; *Nazli* for a little too long afternoon chats, and opening the doors of your delightful friendship, and last but not least to *Esra*, *Mehtap*, *Necmi*, *Baris*, *Ibrahim*, *Safak*, and *Mike* in addition to friends (*Dr*. *Halil Ceylan*) and relatives elsewhere in the world (the *Celik*’s, the *Sunay*’s, *Totosum*, *Gamzem*, the *Unuvar*’s and the *Hatipoglu*’s) and my previous mentors in my home country (*Dr*. *Vedat Doyuran*, *Dr*. *Ufuk Ergun*, and *Dr*. *Kemal Onder Cetin*) who have always supported me.

Last, but not the least, I do not think I can thank enough my husband, my best-friend and my home-overseas, Onur Celik for his full interest in my ever-sustainable mood and often not so fun life, for the incredible motivation he provided me during those days when I felt miserably lost, and for the joy of “life together” he has given whole heartedly from the day we first met till the last push. Thank you zillions of times for your full-time job of being by my side no matter where and how I stand and believing in what I can achieve more than I believed in what I can do. Trust me, without him neither this dissertation nor me would ever be complete!

TABLE OF CONTENTS

LIST OF TABLES

LIST OF FIGURES

SUMMARY

Seafloor hydrothermal systems play a significantly important role in Earth's energy and geochemical budgets and support the existence and development of complex biological ecosystems by providing nutrient and energy to microbial and macrafaunal ecosystems through geochemical fluxes. Heat output and fluid flow are key parameters which characterize hydrothermal systems at oceanic spreading centers by constraining models of hydrothermal circulation. Although integrated measurements of heat flux in plumes are critically important as well, quantification of heat flux at discrete sources (vent orifices versus patches of seafloor shimmering diffuse flow) from direct measurements is particularly essential for examining the partitioning of heat flow into focused and diffuse components of venting and determining geochemical fluxes from these two modes of flow. Hydrothermal heat output also constrains the permeability of young oceanic crust and thickness of the conductive boundary layer that separates magmatic heat source from overlying hydrothermal circulation. This dissertation will be fundamentally focused on three main inter-connected topics: (1) the design and development of direct high- or low-temperature heat flow measuring devices for hydrothermal systems, (2) the collection of new heat output results on four cruises between 2008 and 2010 at several distinct hydrothermal sites along mid-ocean ridges (MORs) to estimate total heat output from individual vent structures such as Dante, Hulk or the whole vent field (e.g., Main Endeavour Vent Field (MEF)), the partitioning between focused and diffuse hydrothermal venting in MEF, and determination of initial estimates of geochemical flux from diffuse hydrothermal fluids which may be influenced

by the activity in subsurface biosphere and finally (3) the deformation and uplift associated with serpentinization at MORs and subduction zones.

Despite extensive efforts spent for the last couple of decades on heat flow measurement methods and techniques either in the plumes or right at sources, there is still limited knowledge of direct estimates of heat discharge particularly at the vent scale and reliable estimates of temporal variation in heat flux. Moreover, a few previously used tools to make discrete measurements were associated with mechanical complications and/or problems mostly related to electronics or irrecoverable damage due to environmental problems such as accumulation of sediments/particles from hydrothermal fluids. In this dissertation we showed the stages of design, fabrication, calibration and in-situ deployment from DSV Alvin for two unique heat flow measuring seafloor instruments; cup anemometer and turbine flow meter. The devices have proven to be robust, practical, and simple to maneuver and perform in both focused and diffuse flow milieus. Field experiments showed that these self-contained devices yielded a broad range of accurate heat flow estimates ranging from 2 cm/s to 200 cm/s with minimum required maintenance and much less on-station time compared to previous designs.

This dissertation reports 63 successful point measurements of focused and diffuse fluid flow the majority of which were completed at the Main Endeavour, High Rise and Mothra hydrothermal vent fields along Endeavour Segment of Juan de Fuca Ridge. By coupling a fraction of our flow rate results with geochemical data (i.e. fluid

volatile concentrations) collected with in-situ mass spectrometer, direct geochemical flux were estimated from both focused and diffuse flows.

Heat and fluid flow results we have obtained complement our understanding of serpentinization assisted deformation processes at Mid-Ocean Ridges and subduction zones. This dissertation also includes a simple mathematical model developed for crustal deformation and seafloor uplift resulting from volume expansion associated with subsurface serpentinization. Application of this model shows the apparent deformation at the central portion of the east wall of the axial valley at the TAG hydrothermal field and the Quaternary uplift of the Miyazaki Plain observed above the Kyushu-Palau subduction zone in the western Pacific. Our model suggests that observed topographic anomaly may have been produced in a relatively deep-seated region of serpentinized mantle associated with a volume expansion (transformation strain) of 20 to 40% that could have possibly resulted into fracturing/faulting processes or only with 3% of transformation strain respectively.

CHAPTER 1

INTRODUCTION

The flow of aqueous fluids in the oceanic crust has major impacts on Earth's thermal, biogeochemical, and tectonic processes. At oceanic spreading centers, where new oceanic crust and lithosphere are created, hydrothermal processes transport ~25% of Earth's total heat loss [*Williams and Von Herzen,* 1974; *Sclater et al.,* 1980; *Stein and Stein,* 1994; *Elderfield and Schultz,* 1996], cycle chemical constituents between the ocean and lithosphere [e.g., *Wolery and Sleep,* 1976], and supply nutrients to a variety of microbial and macrofaunal biological communities [e.g., *Jannasch,* 1995; *Kelley et al.,* 2002; *Shank et al.,* 1998]. The global impact of these processes has suggested a potential link between hydrothermal systems and the origin of life on Earth [e.g., *Baross and Hoffman,* 1985; *Miller et al.,* 1995; *Imai et al.,* 1999].

As seawater circulates through the permeable rocks in young oceanic crust, it is heated by subsurface magma to temperatures of ~400° C. Along its flow path the heated seawater undergoes a number of water-rock reactions resulting in a chemically altered hydrothermal fluid. This low density hot, buoyant hydrothermal fluid then rises toward to seafloor where it discharges through focused chimneys as mineral-laden "black smokers" of ~350° C [*Macdonald et al.,* 1980; *Spiess et al.,* 1980]. In addition, the hot hydrothermal fluid may mix with seawater in the shallow crust resulting in the discharge of low-temperature diffuse flows. These diffuse fluid flows provide nutrients

for extensive microbial ecosystems within the shallow crust as well as for a variety of macrofaunal ecosystems on the seafloor. **Figure 1.1a** illustrates the hydrothermal circulation process conceptually; **Figures 1.1b** and **1.1c** show a photograph of a black smoker vent and a diffuse flow site hosting a tube worm community, respectively.

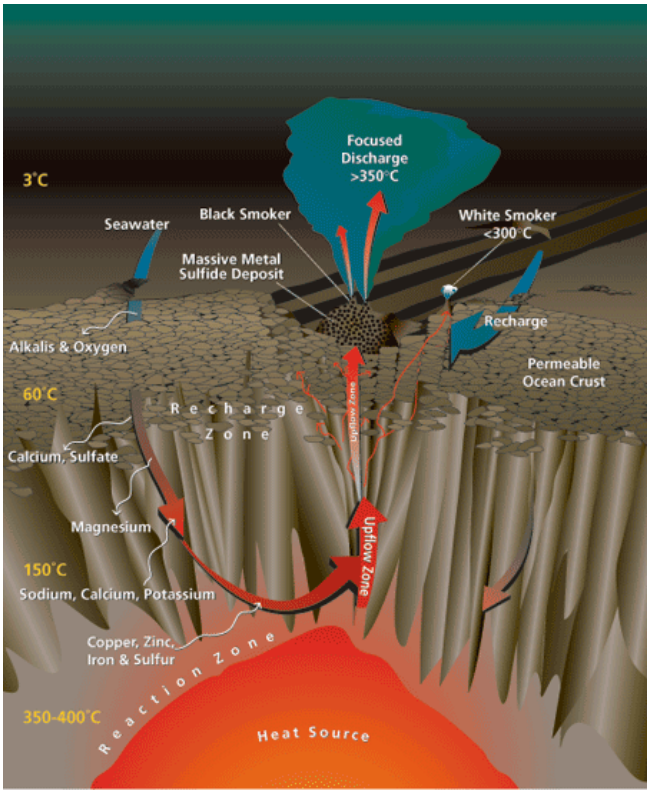

(a)

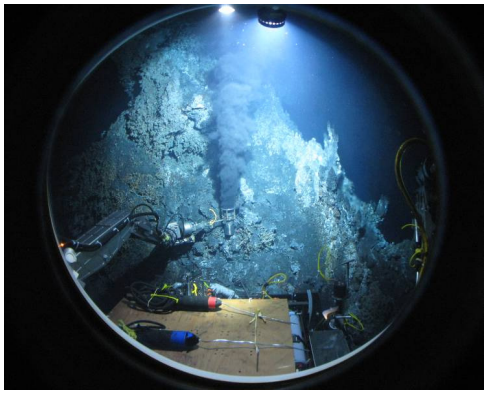

(b)

(c)

Figure 1.1 (a) Hydrothermal circulation system in the oceanic crust at mid-ocean ridges **(b)** black smoker chimneys and **(c)** a diffuse flow site surrounded by biological communities (tube worms). Pictures taken respectively during the June 2009 and July 2010 expeditions (AT15-47 & 15-67) to Juan de Fuca Ridge.

Fluid flow and advective heat output data at oceanic spreading centers are critically important for understanding the physical, geochemical, and biological behavior of seafloor hydrothermal systems and to determine energy and biogeochemical fluxes through the crust to the ocean [*Butterfield et al.,* 2004; *Von Damm and Lilley,* 2004;

Wankel et al., 2011]. Heat output data also provide important constraints on models of magma-driven hydrothermal systems [*Lowell and Germanovich,* 2004; *Lowell et al.,* 2008; *Lowell,* 2010]. Nevertheless these data are available at a very limited number of hydrothermal vent fields [*Baker,* 2007; *Lowell et al.,* 2008], and even fewer studies have addressed the partitioning of heat output between focused and diffuse flow [e.g., *Rona and Trivett,* 1992; *Schultz et al.,* 1992; *Ramondenc et al.,* 2006; *Veirs et al.,* 2006], which is important for constraining geochemical fluxes and biogeochemical processes in the shallow crust.

The next two Chapters of this thesis advance the science of fluid flow and advective heat output measurements in seafloor hydrothermal systems. Each chapter is written in the format of a manuscript which has been submitted for publication, or will be submitted in the near future; consequently each chapter has its own introduction and list of references.

Chapter 2 describes the development, calibration, and field testing of cup anemometer and turbine flow meters to measure instantaneous rates of fluid flow, at depths up to 5,000 m and temperatures as high as 450° C. Both types of device can be deployed from a manned submersible or from a remotely operated vehicle (ROV) and can measure fluid flow at both focused and diffuse flow sites on the seafloor. A key feature of the turbine flow meters is the open bearing design that eliminates potential clogging by precipitates/particles, which are often encountered at hydrothermal vent environments. It is hoped that such devices become a part of the deep sea arsenal of tools so that measurements of fluid flow and advective heat output at seafloor

hydrothermal sites becomes routine. The development stages of design, instrumentation and calibration of these heat flow measuring devices and the results obtained using these instruments are presented and discussed by *Germanovich et al*. [2012a].

Chapter 3 reports 63 fluid flow and heat flux estimates from various vent orifices and diffuse flow sites on the Endeavour segment of the Juan de Fuca Ridge (JdF). The data were collected between July 2008 and July 2010 from Deep Submergence Vehicle (DSV) *Alvin* with the devices described in Chapter 2. Most of these data were obtained at large sulfide structures in the northern end of the Main Endeavour Field (MEF) but also at Mothra and High Rise vent fields. Not only do we determine the high-temperature focused heat output at individual structures (e.g, Dante, Hulk, Faulty Towers) but we also extrapolate the estimated heat output to the entire hydrothermal filed (e.g., MEF, High Rise) and we argue that the high-temperature heat output of the system may be declining since the 1999 eruption at MEF [*Lilley et al.,* 2003]. A fraction of the results from our broadly collected heat-flow data and an estimate on heat output from Dante vent structure are published on *Di Iorio et al*. [2012]. We also report the first estimates in the High Rise and Mothra hydrothermal vent fields. Although the data from High Rise are limited, they suggest that heat output from High Rise may be higher than that from MEF. Finally, we describe the results of a collaborative study to obtain fluxes of volatile compounds such as H_2, CH_4 and $CO_{2(aq)}$ from focused and diffuse flows in the MEF and Mothra vent fields by combining fluid flow measurements with geochemical data collected using the In Situ Mass Spectrometer [e.g., *Bell et al*., 2007; *Camilli and*

Duryea, 2009; *Wankel et al*., 2010]. These first direct estimates of geochemical flux suggest that geochemical flux from diffuse flow systems can constitute approximately half of the net geochemical flux. Above mentioned results, used *in-situ* tools (e.g., mass spectrometer, flow meter) and associated methods are described by *Wankel et al.* [2011].

In addition to magma-driven hydrothermal processes, serpentinization of peridotite may also be an important process, particularly along slow-spreading oceanic spreading centers [e.g., *Carlson and Miller,* 1997; *Escartin et al.,* 2001]. The reaction of seawater with peridotite gives rise to different vent fluid chemistry, and the exothermic nature of the serpentinization reaction may provide an additional heat source to drive the circulation [*Lowell and Rona,* 2002; *Lowell,* 2010]. Moreover, because serpentinization reactions generally result in volume expansion of ~25 to 53% [*Coleman,* 1971; *O'Hanley,* 1992], large scale serpentinization may result is significant structural deformation and uplift. The formation of oceanic core complexes at slow spreading oceanic plate boundaries which have a limited supply of upwelling magma and associated detachment faults is often associated with serpentinization reactions [e.g., *Francis,* 1981; *Zonenshain et al.,* 1989; *Bougault et al.,* 1993; *Cann et al.,* 1997; *Tucholke et al.,* 1998; *Escartin and Hirth,* 1997; *Escartin et al.,* 2001; *Blackman et al.,* 2002; *Mével,* 2003; *Boschi et al.,* 2006; *Ildefonse et al.,* 2007; *Macleod et al.,* 2009; *Miranda and Dilek,* 2010]. Serpentinization and associated structural deformation may also be important at rifted margins [e.g., *Reston,* 2009], the ocean-continent transition zones [e.g., *Skelton*

and Jakobsson, 2007], and subduction zones [e.g., *Faccenda et al.,* 2008; *Tahara et al.,* 2008; *Hilairet and Reynard,* 2009].

Despite the extensive distribution of serpentinites and its important role in crustal deformation, quantitative models of the process are scarce. Chapter 4 of this dissertation focuses on the mathematical modeling of the structural deformation and uplift associated with subsurface serpentinization of variously shaped and inclined inclusions, by considering the classic problem of an inclusion undergoing uniform transformation strain in an elastic half-space. By using scaling analysis for simple inclusion shapes (e.g., cylinder, sphere) and closed-form solutions for a more general case of elliptical inclusions with various orientation and aspect ratio, we show that surface uplift is insensitive to the shape of the intrusion provided its depth is greater than ~1.5 times the radius of the inclusion. We apply this model to the Trans-Atlantic Geotraverse (TAG) hydrothermal field on the Mid-Atlantic Ridge (MAR) and to the Miyazaka Plain above the Kyushu-Palau subduction zone in the western Pacific. At the TAG hydrothermal field, an anomalous topographic high of 100 m is located in the central portion of the eastern axial valley wall, and projects ~3.5 km westward into the axial valley [*Rona et al.*, 1993]. Our model suggests that the observed uplift may result from a relatively deep-seated serpentinized body undergoing a transformational strain of 20 to 40%. At the Miyazaki Plain, crustal uplift of ~120 m during the past ~1.2×10^5 years [*Nagaoka et al.,* 1991; *Tahara et al.,* 2008] may be explained by the volume expansion associated with serpentinization of the mantle peridotites by using the full

elliptical solution although the transformational strain may only be 3%. This chapter is based on the paper of *Germanovich et al.,* [2012b].

1.1 References

Baker, E.T. (2007), Hydrothermal cooling of mid-ocean ridge axes: Do measured and modeled heat fluxes agree?, *Earth and Planetary Science Letters, 263*(1-2), 140−150.

Baross, J.A., and S.E. Hoffman (1985), Submarine hydrothermal vents and associated gradient environments as sites for the origin and evolution of life, *Origins of Life, 15,* 327−345.

Bell, R.J., R.T. Short, F.H.W. van Amerom, and R.H. Byrne (2007), Calibration of an in situ membrane inlet mass spectrometer for measurements of dissolved gases and volatile organics in seawater, *Environmental Science and Technology, 41*(23), 8123−8128.

Blackman, D.K., J.A. Karson, D.S. Kelley, J.R. Cann, G.L. Früh-Green, J.S. Gee, S.D. Hurst, B.E. John, J. Morgan, S.L. Nooner, D.K. Ross, T.J. Schroeder, and E.A. Williams (2002), Geology of the Atlantis Massif (Mid-Atlantic Ridge, 30 degrees N): Implications for the evolution of an ultramafic oceanic core complex, *Marine Geophysical Researchers, 23,* 443−469.

Boschi C., G.L. Früh-Green, A. Delacour, J.A. Karson, D.S. Kelley (2006), Mass transfer and fluid flow during detachment faulting and development of an oceanic core complex, Atlantis Massif (MAR 30°N), *Geochemistry Geophysics Geosystems, 7,* 1−39.

Bougault, H., J.L. Charlou, Y. Fouquet, H.D. Needham, N. Vaslet, P. Appriou, P.J. Baptiste, P.A. Rona, L. Dmitriev, and S. Silantiev (1993), Fast and slow spreading ridges: Structure and hydrothermal activity, ultramafic topographic highs, and CH4 output, *Journal of Geophysical Research, 98*(B6), 9643−9651.

Butterfield, D.A., K.K. Roe, M.D. Lilley, J.A. Huber, J.A. Baross, R.W. Embley and G.J. Massoth (2004), Mixing, reaction and microbial activity in the sub-seafloor revealed by temporal and spatial variation in diffuse flow vents at Axial Volcano, *Geophysical Monograph, 144,* 269−289.

Camilli, R., and A.N. Duryea (2009), Characterizing spatial and temporal variability of dissolved gases in aquatic environments with in situ mass spectrometry, *Environmental Science and Technology, 43*(13), 5014−5021.

Cann, J.R., D.K. Blackman, D.K. Smith, E. McAllister, B. Janssen, S. Mello, E. Averinos, A.R. Pascoe, and J. Escartin (1997), Corrugated slip surfaces formed at ridge-transform intersections on the Mid-Atlantic Ridge, *Nature, 385,* 329−332.

Carlson, R.L., and D.J. Miller (1997), A new assessment of the abundance of serpentinite in the oceanic crust, *Geophysical Research Letters, 24,* 457−460.

Coleman, R.G. (1971), Petrologic and geophysical nature of serpentinites, *Geol. Soc. Amer. Bull., 82,* 918−987.

Di Iorio, D., J.W. Lavelle, P.A. Rona, K. Bemis, G. Xu, L.N. Germanovich, R.P. Lowell, and G. Genc (2012), Measurements and models of heat flux and plumes from hydrothermal discharges near the deep sea floor, *Oceanography, 25*(1), 169-179.

Elderfield, H., and A. Schultz (1996), Mid-ocean ridge hydrothermal fluxes and the chemical composition of the ocean, *Annual Review of Earth and Planetary Sciences, 24,* 191−224.

Escartin, J., G. Hirth, and B. Evans (1997), Nondilatant brittle deformation of serpentinites: Implications for Mohr-Coulomb theory and the strength of faults, *Journal of Geophysical Research, 102*(B2), 2897−2913.

Escartin, J., G. Hirth, and B. Evans (2001), Strength of slightly serpentinized peridotites: Implications for the tectonics of oceanic lithosphere, *Geology, 29,* 1023−1026.

Faccenda, M., L. Burlini, T.V. Gerya, and D. Mainprice (2008), Fault-induced seismic anisotropy by hydration in subducting oceanic plates, *Nature, 455*(7216), 1097−1100.

Francis, T.J.G. (1981), Serpentinization faults and their role in the tectonics of slow spreading ridges, *J. Geophys. Res., 86,* 11612−11622.

Germanovich, L.N., R.S. Hurt, G. Genc, and R.P. Lowell (2012a), Measuring fluid flow in seafloor hydrothermal environments (submitted to *J. Geophys. Res*.).

Germanovich, L.N., G. Genc, R.P. Lowell, and P.A. Rona (2012b), Deformation and surface uplift associated with serpentinization at mid-ocean ridges and subduction zones, *J. Geophys. Res.,* in press.

Hilairet N., B. Reynard (2009), Stability and dynamics of serpentinite layer in subduction zone, *Tectonophysics, 465,* 24−29.

Ildefonse, B., D.K. Blackman, B.E. John, Y. Ohara, D.J. Miller, and C.J. MacLeod (2007), Oceanic core complexes and crustal accretion at slow-spreading ridges, *Geology, 35,* 623−626.

Imai E., H. Honda, K. Hatori, A. Brack, and K. Matsuno (1999), Elongation of oligopeptides in a simulated submarine hydrothermal system, *Science, 283,* 831−833.

Jannasch, H.W. (1995), Microbial interactions with hydrothermal fluids, *Geophysical Monograph-American Geophysical Union, 91,* 273−296.

Kelley, D.S., J.A. Baross, and J.R. Delaney (2002), Volcanoes, fluids, and life at Mid-Ocean Ridge spreading centers, *Annual Review of Earth and Planetary Sciences, 30*(1), 385−491.

Lilley, M.D., D.A. Butterfield, J.E. Lupton, E.J. Olson (2003), Magmatic events can produce rapid changes in hydrothermal vent chemistry, *Nature, 422,* 878−881.

Lowell, R.P. (2010), Hydrothermal systems at slow-spreading ridges: Analysis of heat sources and heat transfer processes, in diversity of hydrothermal systems on slow spreading ridges, *Geophysical Monograph, 188,* 11−26.

Lowell, R.P., and P.A. Rona (2002), Seafloor hydrothermal systems driven by sepentinization of peridotite, *Geophys. Res. Letters, 29*(11), 21−26.

Lowell, R.P., and L.N. Germanovich (2004), Hydrothermal processes at mid-ocean ridges: Results from scale analysis and single-pass models, *Geophysical Monograph, 148,* 219−244.

Lowell, R.P., B.W. Crowell, K.C. Lewis, and L. Liu (2008), Modeling multiphase, multicomponent processes at oceanic spreading centers, *Magma to Microbe: Modeling Hydrothermal Processes at Ocean Spreading Centers, 178,* 15−44.

Macdonald, K.C., K. Becker, F.N. Spiess, and R.D. Ballard (1980), Hydrothermal heat flux of the "black smoker" vents on the East Pacific Rise, *Earth Planet. Sci. Lett., 48,* 1−7.

Macleod, C.J., R.C. Searle, B.J. Murton, J.F. Casey, C. Mallows, S.C. Unsworth, K.L. Achenbach, and M. Harris (2009), Life cycle of oceanic core complexes, *Earth and Planetary Science Letters, 287,* 333−344.

Mével, C. (2003), Serpentinization of abyssal peridotites at mid-ocean ridges, *Comptes Rendus Geoscience, 335,* 825−852.

Miller, S.L., and A. Lazcano (1995), The origin of life - did it occur at high temperatures?, *Journal of Molecular Evolution, 41,* 689−692.

Miranda, E.A., and Y. Dilek (2010), Oceanic Core Complex development in modern and ancient oceanic lithosphere: Gabbro-localized versus peridotite-localized detachment models, *Journal of Geology, 118,* 95−109.

Nagaoka, S., H. Maemoku, and Y. Matsushima (1991), Evolution of Holocene coastal landforms in the Miyazaki Plain, Southern Japan, *Quat. Res. (Jpn.), 30,* 59−78.

O'Hanley, D.S. (1992), Solution to the volume problem in serpentinization, *Geology, 20,* 705−708.

Reston, T.J. (2009), The structure, evolution, and symmetry of the magma-poor rifted margins of the North and Central Atlantic: A synthesis, *Tectonophysics, 468,* 6−27.

Ramondenc, P., L.N. Germanovich, K.L. Von Damm, and R.P. Lowell (2006), The first measurements of hydrothermal heat output at 9°50'N, East Pacific Rise, *Earth and Planetary Science Letters, 263,* 140−150.

Rona, P.A., and D.A. Trivett (1992), Discrete and diffuse heat transfer at ASHES vent field, Axial Volcano, Juan de Fuca Ridge, *Earth and Planetary Science Letters, 109,* 57−71.

Rona, P.A., M.D. Hannington, C.V. Raman, and G. Thompson (1993), Active and relict seafloor hydrothermal mineralization at the TAG hydrothermal field, Mid-Atlantic Ridge, *Econ. Geology, 88,* 1989−2017.

Schultz, A., J.R. Delaney, and R.E. McDuff (1992), On the partitioning of heat flux between diffuse and point source seafloor venting, *Journal of Geophysical Research, 97*(B9), 12299−12314.

Sclater, J.G., C. Jaupert, and D. Galson (1980), The heat flow through oceanic and continental crust and the heat loss of the Earth, *Reviews in Geophysics, 18,* 269−311.

Shank, T.M., D.J. Fornari, K.L. Von Damm, M.D. Lilley, R.M. Haymon, and R.A. Lutz (1998), Temporal and spatial patterns of biological community development at nascent deep-sea hydrothermal vents (9°50'N, East Pacific Rise), *Deep-Sea Research Part II, 45*(1-3), 465−515.

Skelton, A., and M. Jakobsson (2007), Could peridotite hydration reactions have provided a contributory driving force for Cenozoic uplift and accelerated subsidence along the margins of the North Atlantic and Labrador Sea?, *Norwegian Journal of Geology, 87,* 21−28.

Spiess, F.N., et al. (1980), East Pacific Rise: Hot Springs and Geophysical Experiments, *Science, 207,* 1421−1433.

Stein, C.A., and S. Stein (1994), Constraints on hydrothermal heat flux through the oceanic lithosphere from global heat flow, *Journal of Geophysical Research, 99,* 3081−3095.

Tahara, M., K. Uehira, H. Shimizu, M. Nakada, T. Yamada, K. Mochizuki, M. Shinohara, M. Nishino, R. Hino, and H. Yakiwara (2008), Seismic velocity structure around the Hyuganada region, Southwest Japan, derived from seismic tomography using land and OBS data and its implications for interplate coupling and vertical crustal uplift, *Physics of the Earth and Planetary Interiors, 167,* 19−33.

Tucholke, B.E., J. Lin, M.C. Kleinrock (1998), Megamullions and mullion structure defining oceanic metamorphic core complexes on the mid-Atlantic ridge, *Journal of Geophysical Research-Solid Earth, 103,* 9857−9866.

Veirs, S.R., R.E. McDuff, and F.R. Stahr (2006), Magnitude and variance of near-bottom horizontal heat flux at the Main Endeavour hydrothermal vent field, *Geochemistry Geophysics Geosystems, 7,* 1−16.

Von Damm, K.L., and M.D. Lilley (2004), Diffuse flow hydrothermal fluids from 9°50'N East Pacific Rise: Origin, evolution and biogeochemical controls, *Geophysical Monograph, 144,* 245−268.

Wankel, S.D., S.B. Joye, V.A. Samarkin, S.R. Shah, G. Friederich, J. Melas-Kyriazi, and P.R. Girguis (2010), New constraints on methane fluxes and rates of anaerobic methane oxidation in a Gulf of Mexico brine pool via in situ mass spectrometry, *Deep Sea Research Part II: Topical Studies in Oceanography, 57*(21-23), 2022−2029.

Wankel, S.D., L.N. Germanovich, D.L. Marvin, G. Genc, C.J. DiPerna, A.S. Bradley, E.J. Olson, and P.R. (2011), Girguis Influence of subsurface biosphere on geochemical fluxes from diffuse hydrothermal fluids, *Nature Geoscience, 4,* 461−468.

Williams, D.L., and R.P. Von Herzen (1974), Heat loss from the earth: new estimate, *Geology, 2*(7), 327−328.

Wolery, T.J., and N.H. Sleep (1976), Hydrothermal circulation and geochemical flux at mid-ocean ridges, *The Journal of Geology, 84,* 249−275.

Zonenshain, L.P., M. Kuzmin, A.P. Lisitsin, Y.A. Bogdanov, and B.V. Baranov (1989), Tectonics of the Mid-Atlantic rift valley between the TAG and MARK areas (26-24°N): evidence for vertical tectonism, *Tectonophysics, 159*(1-2), 1−23.

CHAPTER 2

MEASURING FLUID FLOW IN SEAFLOOR HYDROTHERMAL ENVIRONMENTS

Abstract. We have designed, built, calibrated, and tested new flow meter devices to measure fluid velocity at high-temperature focused and low-temperature diffuse discharge sites at oceanic spreading centers. The devices are designed to perform at ocean floor depths and black smoker temperatures, and can be used to measure fluid velocities between 2 and 317 cm/s. The devices are compact and lightweight enough for deployment from either a manned submersible or a remotely operated vehicle. For the sake of robust and reliable performance in the deep sea environment, the devices do not have sensors to record and store fluid velocity, but rather rotation rates are determined from video recording and converted to velocity using calibration curves. An important feature of these devices is an open bearing design that eliminates clogging by particles or chemical precipitates as the fluid passes by the rotors. The flow rates determined from the devices can be used in conjunction with discharge temperature and area to obtain instantaneous point measurements of heat output from vent chimneys and diffuse flow regions. The fluid flow data can also be used in conjunction with geochemical measurements to determine chemical fluxes. The devices have been tested on 24 *Alvin* dives on the Juan de Fuca Ridge at depths up to 2,400 m and temperatures up to 364^{o} C. We report 63 new measurements that show the capability of the devices. In particular, our devices measured the lowest rate of diffuse flow ever

recorded at the Juan de Fuca Ridge, and the results obtained with our devices represent the first advective heat output measurements at the High Rise vent field and direct fluid flow measurements at Middle Valley.

2.1 Introduction

The discovery of low temperature hydrothermal discharge at the Galapagos Spreading Center in 1977 [*Corliss et al.,* 1979] and high-temperature vents a year later on the East Pacific Rise (EPR) [*Spiess et al.,* 1980], together with their associated biological ecosystems [*Corliss et al.,* 1979] ushered in a new era of marine geophysical exploration at oceanic spreading centers. The mineral-laden, dark-colored, high-temperature fluids vent from discrete chimneys called "black smokers" whereas low to moderate temperature diffuse discharge occurs from nearby patches of seafloor or from sulfide edifices on which the high-temperature vents reside. Diffuse flow discharge that occurs near black smokers and the vents at the Galapagos Spreading Center have chemical signatures indicating that they are mixtures of high-temperature fluid and seawater [e.g., *Edmond et al.,* 1979; *Corliss et al.,* 1979; *Von Damm and Lilley,* 2004]. Since these discoveries, numerous methods have been used to determine heat flow from both high-temperature and low-temperature discharge zones [e.g., *Converse et al.,* 1984; *Baker and Massoth,* 1987; *Thomson et al.,* 1992; *Ginster et al.,* 1994; *Schultz et al.,* 1992].

Flow data from diffuse sites are necessary for understanding the geochemical and nutrient fluxes to seafloor biological communities, which are required for comprehending ecosystem maintenance and evolution [*Butterfield et al.,* 2004; *Von*

Damm and Lilley, 2004; *Wankel et al.,* 2011]. Advective heat transfer data from both diffuse and focused flow sites are critical for understanding the physical and geochemical evolution of seafloor hydrothermal systems [e.g., *Lowell and Germanovich,* 1994, 2004]. These data provide important constraints on mathematical models that relate magmatic and hydrothermal heat fluxes [e.g., *Liu and Lowell,* 2009; *Lowell,* 2010; *Germanovich et al.,* 2011].

Measurements of hydrothermal heat flux can be categorized into two broad classes: direct measurements from discrete vents and integrated water-column measurements that are made on the scale of a vent field. In this paper, we first review previous techniques for measuring advective heat output from seafloor hydrothermal systems. Then, we describe new devices for making point measurements of fluid flow and heat output and discuss results of their testing during 24 dives on submersible *Alvin.*

2.2 Measurements of Advective Heat Output From Seafloor Hydrothermal Systems

2.2.1 Integrated Flux Measurements

Hydrothermal discharge at the seafloor, whether from discrete high-temperature vents or low-temperature diffuse flow sites, tends to form buoyant plumes that transfer mass and energy up to several hundred meters above the seafloor [*Dymond et al.,* 1988; *Speer and Rona,* 1989; *Middleton and Thomson,* 1986]. These plumes provide important sampling sites for studying the chemistry of hydrothermal vents, and geochemical cycling between the lithosphere and ocean [*Elderfield et al.,* 1993; *Kadko,* 1993; *Johnson and Pruis,* 2003; *Wheat et al.,* 2003]. Hydrothermal plumes

are likely to be important mechanisms for biological dispersal [*Metaxas,* 2001; *Van Dover and Lutz,* 2004], and they may also affect deep ocean circulation [*Stommel,* 1982; *Thomson et al.,* 2003, 2005]. As hydrothermal plumes rise in the water column, they entrain denser ambient seawater. When the buoyant plume reaches its level of neutral buoyancy, it spreads laterally [e.g., *Turner,* 1986].

To map the location and dimensions of the plume and hence estimate the total heat output at the *scale of a vent field*, ship-based surveys of the neutrally buoyant plume are conducted by deep conductivity-temperature-depth (CTD) and transmissometer tows or vertical casts and water bottle sampling [*Baker and Massoth,* 1987; *Thomson et al.,* 1992]. Towed sensor packages may be cycled in different patterns (e.g., sawtooth or vertical) and tracked by an acoustical navigation system. Contrasting changes in heat and particle properties of the plume are attributed to hydrothermal venting during the advection of the plume from its source. Therefore, these hydrothermal plumes can be identified and tracked from mapped values of temperature, salinity, conductivity, and light-attenuation anomalies which are related to the concentration of suspended particles in the upper water column [e.g., *Baker and Massoth,* 1987; *Thomson et al.,* 1992; *Baker,* 1994; *Gendron et al.,* 1994; *Baker et al.,* 1998]. Currents are obtained by current meter moorings to define the relationship of the plume to the regional hydrographic setting. The advective transport of heat is then calculated and total mean and instantaneous heat flux is estimated by using the distributions of heat and particle emissions out of the vent field or survey region [*Baker and Massoth,* 1987; *Thomson et al.,* 1992].

Integrated heat flow measurements have been conducted at various locations including Flow and Floc vent areas at the CoAxial segment [*Baker et al.,* 1998], North Cleft [*Baker et al.,* 1993] at Juan de Fuca Ridge (JdF), and Broken Spur [*Murton et al.,* 1999] and TAG [*Rudnicki and Elderfield,* 1992] at the Mid-Atlantic Ridge. Integrated heat output estimates have also been obtained at the Main Endeavour Field using the Autonomous Benthic Explorer (ABE) to estimate the heat output [*Veirs et al.,* 2006]. Measurements of vertical velocity, temperature, and salinity, obtained by the ABE onboard sensor, were used to estimate vertical heat output through the top surface of the control volume. The heat flow through the sides of the control volume was determined by a combination of ABE sensors, CTD surveys, and two current meter moorings.

2.2.2 Vent Scale Measurements

2.2.2.1 Buoyant plume measurements

In buoyant plumes, above discrete vents, a package of instruments is deployed from a submersible to obtain profiles of temperature, velocity, conductivity, and pressure. The package includes a vertical cabled array that contains a chain of sensors such as thermistors, CTD, and transmissometer. Typically, the ambient stratification is monitored by the instrument array during the descent of the submersible through the water column, whereas the turbulent fluctuations are recorded as a function of time once the submersible is stabilized at a vent site. *Little et al.* [1987] and *Bemis et al.* [1993] used such an array to determine heat flow from individual discrete vents by using

either simple linearized plume theory [*Fischer et al.,* 1979; *Tennekes and Lumley,* 1972; *Papanicolaou and List,* 1987; *Turner,* 1973; *Chen and Rodi,* 1980] or nonlinear plume theory [*Morton et al.,* 1956; *Fischer et al.,* 1979]. They then combined measurements from individual vents to obtain total focused high-temperature heat flux from the vent field. For example, *Bemis et al.* [1993] found that the median heat flux per vent was 9 MW and 3 MW, respectively, for the Endeavour (18 vents) and Southern (18 vents) segments, while the total heat flux from high-temperature venting at these JdF segments was estimated as 239 MW and 66 MW, respectively. *Little et al.* [1987] estimated the total heat flow from the EPR $10^{o}56'$N vent site as 3.7 MW. Using simple plume theory, *Stein and Fischer* [2001] measured advective heat flux from 10 individual vents in Middle Valley, JdF (8 at Dead Dog and 2 at Bent Hill active venting areas) to be in the range of 1.4 – 39.6 MW.

Although measurements in plumes are effective ways to quantify heat output from discrete high-temperature vents, their interpretation can benefit from comparison to the results of direct flow measurements [*Di Iorio et al.,* 2011; *Xu,* 2010]. Furthermore, it is difficult to use plume methods to obtain heat output from diffuse flow sites. High-temperature buoyant plumes from individual vents and plumes combined from several nearby vents may rise hundreds of meters above the seafloor [*McDuff,* 1995]. Diffuse discharge, however, because of its lower buoyancy flux, would tend to rise relatively short distances above the seafloor [e.g., *Rona and Trivett*, 1992], where it would contribute to the warming of the local bottom water. Consequently, *Bemis et al.* [1993] and *Little et al.* [1987] concluded that estimation of diffuse discharge by applying plume

methods may be difficult. Therefore, measurements in buoyant plumes need to be complemented by estimates of diffuse flow to provide a better prediction of total heat flux and partitioning of heat flow components at both vent and vent-field scale.

2.2.2.2 Acoustic measurements

Acoustic methods have also been used to image and quantify hydrothermal flow both from diffuse flow sources and discrete vents in the plumes. Such methods varied from the use of backscatter of an acoustic pulse from small suspended particles [*Palmer,* 2005] or turbulent temperature fluctuations [*Ostachev,* 1994; *Ross,* 2003] to the use of a Doppler algorithm to measure flow velocity and mean vertical velocity [*Jackson et al.,* 2003]. An alternative method, the *acoustic scintillation* from forward scattered signals, has been applied in the Main Endeavor Field [*Xu and Diorio,* 2011] to monitor integrated plumes and investigate temporal variability in physical properties such as temperature or flow velocity. This method is based on recovering properties of the medium by measuring fluctuations of the acoustic signal passing through the plume [*Di Iorio et al.,* 2005]. By using this method, [*Xu,* 2010] estimated the heat transport of the plume at 20 m above the orifice from Dante as 62 MW.

2.2.3 Point Measurements

Point measurements of hydrothermal heat output involve obtaining temperature, velocity, and discharge area from individual high-temperature smokers or patches of low-temperature diffuse flow. These methods can be grouped into three main categories, described below.

2.2.3.1 Eddy and particle tracking

MacDonald et al. [1980] and *Rona and Trivett* [1992] evaluated the flow velocity in a black smoker plume at the 21°N site at EPR and at the ASHES (Axial Seamount Hydrothermal Emissions Study) hydrothermal field at JdF, respectively. They recorded the turbulent eddies and entrained particulates ascending in the plume. The flow rate was estimated by tracking an eddy or a particle on the video post-dive. For example, *Rona and Trivett* [1992] tracked the particles with respect to a reference scale on a vertical rod held by the submersible *Alvin*'s robotic arm. The velocity of flow from individual orifices ranged from 20 to 90 cm/s, and the corresponding range of heat fluxes was 0.02 – 1.54 MW. *MacDonald et al*. [1980] estimated that at EPR 21°N, 350° C black smoker vents flowed at rates of 1 to 5 m/s using a similar technique based on careful analysis of tracking particulates in the plume from the film and video tapes.

More recently, *Ramondenc et al.* [2006] measured flow velocity utilizing a horizontal stainless steel plate held directly over the vent flow via *Alvin*'s mechanical arm. A circular hole in the center of the plate sampled a portion of the vent flow. The rise time of particles entrained in the fluid emerging through the hole was determined by using the video record to track the particle displacement against a vertical scale attached to the device. **Figure 2.1** shows a similar device [*Ramondenc,* 2008] we deployed later at EPR 9°50'N and at Main Endeavor at JdF. *Ramondenc et al.* [2006] measured the flow rate from individual high temperature orifices at EPR 9°50'N ranging from 10 to 30 cm/s with the range of 0.5 to 1.5 MW of the corresponding heat output.

Their diffuse flow measurements in this location resulted in 4 cm/s and 40.7 MW, respectively.

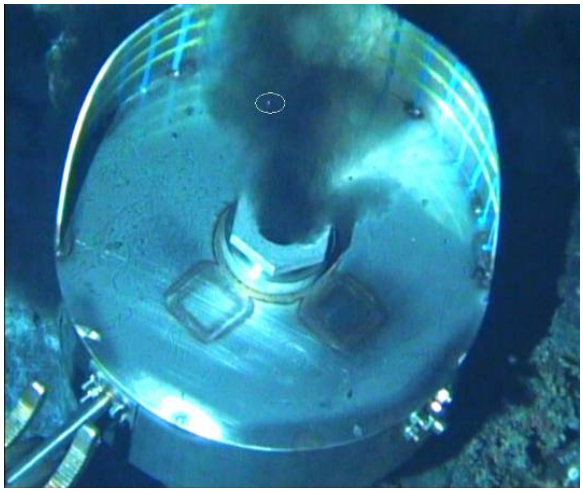

Figure 2.1 Example of flow velocity measurement at a black smoker chimney at Dante vent structure, JdF in September 2007 (cruise AT15-23, *Alvin* dive 4350). A particle is tracked on the frames of the video tape recorded during the dive. Using the known time between the frames, fluid velocity is calculated for the observed particle motion. The distance traveled by the particle is estimated based on the reference grid drawn on the device wall and knowing that the flow direction is sub-vertical and sub-parallel to the grid lines spaced with 2.54 cm interval. Flow rate of the hydrothermal fluid of the 330^{o} C temperature from the orifice of 5 cm was 20 cm/s while the heat output was 0.5 MW. *Ramondenc et al.* [2006] used a similar device with a plate shaped as a square.

Although these devices are relatively simple to use, uncertainties arise because only a limited number of particles can be observed unambiguously, and flow turbulence makes it difficult to accurately determine a particle's rise time. This may have contributed to a large difference in results of different works. For example, *MacDonald et al*. [1980] obtained heat output from an individual orifice at EPR 21^{o}N as high as 250 MW. This exceeds the results of subsequent flow meter measurements of *Converse et al.* [1984] (0.5 – 10 MW at EPR 21°N; see the next section) by one to three orders of

magnitude. Nevertheless, these devices have provided important baseline data for flow velocities at both JdF and EPR hydrothermal sites.

2.2.3.2 Flow meters

Converse et al. [1984] and later *Ginster et al.* [1994] employed a commercial, electro-magnetic turbine flow meter (**Figure 2.2**) to measure fluid flow at black smoker vents at EPR and JdF respectively. The flow meter was deployed from submersible *Alvin* by positioning it with *Alvin*'s mechanical arm at a few centimeters above the high-temperature chimney orifices, along the centerline of hydrothermal plumes. The rotation of the rotor blades created magnetic distortions, as they passed the magnetic sensor, at a frequency rate that was assumed proportional to the volumetric flow rate. In turn, the magnetic distortions created electric pulses, the frequency of which was transmitted to and stored by *Alvin*'s onboard computer. The hydrothermal fluid velocity was then estimated from a calibration curve. As a result, *Converse et al.* [1984] estimated total heat output of 220 MW from three vent structures at the EPR 21^{o}, where heat output from individual vents ranged from 0.5 to 10 MW, The lowest flow rate was estimated to be 70 cm/s. *Ginster et al.* [1994] determined the focused (high-temperature) heat output as 49 MW, 364 MW, and 122 MW, respectively, from Southern Cleft, Main Endeavour, and Tubeworm vent fields at Endeavour, JdF**.** They concluded that focused venting constitutes only 6% of the total heat output in that area.

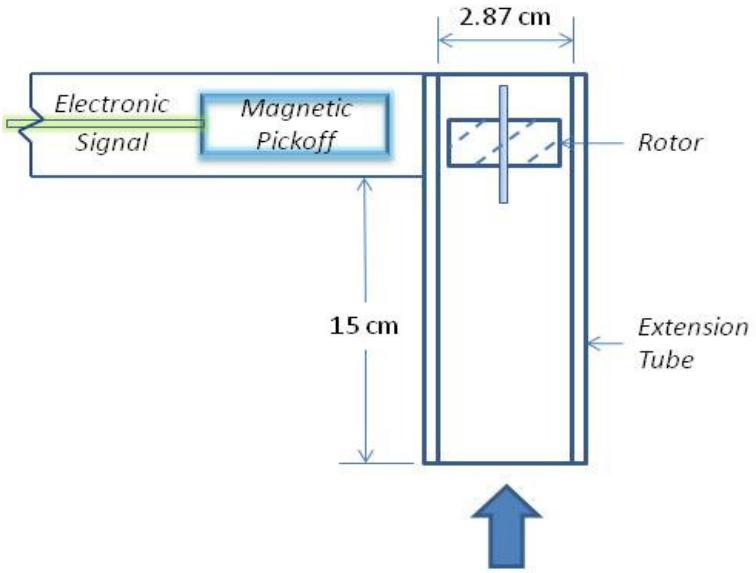

Figure 2.2 Schematics of the commercial turbine flow meter used by *Converse's* [1985] and *Ginster et al.* [1994] at EPR and JdF, respectively. After being deployed from *Alvin* and positioned in the plume a few centimeters above the heat source, the meter starts rotating, creating magnetic distortions that yield electric pulses to be stored by the submarine's computer system. Hydrothermal fluid flow rate is then determined from calibration curves.

Sarrazin et al. [2009] used a dual sensor system that combines two methods to estimate diffuse flow rates. A "flow visualizer" consisting of a transparent graduated pipe was placed atop a cylindrical chamber containing a constant voltage anemometer [*King*, 1914]. Observations of vertical particle ascent in the pipe were obtained through video imagery. The calibrated anemometer was used simultaneously with the flow visualizer. This dual sensor device was used to measure diffuse flow velocity of 4.2 to 18.4 cm/s at the Lucky Strike vent field on the Mid-Atlantic Ridge [*Sarrazin et al.,* 2009].

Schultz et al. [1992] developed an electromagnetic flow meter for measuring diffuse effluent velocities and temperatures by using electromagnetic induction. Hydrothermal flow was channeled into the flow chamber through the flux concentrator cone. The voltage difference between two electrodes was recorded and used to

measure the electro-motive force, which is proportional to the product of magnitudes of the magnetic field and velocity. The flow meter of *Schultz et al.* [1992] was deployed at the Peanut hydrothermal structure, Main Endeavor Filed, JdF and measured diffuse flow rates from 7 to 15 cm/s.

Schultz et al. [1996] describe *Medusa*, a diffuse flow monitoring system composed of a spinning rotor with an optical velocity sensor, two thermocouples, a gasket to keep the device away from the contact with the impurities along the seafloor, and electronics housed in a pressure case. The *Schultz et al.* [1992, 1996] devices could be left in place for days in order to obtain time series of hydrothermal flow velocity and temperature. Because of *Medusa*'s rapid sampling rate, it could monitor short-time variations in effluent temperature and their temporal correlation to discharge rate. Although this device is rather complex, it was able to determine the lowest currently measured diffuse flow of ≈5 mm/s (at the TAG hydrothermal mound, Mid-Atlantic Ridge).

The major issues associated with heat flow measurements by using turbine flow meters have been problems with particle precipitation in high-temperature (focused) venting [*Butterfield et al*., 1994, 1998], which typically coats the turbine blades and jams the bearings [e.g., *Converse et al.,* 1984; *Converse,* 1985; *Ginster et al.,* 1994].

2.2.3.3 Rationale for new point measurement devices

While integrated water column measurements provide a useful estimate of the total heat flux from a hydrothermal vent field, they do not provide insight into the partitioning between focused and diffuse flow components. Direct fluid flow

measurements, when linked with geochemical data, also provide estimates of geochemical fluxes [*Wankel et al.,* 2011]. These fluxes are important for understanding interactions between the hydrothermal processes in oceanic crust and ocean chemistry. Moreover, since many of the chemical constituents in hydrothermal fluids are used by microbial and macrofaunal communities, flux data may provide new understanding of the spatial and temporal characteristics of biological processes at oceanic spreading centers [*Wankel et al.,* 2011]. Finally, integrated water column measurements require a large-scale effort and time to complete, whereas instantaneous point measurements, which may not be entirely representative of the average flow, can be obtained rather easily.

One goal for developing relatively simple devices for point measurements would be for these devices to be part of the standard "tool box" on manned submersibles such as *Alvin* and remotely operated vehicles (ROVs) such as Jason [e.g., *Yoerger et al.,* 1986]. These devices would be relatively compact and lightweight, and sufficiently robust for deployment on any cruise exploring hydrothermal flows at oceanic spreading centers or flows of different nature such as petroleum leaks [e.g., *Crone and Tolstoy,* 2010; *Camilli et al.*, 2011]. As such devices become more widely used, the database for heat and biogeochemical fluxes would grow with time.

Most of the methods for instantaneous point heat flow measurements described in the previous sections were either highly sophisticated [e.g., *Schultz et al.,* 1992; *Schultz et al.,* 1996; *Sarrazin et al.,* 2009] or highly simplified [e.g., *Macdonald et al.,* 1980; *Rona and Trivett,* 1992; *Ramondenc et al.,* 2006]. The sophisticated instruments

are expensive and require high levels of control and maintenance, and hence are not used on a routine basis. A few of them may have adaptation issues with measuring fluid flow velocity in some hydrothermal biological communities such as long tube worms [e.g., *Sarrazin et al.,* 2009]. Methods such as particle tracking have considerable uncertainties because particles entrained in turbulent eddies may not have straight paths. In addition to this, there may not be enough particles to visualize. The earlier turbine flow device [*Converse et al.,* 1984; *Ginster et al.,* 1994] encountered maintenance problems mostly related to the failure of the electronic components and/or coating of bearings exposed to incoming flow by accumulated vent or sediment particles. In this device, bearings were enclosed in the structure, which allowed small particles precipitate from smokers to clog the bearings and alter the measured flow rate over time.

In this work, we have developed three new instruments for making point measurements of fluid flow in seafloor hydrothermal systems. One is based on a cup anemometer design used in hydrological flow measurements [e.g., *Futrell,* 1989; *Vaughn et al.,* 2006] and the other two are turbine flow meters, similar to those employed for flow measurements in pipes [e.g., *Munson et al.,* 2005]. While designing these instruments, our main objective was to develop a robust, lightweight device, which could operate at high-pressure and high-temperature subsea conditions, which would be easy to maintain on shipboard, and would allow reliable flow visualization in both focused high-temperature and diffuse low-temperature environments. Below we

describe these instruments and report some measurement results that show their capabilities.

2.3 Fluid Flow Instruments and Methods

2.3.1 Cup Anemometer

The cup anemometer device consists of a frame and a paddle wheel assembly with a number of attached conical cups. The paddle wheel assembly is mounted on a shaft and rotates freely (**Figure 2.3**). The support frame is assembled to the metal shield by two support rods. The device is shown in **Figure 2.3**, and the details of the design are given in **Appendix 2A**.

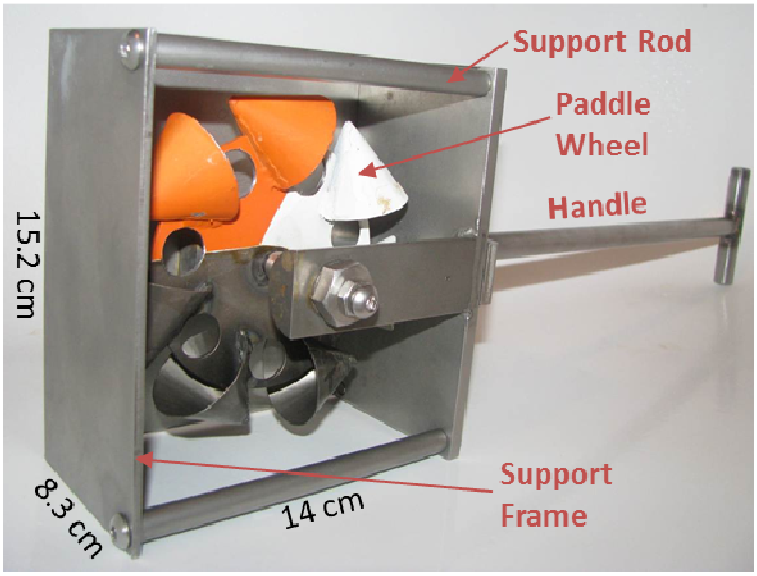

Figure 2.3 Cup anemometer device. The device size is 14.7 × 14.2 × 7.8 cm. A handle is attached to the main frame for ease of deployment from a manned submersible or ROV.

The paddle wheel assembly was fabricated in stainless steel in order to withstand the high pressure and temperature conditions on the seafloor, in both diffuse and focused flow settings. The rotating wheel has an external diameter of 9.4 cm and has seven cups on its body. Occasionally, a conical flux concentrator (**Figure 2.4a**) was attached to the base in order to focus the flow to the anemometer. On two cruises to JdF in July and August 2008, 39 flow measurements were obtained using this instrument (Section 2.5). The device has dimensions of 14.7 × 14.2 × 7.8 cm, and it weighs 1.9 and 2.1 kg in the room temperature water and air, respectively. We also constructed another version of this device, with the paddle wheel and anemometer cups fabricated in a titanium alloy to reduce weight and decrease the potential of corrosion.

The main difference between our device and those used in hydrological flow measurements [e.g., *Futrell,* 1989; *Vaughn et al.,* 2006] is that we implemented an *open* bearing support. That is, the axis of rotation is supported by sapphire jewel bearings that are open to the flow. These bearings are similar to those used in the turbine flow meter and are described, in more detail, in the next section.

To enhance the visualization process, cups of the paddle wheel were painted different colors and often marked with numbers before the deployment. After assembly, the device is deployed over the fluid discharge (**Figure 2.4**) from either a manned submersible or ROV. The flow into the anemometer is recorded by the submarine's video cameras. The device is typically held at a given site for a few minutes to insure that a sufficient number of revolutions are recorded. The rotation rate is estimated post dive from video records by counting the paddle wheel rotations within a

certain amount of time. Linear flow velocity is obtained from the calibration curve constructed from lab test results (Section 2.4).

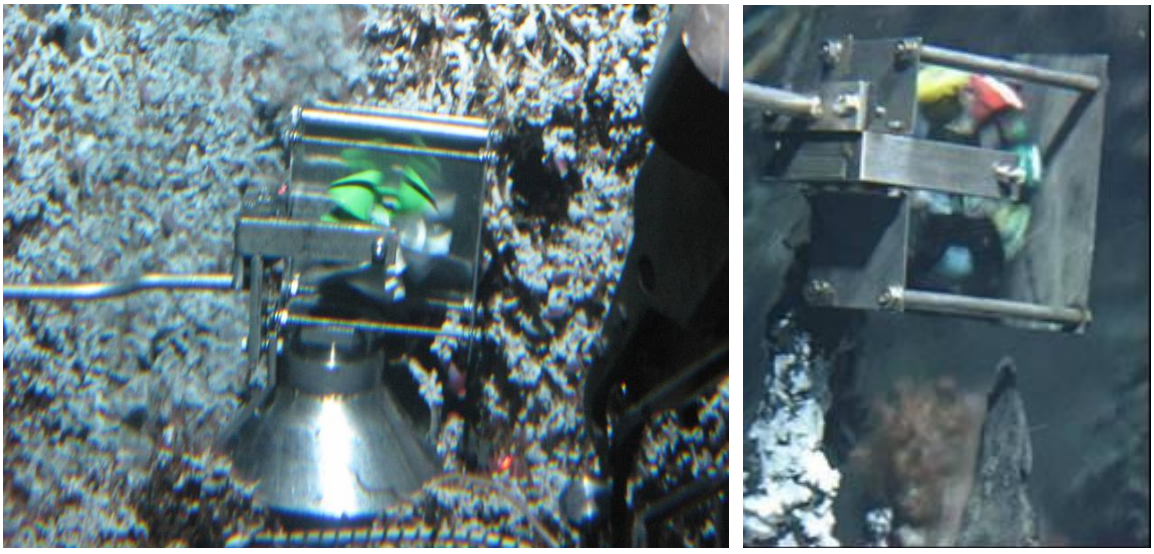

(a) **(b)**

Figure 2.4 Deployment of the cup anemometers **(a)** over low-temperature diffuse flow site (covered with tubeworms) on *Alvin* dive 4412 at the low-temperature the Clam Bed vent field [e.g., *Robigou et al.,* 1993] and **(b)** over a high-temperature gray smoker orifice on *Alvin* dive 4418 to the Mothra Hydrothermal vent field [e.g., *Glickson et al.,* 2007] (both during AT15-34 in July 2008).

The hydrothermal heat output is calculated over the area of an individual chimney orifice or diffuse flow site from

$$H = C_f v (T_f - T_0) A \tag{2.1}$$

where $C_f \approx 4\times10^6$ J/(m^3×°C) is the volumetric heat capacity of the fluid ($C_f = C_p \rho_f$) [e.g., *Riley et al.*, 1975], v is the fluid velocity, $T_f - T_0$ is the difference in temperature between that of hydrothermal vent fluid, T_f, and ambient water, T_0, and A is the area of the discharge site. Temperatures T_f and T_0 are directly measured by the submarine's

temperature sensors. The orifice sizes are estimated from video footage, although they can also be measured during the dive.

2.3.2 Turbine Flow Meter

The turbine flow meter (TFM) design is similar to that of flow meters used in pipe systems [e.g., *Munson et al.,* 2005]. The TFM principal components include: (1) main body (flow tube), (2) turbine rotor assembly, and (3) upper and lower bearing supports (**Figure 2.5**). It also incorporates a handle and a pipe adapter (**Figure 2.6**). We developed two versions of the turbine flow meter, TFM1 and TFM2, which differ by their rotor assemblies. Otherwise their designs are similar. We first describe TFM1 and then indicate how TFM2 differs from TFM1.

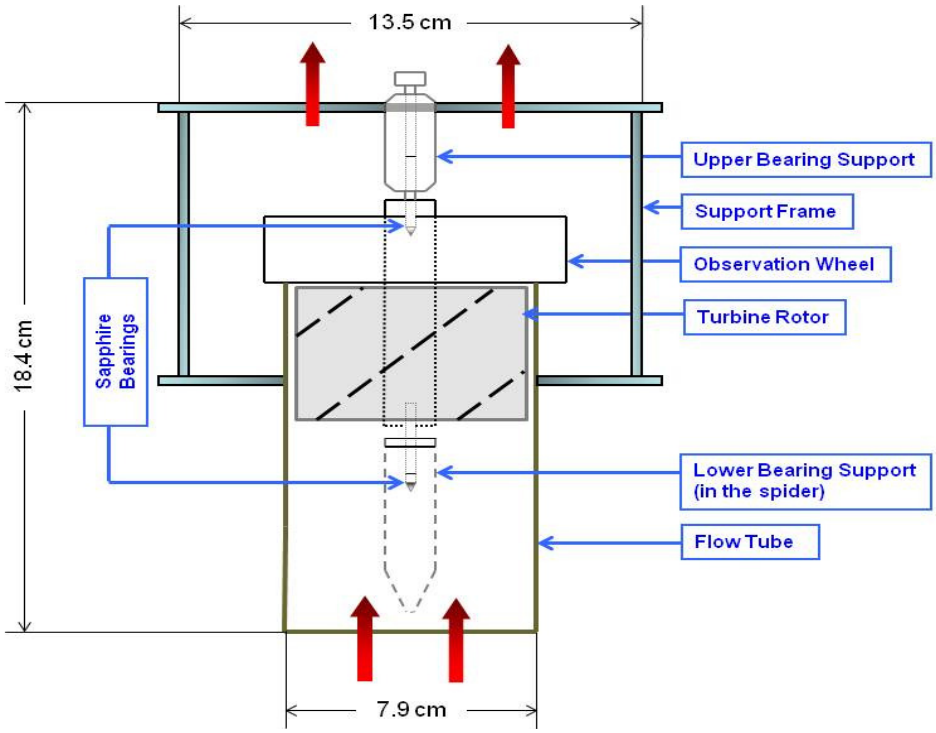

Figure 2.5 Schematic drawing (not to scale) of the turbine flow meter showing the major components.

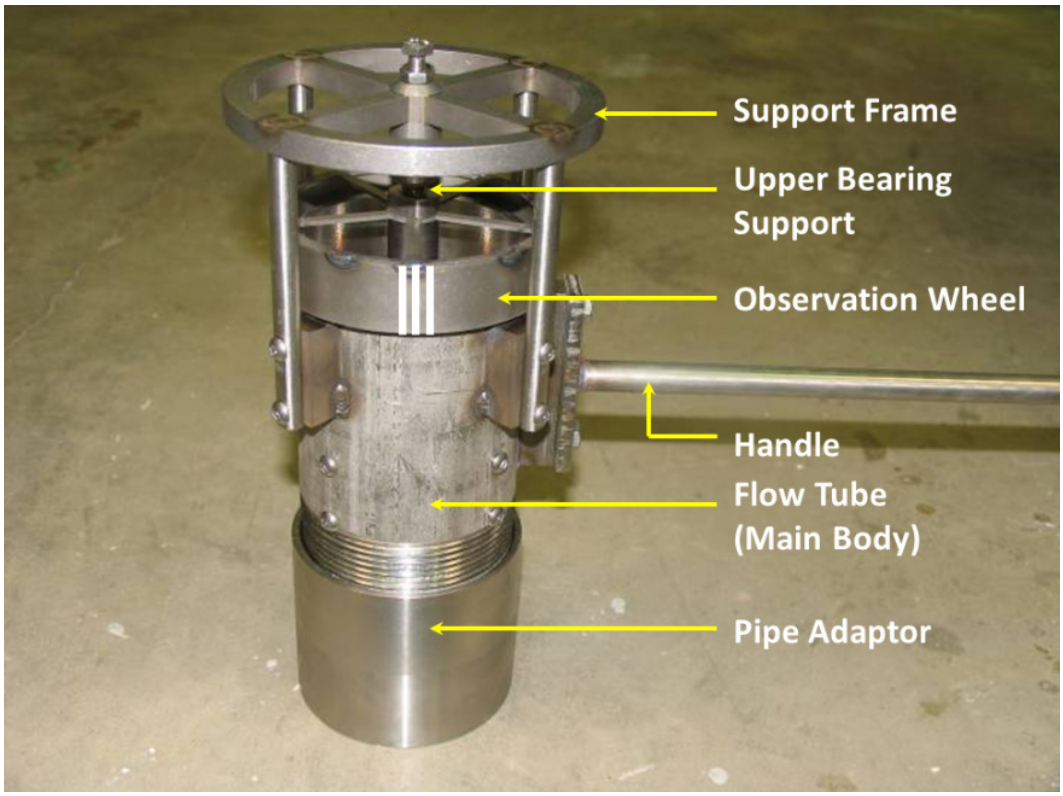

Figure 2.6 Turbine flow meter TFM1.

Most of the TFM1 components are made from the molybdenum-alloyed austenitic stainless steel grade 316 [e.g., ASTM A313], which is the preferred grade of stainless steel for salty water exposure [ASM 2005]. The main body (flow tube) has an internal diameter of 7.9 cm and houses the turbine rotor assembly, which consists of the turbine and an observation wheel (**Figure 2.6**). Since the rotor is covered and cannot be directly observed, the wheel protrudes outside the flow tube. This allows for visualizing the rotations from the submersible. The rotor assembly is concentrically mounted on the lower and upper bearings and is supported on both ends by sapphire jewels (**Figure 2.7**). The lower bearing is supported by spring pressure. The spring pressure is adjustable and allows for optimal bearing pre-load, which enables smooth and consistent operation. For the sake of robust and reliable performance in the deep-

sea environment, the instrument configuration does not include electronic sensors to collect and record the rotation rate. Instead, the rotation is determined from video imagery recorded by using standard *Alvin* or ROV video equipment. A white mark is painted on the observation wheel of the rotor assembly as a reference (**Figure 2.6**), so that rotations of the turbine rotor can be tracked by video recorder. The design of the flow meter does allow for efficient adaptation of electronic sensors, however.

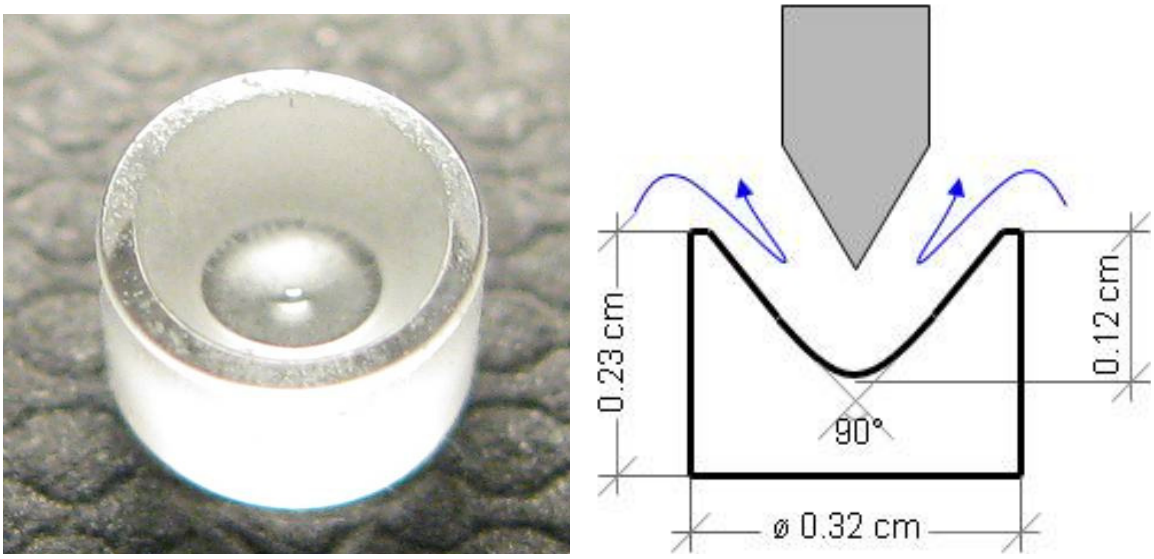

(a) **(b)**

Figure 2.7 (a) Sapphire vee jewel and **(b**) schematics of sapphire jewel bearing support.

When the instrument is placed over a vent orifice or diffuse flow site, the hydrothermal fluid flows through the rotor assembly (**Figure 2.8**). As a result of the angle between the turbine blades and the flow direction, the flow exerts a torque that initiates the rotation. The device is held in place by a manipulator arm of the submersible, and the cameras on the submersible record the rotations. As with the anemometer device, rotation rate is determined by analyzing recorded video imagery.

We determine the number of rotations per unit time and convert to linear velocity using the calibration curves (Section 2.4). Heat flux is then determined from equation (2.1).

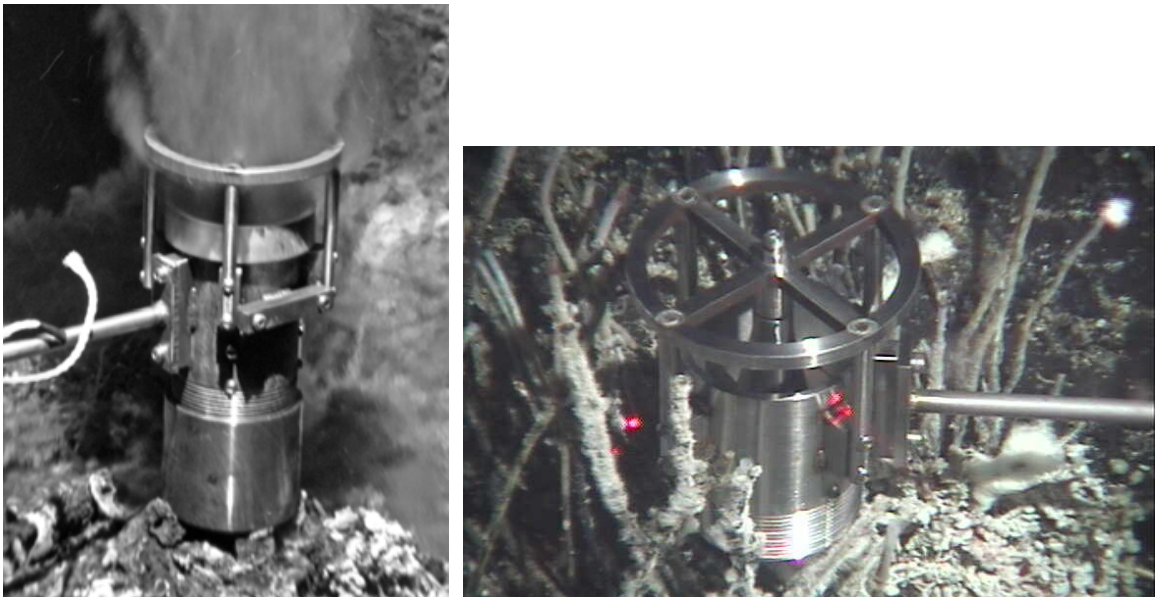

(a) **(b)**

Figure 2.8 (a) Deployment of TFM1 at a black smoker at Fairy Castle vent structure at the High Rise vent field (cruise AT15-47, *Alvin* dive 4526, June 2009). The fluid flow rate was estimated to be 80 cm/s. **(b)** TFM2 deployed at a diffuse flow site at the Hulk vent structure in the Main Endeavour vent field (*Alvin* dive 4627 during cruise AT15-67 in July 2010). Distance between two red laser dots is 10 cm. The velocity of diffuse fluid was 3.3 cm/s.

Although we obtained a significant number of reliable measurements with TFM1 at flow velocities greater than 7.7 cm/s (Section 2.5), we designed another turbine flow meter device, TFM2, to determine lower flow velocities. Support frames and flow pipes of TFM1 and TFM2 are identical, but we modified the configuration of the turbine rotor assembly, the details of which are shown in **Figure 2.A4** (**Appendix 2A**). Because low flow velocities are more characteristic for diffuse flow, which is transparent or semi-transparent, we removed the observation wheel to reduce the turbine weight and fluid

drag forces. To further reduce its weight and to increase sensitivity, we used grade 2 titanium [ASTM B265-11] to manufacture the turbine rotor. We also changed the pitch angle (i.e., the angle of the blade inclination with respect to the rotor axis) from 45^{o} to 65^{o}. Deployed TFM2 is shown in **Figure 2.8b**. Note that in most cases we did not use the pipe adapter with TFM2, which reduced the distance between the diffuse flow source and the rotor assembly.

2.3.3 Comparison between the Anemometer and Turbine Flow Meter

The cup anemometer was deployed on 12 separate *Alvin* dives on cruises AT15-34 and AT15-36 to the Endeavour segment of JdF in July and August 2008, respectively. We obtained a total of 39 measurements of fluid flow. TFM1 was completed prior to the June 2009 cruise AT15-47 to JdF and field-tested on 5 *Alvin* dives during that cruise. It was also deployed on one *Alvin* dive on cruise AT15-67 to JdF in July 2010. TFM2 was tested on 6 *Alvin* dives during this cruise. Details of these deployments are given in Section 2.5.

Both the anemometer and turbine flow meters incorporate an open sapphire jewel bearing system that distinguishes these flow meters from previously designed instruments [e.g., *Converse et al.*, 1984; *Ginster et al.*, 1994]. This key component in the design of the devices allowed hydrothermal fluid to simply flow pass the bearings (**Figure 2.7b**). As a result, particle precipitation and clogging on the critical parts of the device (i.e., sapphire bearings) were eliminated.

Due to the difference in axis orientation, the rotation of a TFM axis is much smoother and more consistent than for a cup anemometer. This difference is important

for long-term deployment. The TFM has an axis orientation that is parallel to the flow direction. Therefore, the primary load on the bearings results from the axial (thrust) force component. The bearing pre-load is only required to maintain the axial alignment, as radial loads are minimal. Conversely, the anemometer axis is perpendicular to the fluid flow. This exerts a significant radial load on the sapphire jewels and rotating shaft. The ability to carry the radial load is dependent on the bearing preload. Consequently, the anemometer required much higher pre-loads that contributed to larger amounts of wear and durability issues.

Occasionally, we replaced the sapphire jewels in the cup anemometer when they started showing signs of wear or damage. Design of bearing supports allows their easy replacement. The TFM devices did not require bearing replacement, however. Another advantage of the TFM devices is that the rotor assembly is contained inside the flow pipe. This is a common configuration for flow meters in conventional pipe systems [e.g., *Webster,* 1999]. Therefore, standard design approaches [*Baker*, 2000] for blade geometry and pitch angle can be used for the configurations of TFM devices. Likewise, standard methods [e.g., *Baker*, 2000] can be employed for their calibration (Section 2.4).

TFM is a more robust instrument than the cup anemometer and is less likely to be damaged during transport or deployment by the submarine. Additionally, the closed-structure frame enables TFM devices to completely sample the fluid jet by enclosing the entire flow (e.g., **Figure 2.8a**). In contrast, the open-structure frame of the cup anemometer may result in underestimating the flow rate by partial sampling of the jet. Also, due to the containment of the fluid within the TFM device, electric sensors could

monitor rotations without direct exposure to the fluid flow, while maintaining the video analysis as backup.

On the other hand, enclosing the black smoker flow in the flow pipe results in more aggressive particle precipitation on the hot, stationary components made of stainless steel. For example, due to the precision spacing between the internal surface of the flow pipe and rotating titanium blades of the turbine, this surface needs to be cleaned, typically once or twice per cruise. This effect can be mitigated, however, by replacing the steel flow pipe by the titanium one. This would be an effective solution for a long term deployment of TFM devices. Sea trials (Section 2.5) showed that both devices performed successfully and required little (if any) post-dive shipboard maintenance such as cleaning the components, repainting the observation mark if needed, or adjusting spring tension.

2.4 Calibration

2.4.1 Method

The cup anemometer and TFM1 were calibrated in the hydraulics lab of Georgia Tech before and after deployment. The calibration procedure consisted of a transparent flume and an injection pipe with a water source capable of constant and adjustable flow rates. The inner pipe diameter was 5 cm, which is characteristic for black smoker orifices. Calibrations were performed with a pipe located inside the flume to mimic the orifice of a vent chimney, and the devices were held over the opening of the pipe. An example is shown in **Figure 2.9a**. To evaluate the performance of both devices at flow

velocities characteristic of focused hydrothermal venting [e.g., *Ramondenc et al.,* 2006], we calibrated TFM1 and the cup anemometer at flow rates of 115 to 4304 cm^3/s and 283 to 8495 cm^3/s, respectively, which corresponded to flow velocities of 7 to 170 cm/s and 11 to 317 cm/s. Rotation rates were determined both during the test by using a stroboscope (i.e., precision frequency adjustable strobe light) and afterward by examining the recorded video.

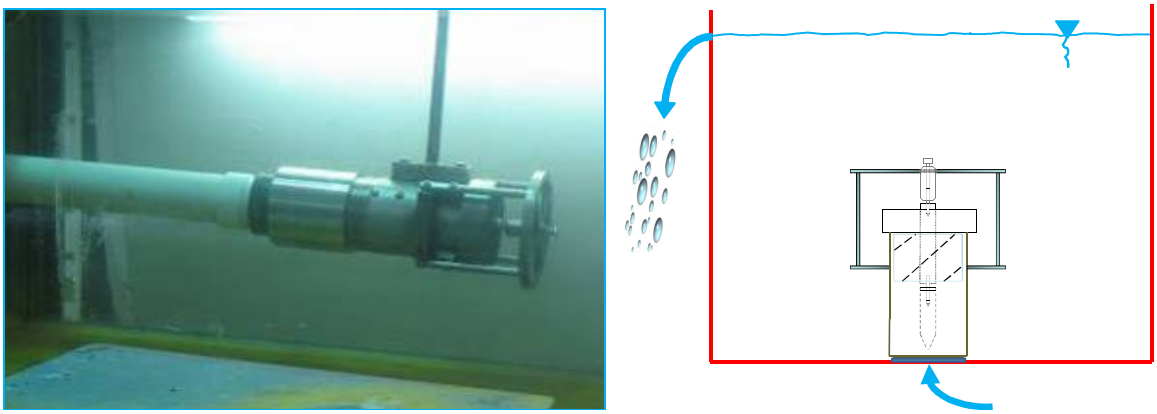

(a) **(b)**

Figure 2.9 (a) TFM1 calibration set-up in the hydraulic flume. Calibrations were performed between 115 and 4304 cm^3/s of volumetric flow rates, which translated to flow velocities between 7 and 170 cm/s. The rotations were simultaneously monitored by a stroboscope and a video camera. The number of revolutions corresponding to a certain flow rate was then determined post-experiment by using the recorded video imagery. The calibration curve shown in **Figure 2.10** was constructed based on these measurements. **(b)** Laboratory set-up for calibrating TFM2 at low flow rates. Calibrations were performed in a plastic container by changing the flow rates manually from the water faucet. The relatively slow rotations were videotaped, visually counted, and plotted on the calibration curve (**Figure 2.10**) for flow rates ranging from 44 to 200 cm^3/s, which translated to flow velocities between 2 and 10 cm/s.

To obtain a calibration curve for speeds less than 10 cm/s we used the experimental set-up shown in **Figure 2.9b** to calibrate TFM2. This set-up included a plastic container used as a water reservoir. TFM2 was placed in the container, by tightly fitting its main body to the 5.1 cm hole drilled at the bottom of the container. Water, at

a constant rate, fed directly into the turbine and filled the container. Once the container was filled, the water level was kept constant by allowing water to flow out freely through a hole drilled on the upper wall of the container (**Figure 2.9b**). The number of full rotations completed by the rotor per unit time was counted visually and recorded. This process was repeated for volumetric flow rates between 44 and 200 cm^3/s, which translated to flow velocities between 2 and 10 cm/s. Such velocities are characteristic for diffuse hydrothermal flow [*Ramondenc et al*., 2006; *Sarrazin et al.,* 2009]. Currently, 2 cm/s is the lower limit of velocity that can be measured with TFM2. The measurable flow velocity, however, can be reduced further by using materials with lower friction on contacts, such as coated titanium vs. synthetic sapphire, or employing more sophisticated blade geometry (e.g., helically twisted that generates larger rotating moments (e.g., appropriately curved blades [*Baker,* 1993; *Merzkirch*, 2005]).

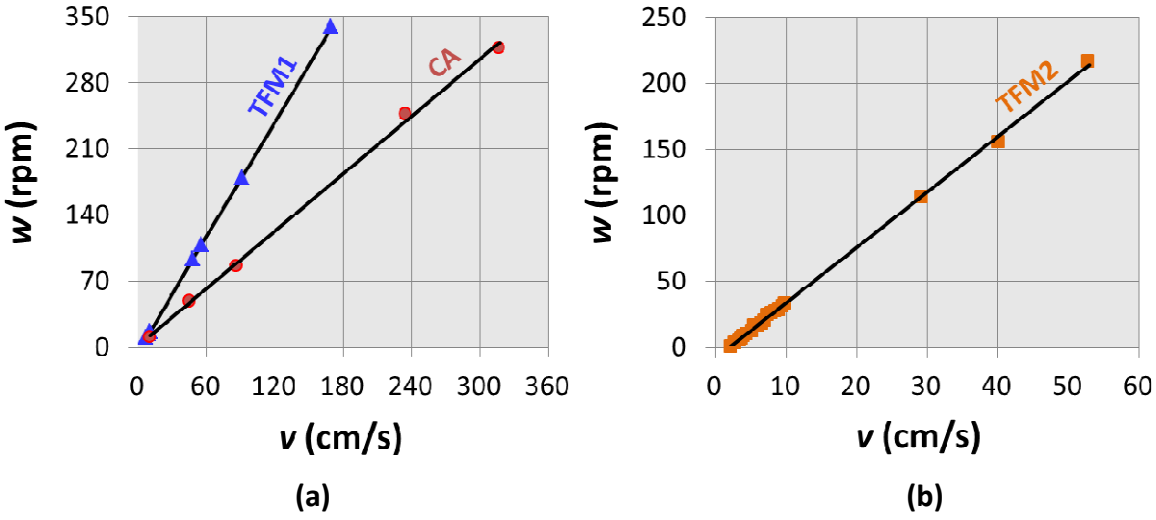

Figure 2.10 (a) Calibration results for the cup anemometer (circles) and TFM1 device (triangles). **(b)** Calibration results (squares) for TFM2 device. Data for $v \leq 10$ cm/s was obtained in the laboratory set-up shown in **Figure 2.9b**. At faster rates of $v > 10$ cm/s, TFM2 was calibrated similarly to TFM1 (**Figure 2.9a**).

Although TFM2 was designed to be used primarily at diffuse flow sites, we also calibrated it at higher velocities (**Figure 2.10b**) for use in focused transparent and semi-transparent flows, such as white and gray smokers. This calibration was done in the same flume as that for TFM1 and cup anemometer. Different calibration methods, however, resulted in the same calibration line (**Figure 2.10b**).

2.4.2 Calibration Results

During the calibration of the cup anemometer, rates of rotation ranged between 11 and 318 rpm. The corresponding flow velocities ranged between 11 and 317 cm/s. Similarly, we calibrated the TFM1 over an interval of flow velocities between 7 and 170 cm/s. To calibrate TFM2, we monitored its performance at rotation rates of 1 to 34 rpm, yielding a range of flow velocity from 2 to 10 cm/s.

The results of the calibration tests are plotted in **Figure 2.10** and are fit with linear dependence

$$w = w_0\left(\frac{v}{v_0} - 1\right) \tag{2.2}$$

where w is the number of rotations per unit time, and v is the linear flow velocity. The fitting parameters, w_0 and v_0 for each device are given in **Table 2.1**. The values of the coefficient of correlation, r^2, are all greater than 0.98. For TFM1 and TFM2, v_0 has a meaning of minimum velocity required to overcome and initiate turbine rotations. Value v_0 = 1.95 cm/s is nearly identical to 2 cm/s we observed during the TFM2 calibrations (**Figures 2.9b and 2.10b**). The value of v_0 for the cup anemometer is negative, however, which means a non-linear dependence $w(v)$ at small flow rates. Hence, extrapolation of

the results determined with the cup anemometer to the region of $v < 10$ cm/s should be done with care. Since $v_0 > 0$ for TFM1 and, in fact, is relatively close to that of TFM2, extrapolating the TFM1-calibration to $v < 7$ cm/s is probably more reliable. In the next section, reporting the field tests of our devices, we explicitly indicate when, on a few occasions, we extrapolate the measurement results beyond the calibrated range (**Table 2.1**).

Table 2.1 Fitting parameters in equation (2.2) for calibration curves shown in **Figure 2.10**.

Device	v_o (cm/s)	w_o (rpm)	**Calibration Range**	
			v (cm/s)	w (rpm)
Cup anemometer	-1.975	-2.002	11 – 317	11 – 318
TFM1	2.670	5.426	7 – 170	10 – 340
TFM2	1.954	8.197	2 – 55	1 – 34

2.5 Field Tests

The cup anemometer was deployed on 6 separate *Alvin* dives on cruise AT15-34 to the Endeavour segment of JdF in July 2008. We obtained a total of 24 measurements of fluid flow at Hulk and Dante structures in the MEF and at the Faulty Towers structure of the Mothra field (**Figure 2.11**). In August 2008, we obtained 15 additional flow rate measurements at Dante, Hulk, Crypto, Grotto, and S&M vent structures (**Figure 2.11**) conducted on 6 *Alvin* dives during cruise AT15-36. Flow rates ranged between 5.1 and 76.5 cm/s whereas temperatures ranged between 49^{o} C and 337^{o} C. Individual heat

output values ranged from 7 kW for a focused high-temperature vent on Dante in MEF to nearly 12 MW at a black smoker orifice on Main Tower of Mothra.

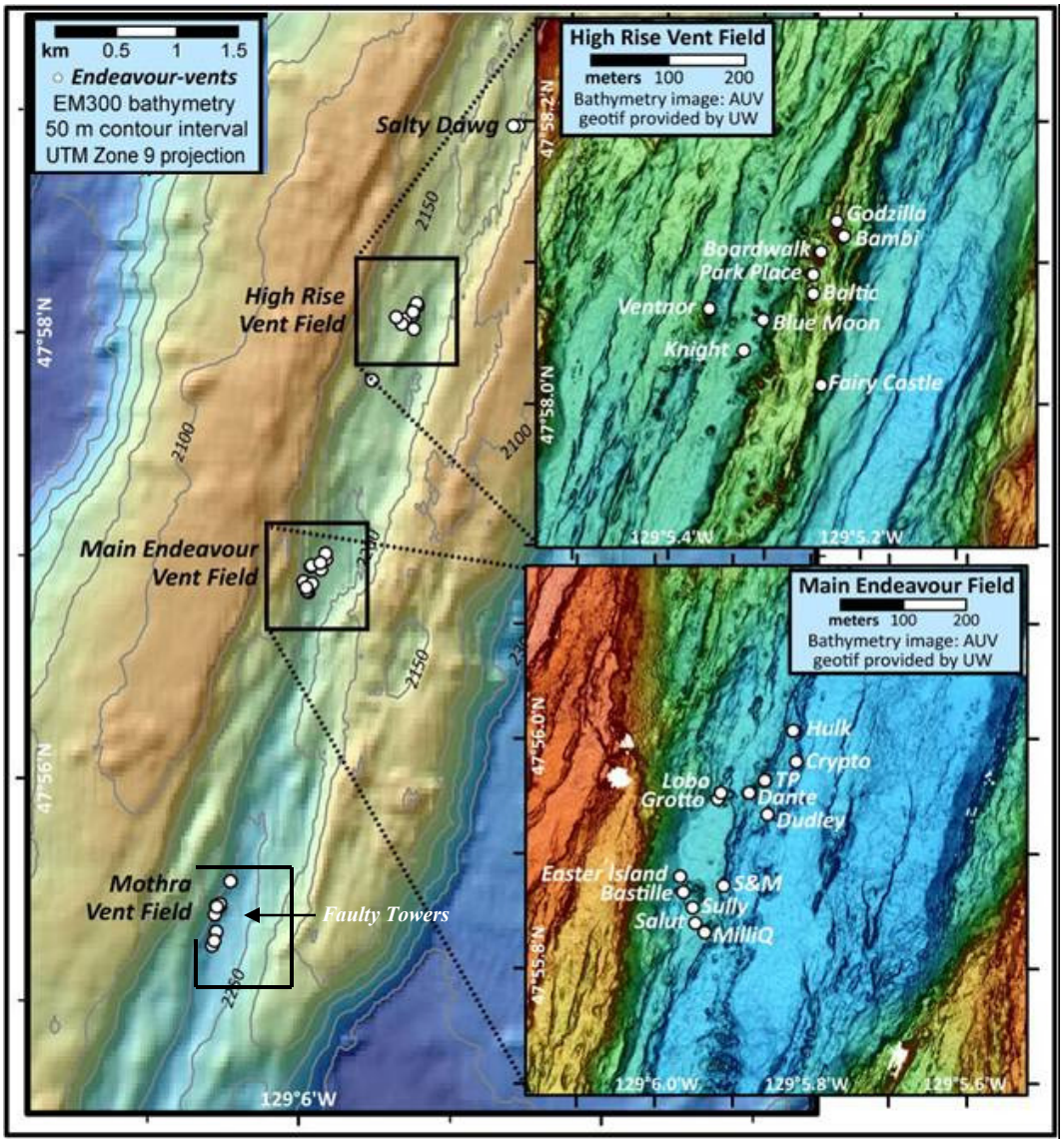

Figure 2.11 Map of the Endeavour segment, JdF showing hydrothermal vent fields [modified after *Merle, 2011*].

Results of measurements with the cup anemometer device are given in **Table 2.2**. Most of the measurements were made at high-temperature vent sites, as this device is more suitable for relatively high flow rates (**Table 2.1**).

Table 2.2 Results of heat flow measurements performed by the cup anemometer device along the Endeavour segment, JdF on the July (AT15-34) and August (AT15-36) 2008 *Alvin* cruises. Values in bold represent data from diffuse flow sources. Red font denotes results obtained based on equation (2.2), but extrapolating beyond the range of device calibration (**Table 2.1**).

Structure **Cruise / Dive**	***Alvin*** **coordinates X, Y, Z (m)**	**Mean velocity (cm/s)**	**T (°C)**	**Flow area (cm^2)**	**Flow rate (cm^3/s)**	**Heat output (MW)**
Main Endeavour vent field						
Hulk						
AT15-34 / 4414	5045, 6254, 2186	54.6	322	12.6	686.0	0.88
	5041, 6230, 2187	76.5	313	29.8	2278.8	2.85
	5035, 6236, 2186	25.9	312	8.9	229.9	0.29
AT15-34 / 4416	5034, 6251, 2190	11.8	304	5.0	58.7	0.071
	5034, 6253, 2193	21.8	136	169.5	3688.1	2.01
	5036, 6256, 2192	10.7	256	14.3	152.7	0.16
	5040, 6245, 2188	15.3	272	67.4	1028.4	1.12
	5040, 6245, 2188	22.5	279	120.2	2698.0	3.01
	5045, 6253, 2184	16.6	260	127.9	2122.8	2.21
AT15-34 / 4420	5041, 6260, 2186	8.2	213	3.3	26.8	0.023
AT15-36 / 4447	5047, 6246, 2188	14.5	308	12.6	182.3	0.22
AT15-36 / 4449	5043, 6243, 2197	13.0	324	50.3	652.0	0.84
AT15-36 / 4452	5047, 6262, 2191	27.0	320	19.6	529.7	0.68
	5068, 6262, 2191	62.3	328	28.3	1760.9	2.31
	5068, 6262, 2191	14.1	85	50.3	710.3	0.24
Dante						
AT15-34 / 4415	4976, 6144, 2191	73.1	319	21.8	1593.2	2.03
AT15-34 / 4422	4968, 6146, 2185	6.5	250	1.1	6.8	0.0068
	4969, 6160, 2185	24.1	328	25.1	604.2	0.79
	4972, 6163, 2182	66.8	333	48.0	3206.0	4.27
	4977, 6154, 2180	22.1	210	20.8	458.4	0.39
	4965, 6135, 2185	21.2	300	4.2	89.8	0.11
	4987, 6172, 2175	6.7	333	57.8	385.7	0.51
	4987, 6172, 2175	9.2	333	29.8	274.5	0.37
	4987, 6172, 2175	7.9	142	94.2	743.0	0.42
	4988, 6170, 2175	9.5	312	27.4	259.5	0.32
	4984, 6175, 2174	22.4	236	253.9	5684.8	5.38
AT15-36 / 4439	4973, 6162, 2176	49.9	328	12.6	627.5	0.82
AT15-36 / 4441	4954, 6165, 2185	51.8	328	28.3	1463.0	1.92
AT15-36 / 4447	4977, 6157, 2175	73.0	325	38.5	2809.8	3.65
	5096, 6054, 2173	61.8	337	44.2	2729.9	3.68
	4980, 6163, 2179	28.9	337	41.9	1209.5	1.63
AT15-36 / 4452	4974, 6153, 2175	5.9	163	12.6	73.8	0.048
AT15-34 / 4420	**4997, 6182, 2194**	**7.3**	**52**	**7.3**	**53.4**	**0.011**
Grotto						
AT15-36 / 4439	4923, 6145, 2185	54.0	324	3.1	169.7	0.22
	4935, 6146, 2189	53.2	330	132.7	7058.6	9.32
S&M						
AT15-36 / 4446	**4938, 6013, 2189**	**5.1**	**49**	**112.0**	**565.6**	**0.11**
Crypto						
AT15-36 / 4452	5051, 6219, 2201	65.9	328	12.6	827.7	1.09
Mothra vent field						
Faulty Towers						
AT15-34 / 4418	4152, 3319, 2277	36.0	322	132.7	4778.3	6.15
	4152, 3319, 2277	36.0	322	254.5	9160.9	11.80

Each time the cup anemometer device returned to the ship, its components were carefully examined to insure that the integrity of the device was maintained and the device was cleaned prior to each dive, particularly, when recovered from black smoker areas. In a few of these cases, the surfaces of cups were darkened by smoke accumulation and, therefore, repainted with distinct colors or numbered for monitoring and data analysis purposes.

Results obtained with TFM1 and TFM2 are given in **Table 2.3**. TFM1 was initially tested on cruise AT15-47 to JdF in June 2009. Fluid flow measurements were obtained on 5 dives during this cruise at several diffuse and focused heat sources at Dante in MEF, at Godzilla, Park Place, Fairy Castle and Ventnor vent structures in High Rise field, Endeavour segment, and at the Marker 55 structure (45^{o}55.9920'N, 129^{o}58.9361'W) on the Marker 33 diffuse vent site in Axial Volcano (**Figure 2.11**). In July 2010, TFM1 was tested on an *Alvin* dive to the Dead Dog vent field, Middle Valley, JdF during cruise AT15-67. During this cruise, TFM2 was deployed on 6 *Alvin* dives. We successfully completed 14 measurements at structures Hulk, Dante, Grotto in Main Endeavour, at Faulty Towers in Mothra, at Boardwalk structure in the High Rise vent field (all along the Endeavour segment), and at the Marker 55 structure in Axial Volcano (**Figure 2.11**).

Note that on some dives, measuring fluid temperature with *Alvin* temperature probe was not possible for reasons independent of our devices (e.g., malfunctions of *Alvin*'s temperature probe or recording system). We used temperature values (shown in red in **Table 2.3**) obtained on the same structure during different dives, for estimating heat output in such cases.

Table 2.3 Results of flow measurements performed by the TFM1 and TFM2 devices at the Endeavour, Axial Volcano, and at Middle Valley on the JdF ridge during the June 2009 (AT15-47) and July 2010 (AT15-67) *Alvin* cruises. Numbers in bold represent data from diffuse sources. On some dives measuring flow temperature with *Alvin* temperature probe was not possible. Temperature values in red represent results measured on different dives.

Structure **Cruise / Dive**	**Device**	***Alvin*** **coordinates X, Y, Z (m)**	**Mean velocity (cm/s)**	**T (°C)**	**Flow area (cm^2)**	**Flow rate (cm^3/s)**	**Heat output (MW)**
ENDEAVOUR SEGMENT (JdF)							
		Main Endeavour vent field					
Hulk							
AT15-67 / 4626	TFM2	5041, 6245, 2199	21.0	288	13	273	0.31
AT15-67 / 4626		5053, 6259, 2192	53.3	316	79	4208	5.32
AT 15-67 / 4627		5043, 6252, 2193	3.3	50	2400	7920	**1.58**
AT 15-67 / 4627		5042, 6252, 2193	9.7	50	200	1938	**0.39**
Dante							
AT15-47 / 4518	TFM1	4999, 6135, 2179	92.0	326	17	1564	2.039
AT15-47 / 4525		4966, 6167, 2179	104.0	326	79	8216	10.71
AT15-67 / 4626	TFM2	4966, 6163, 2181	38.7	326	79	3060	3.99
AT15-47 / 4518	TFM1	5005, 6168, 2194	8.0	50	2400	19200	**3.84**
Grotto							
AT15-67 / 4626	TFM2	4945, 6160, 2189	57.6	320	79	4548	5.82
AT15-67 / 4621		4933, 6154, 2187	17.8	327	9	160	0.21
AT15-67 / 4627		4945, 6160, 2190	5.6	50	300	1677	**0.34**
AT15-67 / 4627		4945, 6160, 2190	2.0	50	200	400	**0.08**
AT15-67 / 4627		4954, 6153, 2188	11.1	55	600	6672	**1.47**
		Mothra vent field					
Faulty Towers							
AT15-67 / 4628	TFM2	4156, 3297, 2278	33.3	322	314	10469	13.48
		High Rise vent field					
Godzilla							
AT15-47 / 4516	TFM1	5769, 8313, 2137	154.0	349	79	12166	16.98
Park Place							
AT15-47 / 4516	TFM1	5736, 8258, 2149	64.0	348	14	896	1.25
Between Fairy Castle & Ventnor							
AT15-47 / 4516	TFM1	5604, 8196, 2164	121.0	348	4	484	0.67
Fairy Castle							
AT15-47 / 4526	TFM1	5710, 8137, 2158	80.0	348	44	3520	4.90
Ventnor							
AT15-47 / 4526	TFM1	5602, 8201, 2163	113.0	332	79	8927	11.86
Boardwalk							
AT15-67 / 4623	TFM2	5786, 8290, 2134	24.1	364	20	482	0.70
AXIAL VOLCANO (JdF)							
MKR 55 (RAS)							
AT15-47 / 4521	TFM1	6538, 3681, 1520	7.7	20	1800	13860	**1.109**
AT15-67 / 4620	TFM2	6614, 3987, 1517	8.7	20	5000	43300	**3.46**
AT15-67 / 4620		6606, 3993, 1517	8.7	20	3500	30310	**2.42**
MIDDLE VALLEY							
		Dead Dog vent field					
AT15-67 / 4625	TFM1	4383, 1747, 2405	128.0	260	314	40192	41.80

The turbine designs were proven suitable for use in both medium-to-high temperature focused flow and low-temperature diffuse flow areas. With TFM2 we obtained a minimum velocity of 2 cm/s. To the best of our knowledge, this is the lowest flow rate ever measured at the JdF ridge. We obtained a velocity of 154 cm/s with TFM1 at a black smoker vent in High Rise during the June 2009 cruise.

Results obtained with our devices (**Table 2.3**) represent the first direct heat output measurements at the High Rise hydrothermal field, Endeavor segment.

2.6 Accuracy of Measurements

Accuracy of our measurements is affected by two main sources of error: (1) mechanical characteristics of the flow meters and (2) uncertainties associated with field conditions. Some inaccuracies of flow meters are typical even for ideal laboratory conditions, whereas others are specific for our designs.

Flow meter performance is often characterized by the factor $K = w/Q$ where Q is the flow rate and w is the frequency of rotation. For flow measurements in pipe systems, it is desirable to use a flow meter within its "linear" range, where K is approximately constant. Once the frequency of rotations is measured, the flow rate is simply obtained from $Q = w/K$. Typical flow meter design criteria require K to be approximately constant for flow rates in the range of $0.1Q_{max}$ to Q_{max}, where Q_{max} is the maximum designed flow rate. The K factor is specific for one set of fluid properties. Consequently, changes in temperature will affect both the viscosity and density of fluid, which may decrease the accuracy [*Cuthbert* and *Beck*, 1999]. For the turbine flow meters, the calibration curves shown in **Figure 2.10** show a strong linear relationship

between *w* and *v* (or equivalently *Q*), suggesting that these devices are operating within standard design specifications for such flow meters.

An important factor associated with field conditions that lead to inaccuracy of velocity measurements is the temperature difference between the lab calibration and field conditions. At elevated temperatures, the meter material undergoes thermal expansion, which may result in the deformation of its components. For black smoker measurements the density of hot hydrothermal fluid is approximately 40% lower than that of room temperature water we used in our calibration tests (Section 2.4). This may result in as much as a 15% error [*Baker*, 1993]. The high temperature of black smokers also yields lower kinematic viscosity. Its effect on the accuracy of the flow measurements is somewhat unclear, but it could result in an error of the same order as the density effect. Temperature variations are unlikely to compromise the structural stability of our devices though, since in industrial applications, flow meters made of the same or similar materials operate at temperatures varying from -270^{o} C to 650^{o} C and pressures ranging from nearly a vacuum to those exceeding 450 MPa. Overall, the error in measured velocity may be approximately 30% at black smokers because the field conditions are significantly different than the calibration conditions. The error in measurement of diffuse flow should be considerably smaller.

The numerous assumptions regarding conditions in the field are even more problematical, particularly for calculating heat flow. Fluid flow rates likely vary with time over tidal cycles and as a result of changes in the subsurface. Our instantaneous flow measurements are not able to capture these variations or obtain long-term mean flow

rates. The sampling of black smoker vents on large vent structures and throughout the vent field is incomplete, and to obtain estimates of heat flow on the vent structure or vent field scale requires extrapolation of the limited data set. Finally, black smoker velocities are translated to volumetric flow rates by assuming elliptic orifices and somewhat inaccurate estimates of orifice area. All of these issues result in an estimate of black smoker heat outputs that are likely accurate to within a factor of $\pm$ 50%.

Diffuse flow measurements have some of the same issues, but inaccurate assessment of the flow area of a diffuse flow patch and extrapolation to diffuse patches where measurement have not been made are likely the greatest source of error in determining heat output. **Figure 2.12** shows how we assess area of a diffuse flow patch and suggest that the estimates could differ by up to even 50%. As a result heat output estimates using these devices are uncertain by roughly a factor of two or more. Such uncertainties are similar to those estimated from both integrated and plume measurements [*Baker*, 2007].

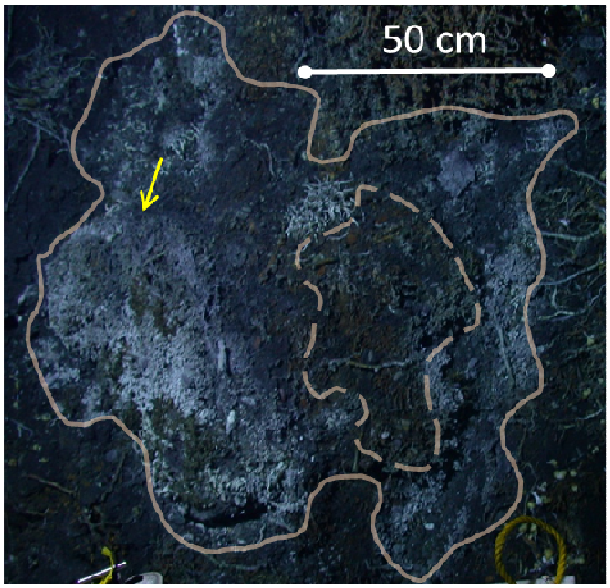

Figure 2.12 Diffuse flow site near Dante structure (Main Endeavour Vent Field, cruise AT 15-47, *Alvin* dive 4518, July 2009). TFM1 device was deployed at the position indicated by yellow arrow (X = 5005 m, Y = 6168 m, Z = 2194 m; **Table 2.3**). The device measured the flow velocity of 8.0 cm/sec (**Table 2.3**). White microbial mats visualize the area of diffuse venting, which is between the solid and dashed lines indicating its outer and inner borders. In addition, the shimmering water was distinctly observed above this area and was not visible outside, where no live biological activity could be detected. The area of this diffuse venting site was estimated to be 7100 cm^2 and used in equation (2.1). We carefully analyzed this site, and it is unlikely that any measurable diffuse flow is venting from the area inside the dashed perimeter, although it cannot be entirely excluded. If this area included in the calculation, the final result would differ by nearly 50%.

With cup anemometer measurements, another source of error can come from cross flow that distorts the flow of the plume past the anemometer wheel. **Figure 2.13** shows an example of such a situation. Measurements with TFM devices will not be significantly affected by such cross flow.

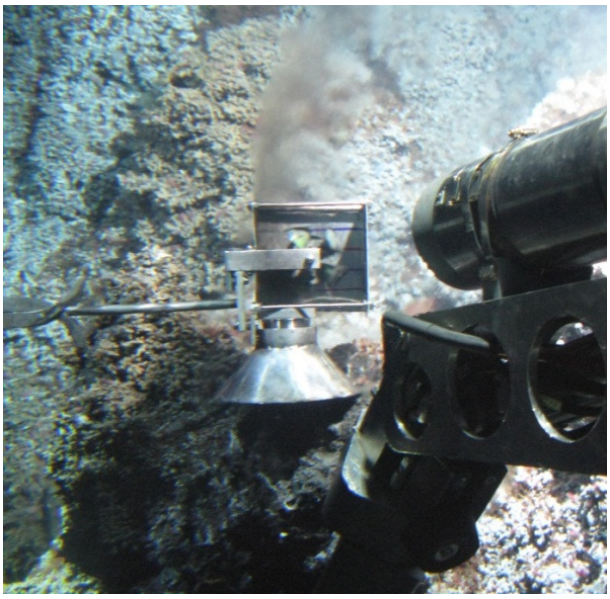

Figure 2.13 Deployment of the cup anemometer device over a black smoker orifice on *Alvin* dive 4414 to the Dante hydrothermal vent field (during AT 15-34 in July 2008).

Determining the true velocity of the fluid exiting the chimney is not trivial. Given the assumptions required in designing and implementing the device, these measurements can be considered to be within approximately 30% of the true vent velocity. Heat output data are likely to be uncertain by approximately a factor of two, when extrapolated to the vent field scale. Multiple measurements, at the same location, result in variance of heat flux typically within 15% as seen in **Table 2.3**, indicating that the devices provide some degree of precision. The data presented in this work are important, however, in that a wide range of velocities are presented. As a result relative velocities highlight the complex flow conditions at vent fields**.**

2.7 Conclusions

We designed, built, and calibrated a cup anemometer and two turbine flow meter devices for making instantaneous point measurements of both focused and diffuse fluid flows in seafloor hydrothermal systems. We have tested the devices on 24 dives from submersible *Alvin*, and obtained 63 separate measurements in total conducted at depths up to 2,400 m and at temperatures up to 364^{o} C. In field tests, the turbine flow meter devices provided measurements of hydrothermal flow between 2 and 154 cm/s. The cup anemometer device has operated successfully between 5 and 77 cm/s. The rate of 2 cm/s is the lowest ever measured at the JdF ridge, and the results obtained with our devices (**Table 2.3**) represent the first direct heat output measurements at High Rise hydrothermal field (Endeavour Segment) and Dead Dog vent field (Middle Valley) at JdF. While *Schultz et al*. [1992] conducted the first direct measurements of diffuse flow on the Peanut structure of the Main Endeavour field, we obtained the first measurements of the diffuse flow rates at most of the structures on the Northern Main Endeavor (Dante, Hulk, Grotto, and S&M).

The instruments we developed are simple, robust, relatively small, lightweight, self-contained devices that are able to measure quickly both high- and low-temperature fluid flows in a variety of hydrothermal settings. They are easy to assemble, disassemble, and maintain. They require significantly shorter amount of deployment time (usually a few minutes) for accurate measurements, than most of the previously developed instruments [e.g., *Sarrazin et al.,* 2009; *Schultz,* 1992, 1996].

A particularly attractive feature of our turbine flow meters is their open-bearing design. We did not notice any damage created by the accumulation of particles or chemical precipitates on the bearings even after many deployments as the open design allowed the fluids to flush through the system easily. This quality makes the developed devices, particularly, turbine flow meters, promising for long-term deployment.

In their present configuration these devices cannot be used for remote data collection or long-term deployment because they do not incorporate electronic recording mechanisms, onboard cameras, and internal temperature or chemical sensors. The TFM devices could easily incorporate a variety of electronic sensors, however, due to the robust modular design.

In summary, the devices discussed in this paper provide reliable results over a two-order of magnitude range of flow velocities and, hence, can be used to explore a broad range of heat and chemical fluxes at oceanic spreading centers. Such data are sorely lacking at present and the availability of these devices for use on manned submersibles and ROVs fills an important niche in the arsenal of tools for understanding seafloor hydrothermal systems.

2.8 References

ASTM Standard Handbook (2005), vol. 1, *Properties and Selection: Irons, Steels, and High Performance Alloys*, ASTM International, West Conshohocken, PA.

ASTM Standard A313 / A313M - 10e1, *Standard Specification for Stainless Steel Spring Wire*, ASTM International, West Conshohocken, PA.

ASTM Standard B265 – 11, *Standard Specification for Titanium and Titanium Alloy Strip, Sheet, and Plate*, ASTM International, West Conshohocken, PA.

Baker, E.T. (1994), A 6-year time series of hydrothermal plumes over the Cleft segment of the Juan de Fuca Ridge, *Journal of Geophysical Research, 99*(B3), 4889-4904.

Baker, E.T. (2007), Hydrothermal cooling of Mid-Ocean Ridge axes: Do measured and modeled heat fluxes agree?, *Earth and Planetary Science Letters, 263*(1-2), 140-150.

Baker, E.T., and G.J. Massoth (1987), Characteristics of hydrothermal plumes from two vent fields on the Juan de Fuca Ridge, Northeast Pacific Ocean, *Earth and Planetary Science Letters, 85,* 59-73.

Baker, E.T., G.J. Massoth, S.L. Walker, and R.W. Embley (1993), A method for quantitatively estimating diffuse and discrete hydrothermal discharge, *Earth and Planetary Science Letters, 118*(1-4), 235-249.

Baker, E.T., G.J. Massoth, R.A. Feely, G.A. Cannon, and R.E. Thomson (1998), The rise and fall of the CoAxial hydrothermal site, 1993-1996, *Journal of Geophysical Research, 103*(B5), 9791-9806.

Baker, R.C. (1993), Turbine flowmeters: II. Theoretical and experimental published information, *Flow Measurement and Instrumentation, 4*(3), 123-144.

Baker, R.C. (2000), *Flow Measurement Handbook: Industrial Designs, Operating Principles, Performance, and Applications*, Cambridge University Press, Cambridge, England.

Bemis, K.G., R.P. Von Herzen, and M.J. Mottl (1993), Geothermal heat flux from hydrothermal plumes on the Juan de Fuca Ridge, *Journal of Geophysical Research, 98,* 6351-6365.

Butterfield, D.A., K.K. Roe, M.D. Lilley, J.A. Huber, J.A. Baross, R.W. Embley, and G.J. Massoth (2004), Mixing, reaction and microbial activity in the subseafloor revealed by temporal and spatial variation in diffuse flow vents at Axial Volcano, *Geophysical Monograph, 144,* 269-289.

Camilli, R., D. Di Iorio, A. Bowen, C.M. Reddy, A.H. Techet, D.R. Yoerger, L.L. Whitcomb, J.S. Seewald, S.P. Sylva, and J. Fenwick (2011), Acoustic measurement of the Deepwater Horizon Macondo well flow rate, pp. 1-5, Proceedings of the National Academy of Sciences, USA.

Chen, C.J., and W. Rodi (1980), *Vertical Turbulent Buoyant Jets: A Review of Experimental Data*, Pergamon Press, New York.

Converse, D.R. (1985), Flow rates in the East Pacific Rise (21°N) hot springs, and numerical investigations of two regimes of hydrothermal circulation, Ph.D. thesis, 462 pp., Harvard University, Cambridge, Massachusetts.

Converse, D.R., H.D. Holland, and J.M. Edmond (1984), Flow rates in the axial hot springs of the East Pacific Rise (21°N): Implications for the heat budget and the formation of massive sulfide deposits, *Earth and Planetary Science Letters, 69,* 159-175.

Corliss, J.B., J. Dymond, L.I. Gordon, J.M. Edmond, R.P. Von Herzen, R.D. Ballard, K. reen, D. Williams, A. Bainbridge, K. Crane, and T.H. Van Andel (1979), Submarine thermal springs on the Galapagos Rift, *Science, 203*(4385), 1073-1083.

Crone, T.J., and M. Tolstoy (2010), Magnitude of the 2010 Gulf of Mexico oil leak, *Science, 330*(6004), 634.

Cuthbert, M., and S. Beck (1999), A non-dimensional method to increase the accuracy of turbine flowmeters, Proceedings of the Institution of Mechanical Engineers, Part E, *Journal of Process Mechanical Engineering, 213*(2), 121-126.

Di Iorio, D., D. Lemon, and R. Chave (2005), A self-Contained acoustic scintillation instrument for path-averaged measurements of flow and turbulence with application to hydrothermal vent and bottom boundary layer dynamics, *Journal of Atmospheric and Oceanic Technology, 22*(10), 1602-1617.

Di Iorio, D., J.W. Lavelle, P.A. Rona, K. Bemis, G. Xu, L.N. Germanovich, R.P. Lowell, and G. Genc (2012), Measurements and models of heat flux and plumes from hydrothermal discharges near the deep sea floor, *Oceanography, 25*(1), 169-179.

Dymond J., E. Baker, and J. Lupton (1988), Plumes: Ocean limb of seafloor hydrothermal systems, The Mid-Ocean Ridge - A Global Dynamic System, Proceedings of the Salishan Workshop, National Academy of Sciences, pp. 209-231, National Academy Press, Washington, D.C.

Edmond, J.M., J.B. Corliss, and L.I. Gordon (1979), Ridge crest-hydrothermal metamorphism at the Galapagos spreading center and reverse weathering, In Deep Drilling Results in the Atlantic Ocean: Ocean Crust, (eds. M. Talwani et al.) *Amer. Geophys. Union, Ewing Series, 2,* 383-390.

Elderfield, H., R. Mills, and M. Rudnicki (1993), Geochemical and thermal fluxes, high-temperature venting and diffuse flow from Mid-Ocean Ridge hydrothermal systems: the TAG hydrothermal field, Mid-Atlantic Ridge 26^{o}N, *Geological Society, London, Special Publications, 76*(1), 295.

Fischer, H.B., E.J. List, R.C.Y. Koh, J. Imberger, and N.H. Brooks (1979), *Mixing in Inland and Coastal Waters*, pp. 315-389, Academic, San Diego, Calif.

Futrell, J.C. (1989), Bucket wheel assembly for a flow measuring device, US Patent 4,866,985.

Ginster, U., M.J. Mottl, and R.P. Von Herzen (1994), Heat flux from black smokers on the Endeavour and Cleft Segments, Juan de Fuca Ridge, *Journal of Geophysical Research, 99,* 4937-4950.

Gendron, J.F., J.F. Todd, R.A. Feely, E.T. Baker, and D.C. Kadko (1994), Excess 222Rn above the Cleft segment of the Juan de Fuca Ridge, *Journal of Geophysical Research, 99*(B3), 5007-5015.

Germanovich, L.N., G. Genc, R.P. Lowell, and P.A. Rona (2012), Deformation and surface uplift associated with serpentinization at mid-ocean ridges and subduction zones, *J. Geophys. Res.,* accepted.

Glickson, D.A., D.S. Kelley, and J.R. Delaney (2007), Geology and hydrothermal evolution of the Mothra hydrothermal field, Endeavour Segment, Juan de Fuca Ridge, *Geochemistry Geophysics Geosystems, 8*(6), Q06010.

Jackson, D.R., C.D. Jones, P.A. Rona, and K.G. Bemis (2003), A method for Doppler acoustic measurement of black smoker flow fields, *Geochemistry, Geophysics, Geosystems, 4*(11), 1095.

Johnson, H.P., and M.J. Pruis (2003), Fluxes of fluid and heat from the oceanic crustal reservoir, *Earth and Planetary Science Letters, 216*(4), 565-574.

Kadko, D. (1993), An assessment of the effect of chemical scavenging within submarine hydrothermal plumes upon ocean geochemistry, *Earth and Planetary Science Letters, 120*(3-4), 361-374.

King, L.V. (1914), On the convection of heat from small cylinders in a stream of fluid: determination of the convection constants of small platinum wires with applications to hot-wire anemometry, *Mathematical or Physical Character, 214,* 373-432.

Liu, L., and R.P. Lowell (2009), Models of hydrothermal heat output from a convecting, crystallizing, replenished magma chamber beneath an oceanic spreading center, *J. Geophys. Res., 114,* B02102, doi:10.1029/2008JB005846.

Little, S.A., K.D. Stolzenbach, and R. P. Von Herzen (1987), Measurements of plume flow from a hydrothermal vent field, *Journal of Geophysical Research, 92*(B3), 2587-2596.

Lowell, R.P. (2010), Hydrothermal circulation at slow spreading ridges: Analysis of heat sources and heat transfer processes, In *Diversity of Hydrothermal Systems on Slow Spreading Ocean Ridges, Geophys. Monogr. Ser., 188* (eds. P.A. Rona, C. Devey, J. Dyment, and B. Murton), 11-26, AGU, Washington, D.C., doi:10.1029/2008GM000758.

Lowell, R.P., and L.N. Germanovich (1994), On the temporal evolution of high-temperature hydrothermal systems at ocean ridge crests, *J. Geophys. Res., 99,* 565-575.

Lowell, R.P., and L.N. Germanovich (2004), Hydrothermal processes at mid-ocean ridges: Results from scale analysis and single-pass models, *Geophysical Monograph, 148,* 219-244.

Macdonald, K.C., K. Becker, F.N. Spiess, and R.D. Ballard (1980), Hydrothermal heat flux of the "black smoker" vents on the East Pacific Rise, *Earth and Planetary Science Letters, 48,* 1-7.

McDuff, R.E., Physical dynamics of deep-sea hydrothermal plumes, in Seafloor Hydrothermal Systems, edited by S.E.Humphris, R.A. Zierenberg, L.S. Mullineaux, and R.E. Thomson, pp. 357-368, AGU, Washington, D.C., 1995.

Merle, S. (2011), NeMO Cruise Report Endeavour Segment and Axial Seamount, Juan de Fuca Ridge.

Metaxas, A. (2001), Behaviour in flow: perspectives on the distribution and dispersion of meroplanktonic larvae in the water column, *Canadian Journal of Fisheries and Aquatic Sciences, 58*(1), 86-98.

Merzkirch, W. (2005), *Fluid Mechanics of Flow Metering*, Springer, New York.

Middleton, J.H., and R.E. Thomson (1986), Modeling the rise of hydrothermal plumes, *Can. Tech. Rep. Hydrogr. Ocean. Sci., 69,* 1-18.

Morton, B., G. Taylor, and J. Turner (1956), Turbulent gravitational convection from maintained and instantaneous sources, *Mathematical and Physical Sciences, 234*(1196), 1.

Munson, B.R., D.F. Young, and T.H. Okiishi (2005), *Fundamentals of Fluid Mechanics*, 5th edition, 816 pp., Wiley and Sons, New York.

Murton, B.J., L.J. Redbourn, C.R. German, and E.T. Baker (1999), Sources and fluxes of hydrothermal heat, chemicals and biology within a segment of the Mid-Atlantic Ridge, *Earth and Planetary Science Letters, 171*(2), 301-317.

Ostashev, V. (1994), Sound propagation and scattering in media with random inhomogeneities of sound speed, density and medium velocity, *Waves in Random Media, 4*(4), 403-428.

Palmer, D.R. (2005), Acoustical scattering from constituents of an ocean plume located near a boundary surface, *Geoscience and Remote Sensing, 43*(4), 770-777.

Papanicolaou, P.N. and E.J. List (1987), Statistical and spectral properties of tracer concentrations in round buoyant jets, *Int. J. Heat Mass Transfer, 30*, 2059-2071.

Ramondenc, P. (2008), Effect of seismicity and diking on hydrothermal circulation at Mid-Ocean Ridges, Ph.D. thesis, Georgia Institute of Technology, Atlanta.

Ramondenc, P., L.N. Germanovich, K.L. Von Damm, and R.P. Lowell (2006), The first measurements of hydrothermal heat output at 9°50'N, East Pacific Rise, *Earth and Planetary Science Letters, 263,* 140-150.

Riley, J.P., G. Skirrow, and R. Chester (1975), *Chemical Oceanography*, Academic Press, New York.

Robigou, V., J.R. Delaney, and D.S. Stakes (1993), Large massive sulfide deposits in a newly discovered active hydrothermal system, The High Rise Field, Endeavour Segment, Juan De Fuca Ridge, *Geophysical Research Letters, 20*(17), 1887-1890.

Rona, P.A., and D.A. Trivett (1992), Discrete and diffuse heat transfer at ASHES vent field, Axial Volcano, Juan de Fuca Ridge, *Earth and Planetary Science Letters, 109,* 57-71.

Ross, T. and R. Lueck (2003), Sound scattering from oceanic turbulence, *Geophys. Res. Lett., 30,* 1344-1347.

Rudnicki, M., and H. Elderfield (1992), Theory applied to the Mid-Atlantic Ridge hydrothermal plumes: The finite-difference approach, *Journal of Volcanology and Geothermal Research, 50*(1-2), 161-172.

Sarrazin, J., P. Rodier, M.K. Tivey, H. Singh, A. Schultz, and P.M. Sarradin (2009), A dual sensor device to estimate fluid flow velocity at diffuse hydrothermal vents, *Deep Sea Research Part I: Oceanographic Research Papers, 56*(11), 2065-2074.

Schultz, A., J.R. Delaney, and R.E. McDuff (1992), On the partitioning of heat flux between diffuse and point source seafloor venting, *Journal of Geophysical Research, 97*(B9), 12299-12314.

Schultz, A., P. Dickson, and H. Elderfield (1996), Temporal variations in diffuse hydrothermal flow at TAG, *Geophysical Research Letters, 23*(23), 3471-3474.

Speer, K.G., and P.A. Rona (1989), A model of an Atlantic and Pacific hydrothermal plume, *J. Geophys. Res., 94,* 6213-6220.

Spiess, F.N., et al. (1980), East Pacific Rise: Hot Springs and Geophysical Experiments, *Science, 207,* 1421−1433.

Stein, J.S., and A.T. Fisher (2001), Multiple scales of hydrothermal circulation in Middle Valley, Northern Juan de Fuca Ridge - Physical constraints and geologic models, *Journal of Geophysical Research, 106*(B5), 563-580.

Stommel, H. (1982), Is the South Pacific helium-3 plume dynamically active?, *Earth and Planetary Science Letters, 61*(1), 63-67.

Tennekes, H., and J.L. Lumley (1972), *A First Course in Turbulence*, MIT Press, Cambridge, Mass.

Thomson, R.E., M.M. Subbotina, and M.V. Anisimov (2005), Numerical simulation of hydrothermal vent-induced circulation at Endeavour Ridge, *Journal of Geophysical Research, 110*(C1), C01004.

Thomson, R.E., S.F. Mihály, A.B. Rabinovich, R.E. McDuff, S.R. Veirs, and F.R. Stahr (2003), Constrained circulation at Endeavour Ridge facilitates colonization by vent larvae, *Nature, 424*(6948), 545-549.

Thomson, R.E., J.R. Delaney, R.E. McDuff, D.R. Janecky, and J.S. McClain (1992), Physical characteristics of the Endeavour ridge hydrothermal plume during July 1998, *Earth and Planetary Science Letters, 111,* 141-154.

Turner, J. (1986), Turbulent entrainment: The development of the entrainment assumption, and its application to geophysical flows, *J. Fluid Mech, 173*(431), 71.

Turner, J. (1973), Convection in the mantle: A laboratory model with temperature-dependent viscosity, *Earth and Planetary Science Letters, 17*(2), 369-374.

Van Dover, C.L., and R.A. Lutz (2004), Experimental ecology at deep-sea hydrothermal vents: a perspective, *Journal of Experimental Marine Biology and Ecology, 300*(1-2), 273-307.

Vaughn, E.C., J.M. Fulford, and H.R. Myers (2006), Bucket wheel assembly for fluid flow meters, US Patent 7,017,425 B1.

Veirs, S.R., R.E. McDuff, and F.R. Stahr (2006), Magnitude and variance of near-bottom horizontal heat flux at the Main Endeavour hydrothermal vent field, *Geochemistry Geophysics Geosystems, 7,* 1-16.

Von Damm, K.L., and M.D. Lilley (2004), Diffuse flow hydrothermal fluids from 9°50'N East Pacific Rise: Origin, evolution and biogeochemical controls, *Geophysical Monograph, 144,* 245-268.

Wankel, S.D., L.N. Germanovich, D.L. Marvin, G. Genc, C.J. DiPerna, A.S. Bradley, E.J. Olson, and P.R. Girguis (2011), Influence of subsurface biosphere on geochemical fluxes from diffuse hydrothermal fluids, *Nature Geoscience, 4,* 461-468.

Webster, J.G. (1999), *The Measurement, Instrumentation, and Sensors Handbook*, Springer, New York.

Wheat, C.G., P. Fryer, S. Hulme, N. Becker, A. Curtis, and C. Moyer (2003), Hydrothermal venting in the southern most portion of the Mariana backarc spreading center at 12.57°N, *EOS Trans. AGU, 84,* Fall Meet. Suppl., abstr. T32A-0920.

Xu, G. (2010), The Investigation of Hydrothermal Plumes by the Acoustic Scintillation Method, Ph.D. thesis, University of Georgia, Athens, GA.

Xu, G., and D. Di Iorio (2011), The relative effects of particles and turbulence on acoustic scattering from deep-sea hydrothermal vent plumes, *The Journal of the Acoustical Society of America, 130,* 1856.

Yoerger, D., J. Newman, and J.J. Slotine (1986), Supervisory control system for the Jason ROV, *IEEE J. Oceanic Eng., 11*(3), 392-400.

Appendix 2A. Details of Device Specifications

We built our heat flow measuring devices by using the specifications shown in **Figures 2A.1** through **2A.5**.

Figure 2A.1 shows the details of the assembly of the cup anemometer: the paddle wheel (**Figure 2A.1a**), the main support frame (**Figure 2A.1b**), and the shield with supporting rods (**Figures 2A.1c and 2A.1d**).

Top and face views of the TFM1 device are given in **Figures 2A.2a** and **2A.2b**, respectively. **Figure 2A.3** shows the pictures of all the major components of TFM1 including upper and lower bearing supports, rotor assembly, main body (flow pipe), pipe adapter, sapphire bearing, and compression and disk springs.

The assembled TFM2 device is displayed in **Figure 2A.4** together with the inset picture showing the connection of the upper bearing support to the shaft of the rotor. Finally, the details of the TFM2 components are shown in **Figure 2A.5** including the flow tube (**Figure 2A.5a**), the spider carrying the lower bearing support (**Figure 2A.5b**), the upper bearing support (**Figure 2A.5c**), the impeller (rotor) shaft (**Figure 2A.5d**).

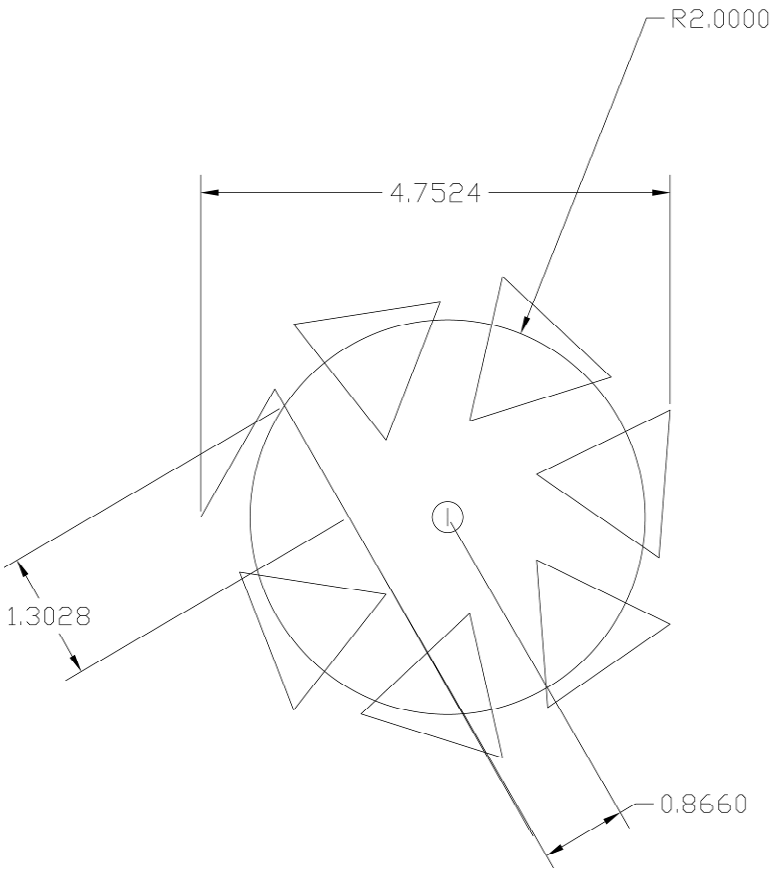
R2.0000
4.7524
1.3028
0.8660

(a)

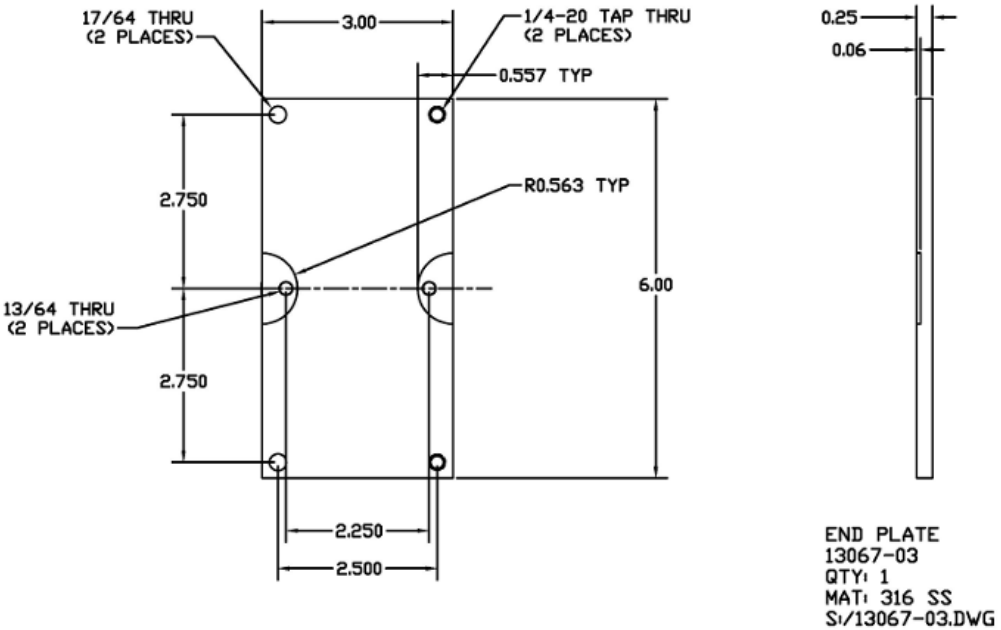
17/64 THRU
(2 PLACES)
3.00
1/4-20 TAP THRU
(2 PLACES)
0.557 TYP
R0.563 TYP
2.750
6.00
13/64 THRU
(2 PLACES)
2.750
2.250
2.500
0.25
0.06
END PLATE
13067-03
QTY: 1
MAT: 316 SS
S:/13067-03.DWG

(b)

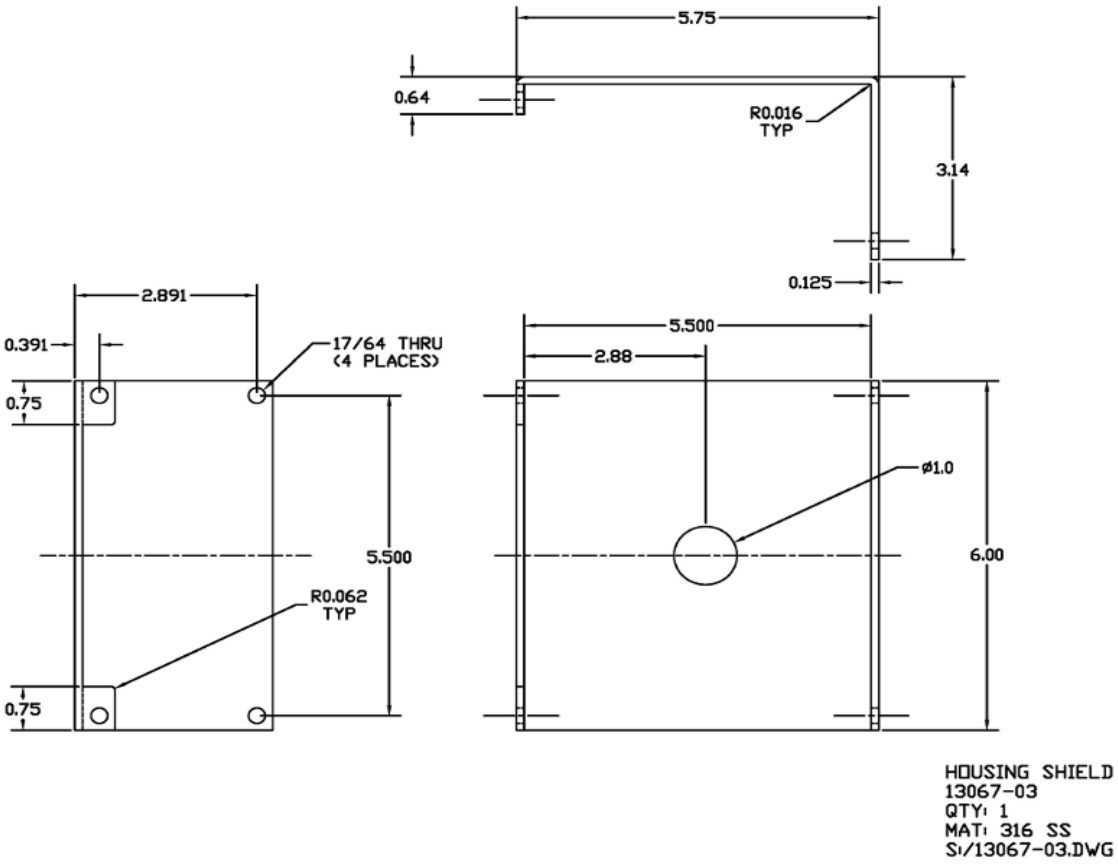

(c)

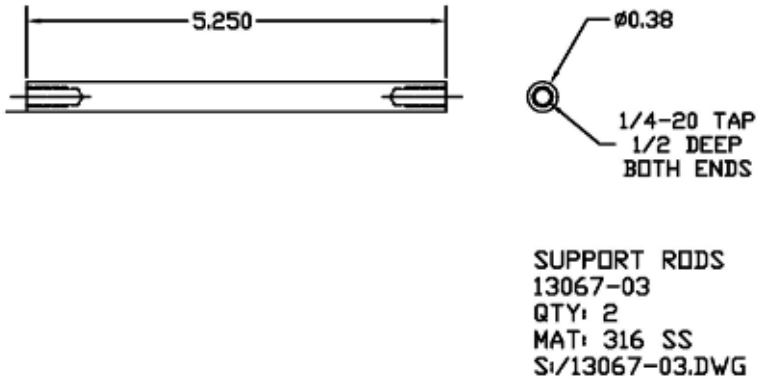

(d)

Figure 2A.1 Principle components of the cup anemometer device: **(a)** the paddle wheel, **(b)** the main support frame, **(c)** the shield, and **(d)** the supporting rods. All dimensions are given in inches.

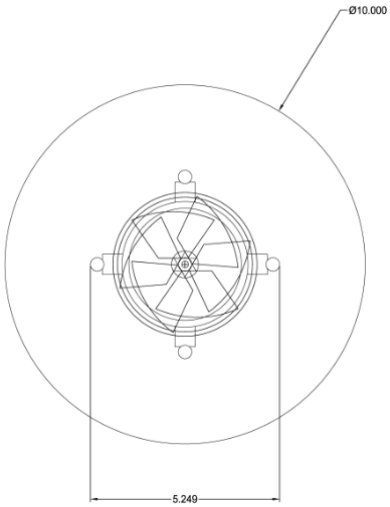

(a)

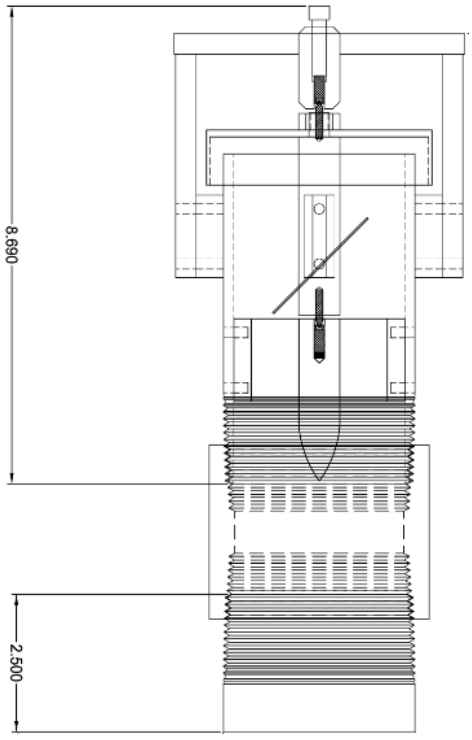

(b)

Figure 2A.2 (a) Top and **(b)** face views of the TFM1 device. Dimensions are given in inches.

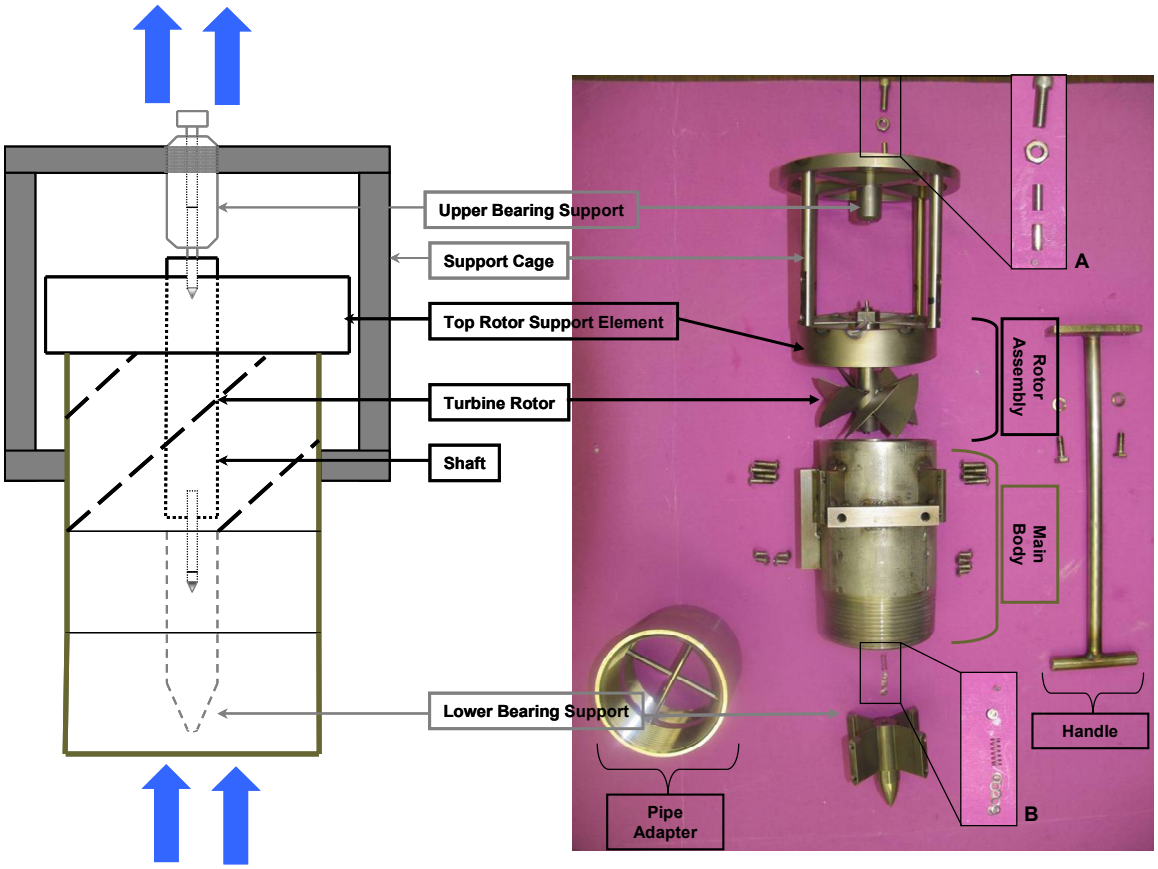

Figure 2A.3 Disassembled device TFM1. TFM1 components include upper and lower bearing supports, turbine rotor assembly, sapphire bearings (on insets A and B), flow pipe (main body), pipe adapter, and springs.

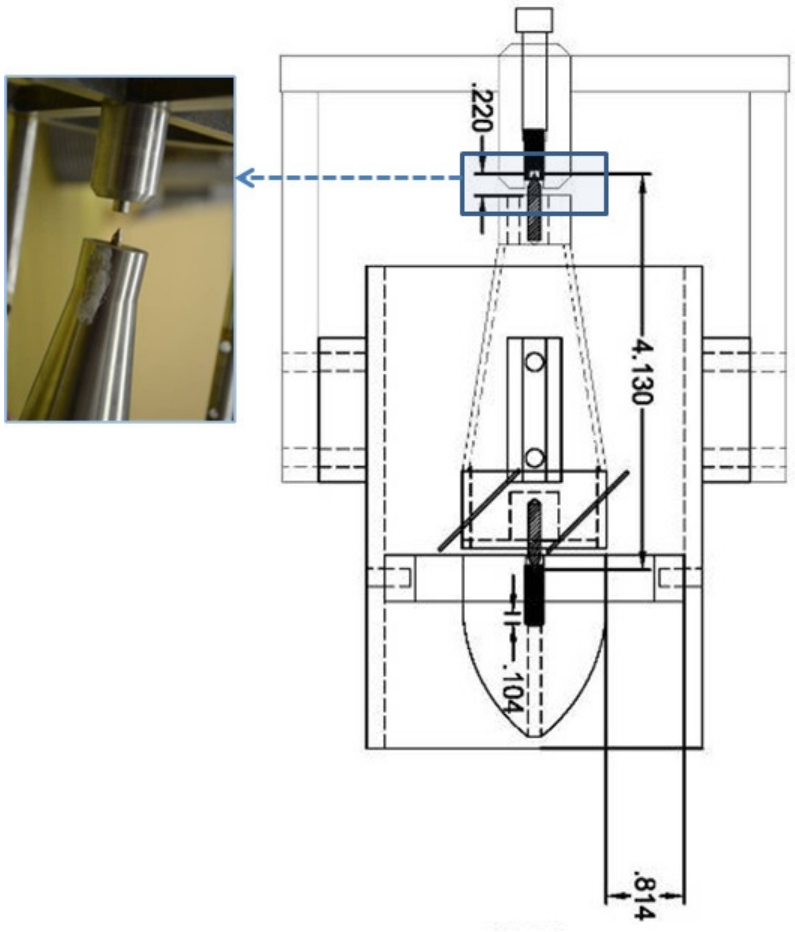

Figure 2A.4 TFM2 device. The inset shows the close up view of the upper bearing support and its connection to the impeller shaft. All the dimensions are given in inches.

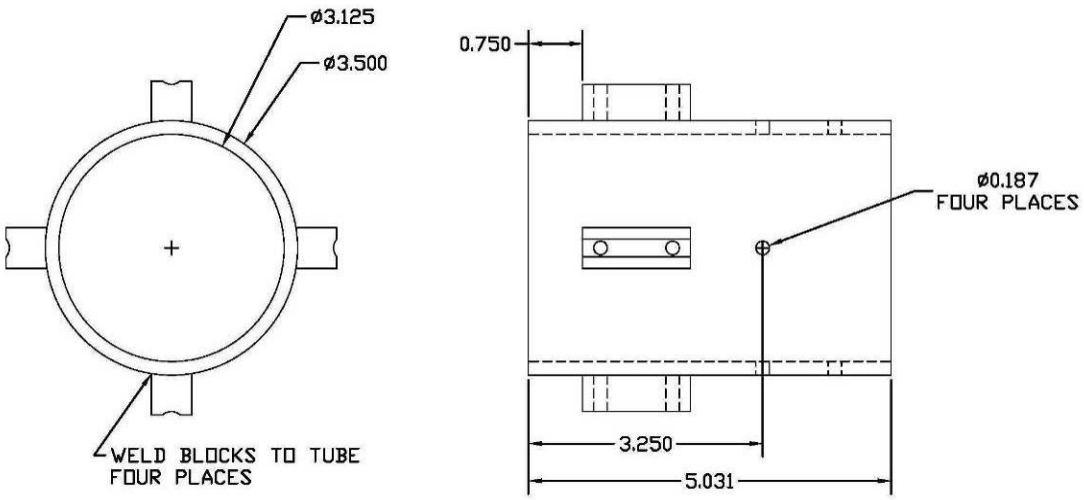
ø3.125
ø3.500
WELD BLOCKS TO TUBE
FOUR PLACES
0.750
ø0.187
FOUR PLACES
3.250
5.031

(a)

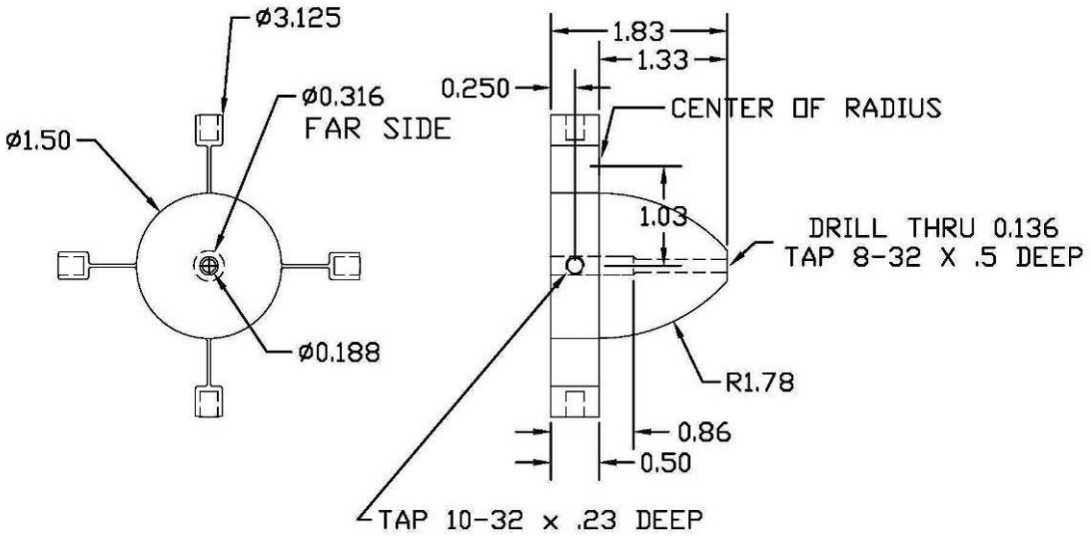
ø3.125
ø0.316
FAR SIDE
ø1.50
ø0.188
1.83
1.33
0.250
CENTER OF RADIUS
1.03
DRILL THRU 0.136
TAP 8-32 X .5 DEEP
R1.78
0.86
0.50
TAP 10-32 x .23 DEEP

(b)

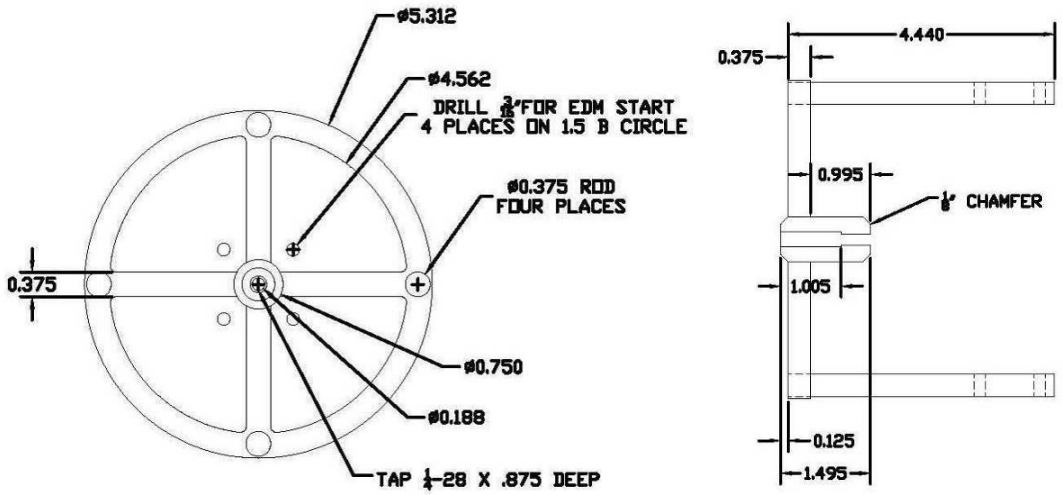

(c)

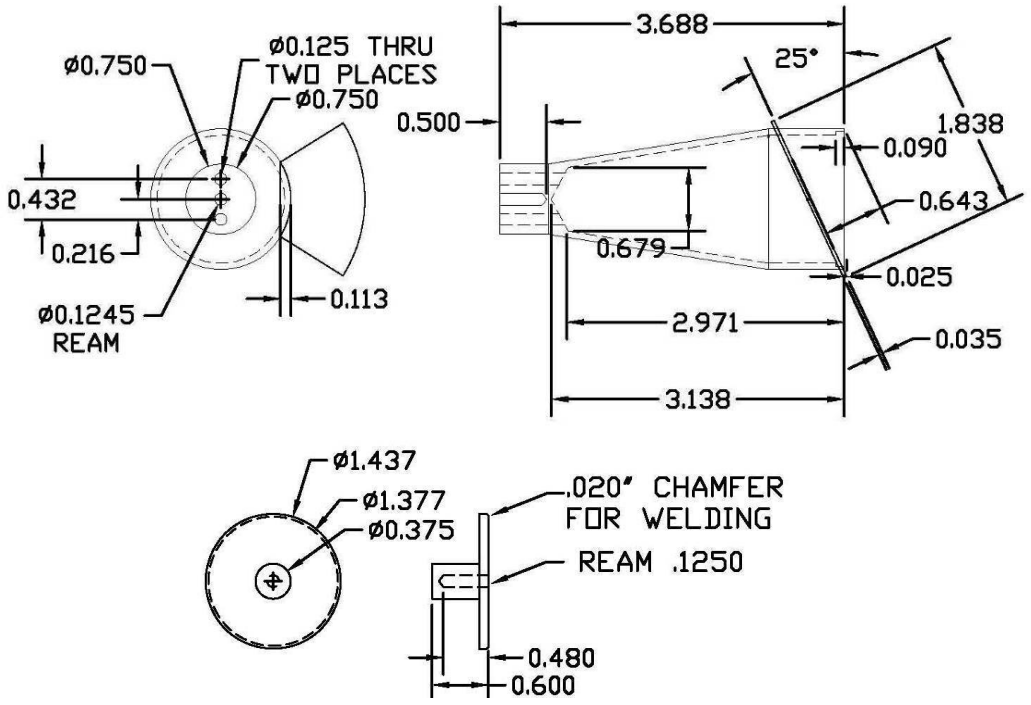

(d)

Figure 2A.5 Top and side views of TFM2 components: **(a)** the cylindrical tube assembly, **(b)** the lower bearing support, and spider, **(c)** the upper bearing elements (turn flange and upper support frame from top to bottom), **(d)** the rotor (impeller) elements (impeller shaft and cap from top to bottom).

CHAPTER 3

DIRECT MEASUREMENTS OF HYDROTHERMAL FLOW AND HEAT FLUX AT THE ENDEAVOUR SEGMENT, JUAN DE FUCA RIDGE

Abstract. Fluid flow and heat flux are key parameters for constraining models of hydrothermal circulation at oceanic spreading centers. In particular, point measurements of heat and fluid flow from both focused and diffuse flow sites are essential for understanding the partitioning of heat flow and more importantly for determining geochemical fluxes. Geochemical fluxes from seafloor hydrothermal systems not only provide key input into models of geochemical cycling between the ocean and lithosphere but also exert controls on the nature and evolution of both microbial and macrofaunal ecosystems. We present 58 new measurements of diffuse and focused fluid flow and estimates of heat flux at various structures along the Endeavour segment of the Juan de Fuca (JdF). These data yield robust estimates of high-temperature heat output from large vent structures such as Dante, Hulk and Grotto and permit extrapolation to total advective heat output from the Main Endeavour Field (MEF). The results suggest that heat output from the MEF may have declined in the wake of 1999 eruption at JdF. Our fluid flow data from diffuse sites have been used to produce the first estimates of geochemical fluxes on an active sulfide structure called "Finn" in the Mothra hydrothermal vent field. Finally, we present the first direct flow measurements from the High Rise and Mothra hydrothermal fields on the JdF.

3.1 Introduction

Hydrothermal circulation is an important mechanism for the transport of heat from the oceanic crust to the overlying ocean. Approximately 70% of the total heat loss through the deep oceans and marginal basins mainly by the creation of lithosphere from the Earth's surface is transported through the oceanic crust [*Sclater et al.,* 1980], and ~30% of global heat loss occurs as a result of hydrothermal venting [*Williams and Von Herzen,* 1974; *Morton and Sleep,* 1985; *Stein and Stein,* 1994; *Stein et al.,* 1995; *Elderfield and Schultz,* 1996]. Much of the hydrothermal heat loss occurs as low temperature discharge as the lithosphere ages, whereas approximately 10% of the total hydrothermal heat loss occurs by high-temperature venting near oceanic spreading centers [*Elderfield and Schultz,* 1996]. Low temperature diffuse discharge also occurs within vent fields, often in close proximity to high-temperature focused venting [e.g., *Edmond et al.,* 1979; *Corliss et al.,* 1979; *Von Damm and Lilley,* 2004].

Although the global estimates of hydrothermal heat transfer are important, quantification of hydrothermal heat loss at the vent field scale as well as from individual high-temperature point sources and low-temperature diffuse flow patches are also needed. Along the ~70,000 km of ocean ridges, there may be $\sim 10^3$ active high-temperature vent sites, of which ~300 have been identified [*Baker and German,* 2004]. Hydrothermal heat flow measurements have been made at only ~10% of the known sites [see **Table 1** from *Baker,* 2007 and *Lowell et al.,* 2008].

Heat flow measurements at the vent field scale provide crucial constraints on important physical parameters and hence on mathematical and numerical models of

magma-driven hydrothermal circulation at oceanic spreading centers. These parameters include: the permeability of young igneous oceanic crust, which cannot be reliably determined by other means [*Lowell and Germanovich,* 1994, 2004; *Wilcock and Nabb,* 1996; *Lowell,* 2010]; the thickness of the conductive boundary layer [e.g., *Lister,* 1983; *Lowell and Rona,* 1985; *Lowell and Burnell,* 1991; *Lowell and Germanovich,* 1994, 2004]; total mass flow rate [*Lowell and Germanovich,* 2004]; and rates of magma replenishment [*Liu and Lowell,* 2009; *Lowell,* 2010]. Quantification of heat through the axis and the flanks can also constrain geophysical models of crustal thermal balance [*Baker,* 2007]. Heat and mass flux at individual vents and diffuse flow sites provide critical information on the partitioning of heat flow and on the fluxes of important chemical constituents through the crust and into the ocean. Hydrothermal circulation is an important component of Earth's global geochemical cycles [e.g., *Wolery and Sleep,* 1976; *Edmond et al.,* 1979; *Thompson,* 1983], and the transport of chemical species such as H_2S, CO_2, and CH_4 by hydrothermal fluids supports a rich microbial biosphere [*Butterfield et al.,* 1997; *Jannasch,* 1995; *Karl,* 1995] and a hierarchy of benthic and near-bottom organisms [e.g., *Grassle,* 1985, 1986; *Lutz,* 1988; *Roth and Dymond,* 1989; *Cowen et al.,* 1990; *Tunnicliffe,* 1991; *Burd et al.,* 1992].

Heat flow measurements at the vent field scale can be divided into two types: (a) integrated heat flow measurements carried out in neutrally buoyant plumes that rise several hundred meters above the vent field [e.g., *Baker and Massoth,* 1987; *Thomson et al.,* 1992] or in a finite box surrounding the vent field through which horizontal and vertical fluxes can be measured [e.g., *Veirs et al.,* 2006], and (b) discrete measurements

performed at or nearby individual vent chimneys and diffuse flow sites, the results of which are summed and usually extrapolated to predict total heat flux either from a known sulfide edifice or vent field [*Bemis et al.,* 1993; *Ginster et al.,* 1994; *Schultz et al.,* 1992; *Ramondenc et al.,* 2006]. Details of heat flow measuring methods and devices are presented in Chapter 2 and in *Germanovich et al*. [2012].

Although a considerable number of discrete measurements at black smoker vents have been made over the last three decades [e.g., *Macdonald et al.,* 1980; *Converse et al.,* 1984; *Rona and Trivett,* 1992; *Ginster et al.,* 1994; *Ramondenc et al.,* 2006], relatively few measurements of diffuse flow are available [e.g., *Rona and Trivett,* 1992; *Schultz et al.,* 1992, 1996; *Pruis and Johnson,* 2004; *Ramondenc et al.,* 2006; *Sarrazin et al.,* 2009]. Measurements of diffuse flow and assessments of its impact on hydrothermal fluxes are difficult because the flow velocities are small and discharge environments are complex. Diffuse flow may occur through isolated cracks or through a fine network of cracks that extend over areas having meters to tens of meters diameter on the sea floor; it may also seep through the base and sides of chimneys and larger sulfide structures [*Bemis et al.,* 1993; *Rona and Trivett,* 1992; *Baker et al.,* 1993, *Ginster et al.,* 1994]. As a result, there is a wide range of estimates for heat partitioning. At East Pacific Rise 9°50'N [*Ramondenc et al.,* 2006] and Axial Seamount Hydrothermal Emissions Study (ASHES) vent field on the JdF [*Rona and Trivett,* 1992], diffuse flow may account for ~90% of the total heat output. At the Main Endeavour vent field (MEF) on the JDF *Schultz et al.* [1992] estimated that diffuse flow dominates focused flow by an

approximate ratio of 10:1; whereas *Veirs et al.* [2006] argue for an equal partitioning between diffuse and focused flow.

In this chapter, we shall report results from direct measurements of hydrothermal fluid flow and heat output on four seafloor expeditions (AT15-34 and AT15-36 in 2008, and AT15-47 in June 2009, and AT15-67 in July 2010). Most of the measurements come from the MEF; however, data were also collected from Mothra and High Rise vent fields on the Endeavour segment. Measurements were made on individual high-temperature orifices as well as on patches of diffuse flow. The measurements were made with a cup anemometer device (CA) on the first two cruises and with turbine flow meters (TFM1 and TFM2) on the latter two cruises. One goal of these measurements was to test new point measurement devices, which was successful (see Chapter 2). In Section 3.2 we describe the geologic setting of the three vent fields for which we have obtained heat output data. In Section 3.3, we describe the flow devices and data analysis. In Section 3.4, we present the main results. In Section 3.5, we show that the data are sufficient to characterize the total high-temperature heat output at several of the larger sulfide structures such as Dante, Hulk, and Grotto at the MEF and compared these estimates with those obtained in the plumes [*Ginster et al.,* 1994; *Bemis et al.,* 1993]. We also extrapolate our data set to estimate the total high-temperature heat output of MEF and the partitioning between focused and diffuse flow. We then discuss our heat output data for High Rise and Mothra. Finally, our direct estimates of fluid flow were coupled with concurrent volatile fluid concentrations, obtained by using an *in-situ mass spectrometry*, to quantify the hydrothermal

geochemical flux of some volatile compounds such as H_2, CH_4 and $CO_{2(aq)}$ among diffuse and focused flows, at Dante and Hulk (MEF) and Main Tower on the Mothra vent field [*Wankel et al.,* 2011]. The coupling of flow data with geochemical data also helped us visualize the potential magnitude of subsurface hydrogen oxidation, and provided a first preliminary glimpse of subsurface microbial metabolism. Section 3.6 concludes the chapter.

3.2 Geological Setting

JdF located roughly 300 km seaward of British Columbia and Washington State in the northeast Pacific Ocean (**Figure 3.1**) is an intermediate-rate ridge, spreading at a full rate of ~60 mm/yr [*Delaney et al.,* 1992] consisting of six segments: Cleft, Vance, Axial, CoAxial, Endeavour, and West Valley from south to north (**Figure 3.1**).

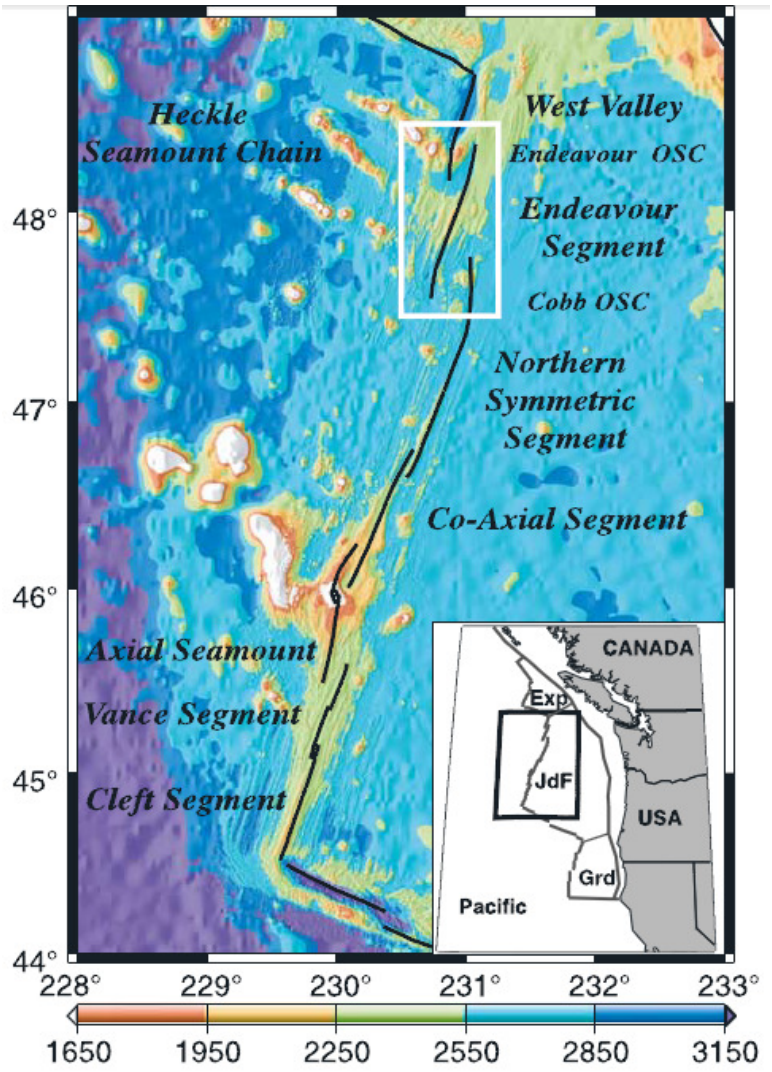

Figure 3.1 Bathymetric map of the JdF (in meters), showing the location of the Endeavour segment and the plate boundary (black line). The Endeavour segment is bounded to the north by the Endeavour overlapping spreading center (OSC) and to the south by the Cobb OSC [*Van Ark et al.,* 2007].

The Endeavour segment, which is the focus of this study, is cleaved by an axial rift valley 10 km long, 1 km wide and has an average depth of 100 m [*Delaney et al.,* 1992]. Hydrothermal venting is distributed among five major active vent fields spaced 2 to 3 km apart. From south to north these are: Mothra, Main Endeavour, High Rise, Salty

Dawg, and Sasquatch [*Delaney et al.,* 1992; *Kelley et al.,* 2001] (**Figure 3.2**). We briefly describe the settings for MEF, High Rise and Mothra below.

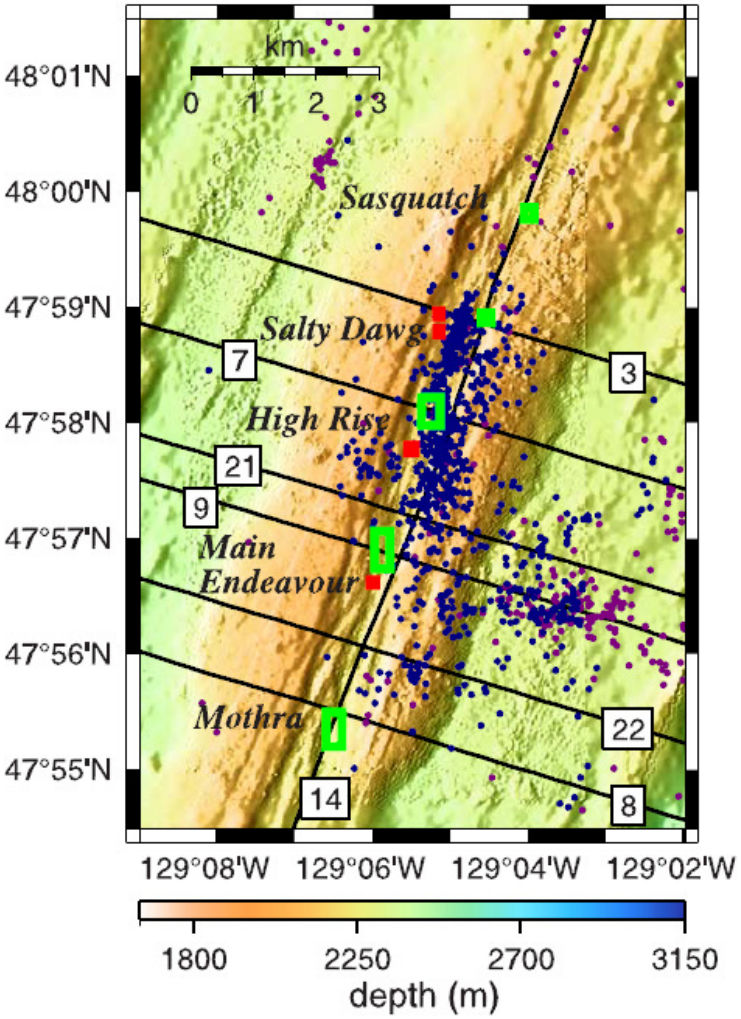

Figure 3.2 Bathymetric map showing the Endeavour segment axial high. Green boxes show the location of the five known active high-temperature hydrothermal vent fields and red boxes the location of diffuse, low-temperature vent fields: Cirque, Dune, Clambed, and Quebec, from north to south (vent locations from D. Glickson (personal communication, 2005)) [*Wilcock et al.,* 2002; *Van Ark et al.,* 2007].

Main Endeavour Vent Field at 47°57'N and 129°06'W [*Tivey and Delaney,* 1986], with an average depth of ~2,200 m [*Delaney et al.,* 1992] is situated near the boundary between the medial valley and western valley wall [*Schultz et al.,* 1992]. The active

hydrothermal vent structures lie along inward-facing normal faults that bound the valley and provide major pathways for hydrothermal fluids to reach the seafloor [*Kappel and Franklin,* 1989; *Delaney et al.,* 1992]. The vent field consists of a large number of sulfide edifices, with some reaching heights greater than 20 m and widths greater than 10 m, occupying an area ~180 m wide and ~350 m along the axis [*Tivey and Delaney,* 1986; *Delaney et al.,* 1992] (**Figure 3.3**). There are ~100 individual high-temperature chimneys with venting orifices typically 3-5 cm in cross-sectional diameter [*Delaney et al.,* 1992] on the various structures, discharging fluid with an average temperature of ~350° C [*Veirs,* 2003]. Diffuse flow fluids with temperatures less than ~50° C emerge from the top and side surfaces of active sulfide structures and are often associated with large tube worm patches [*Delaney et al.,* 1992].

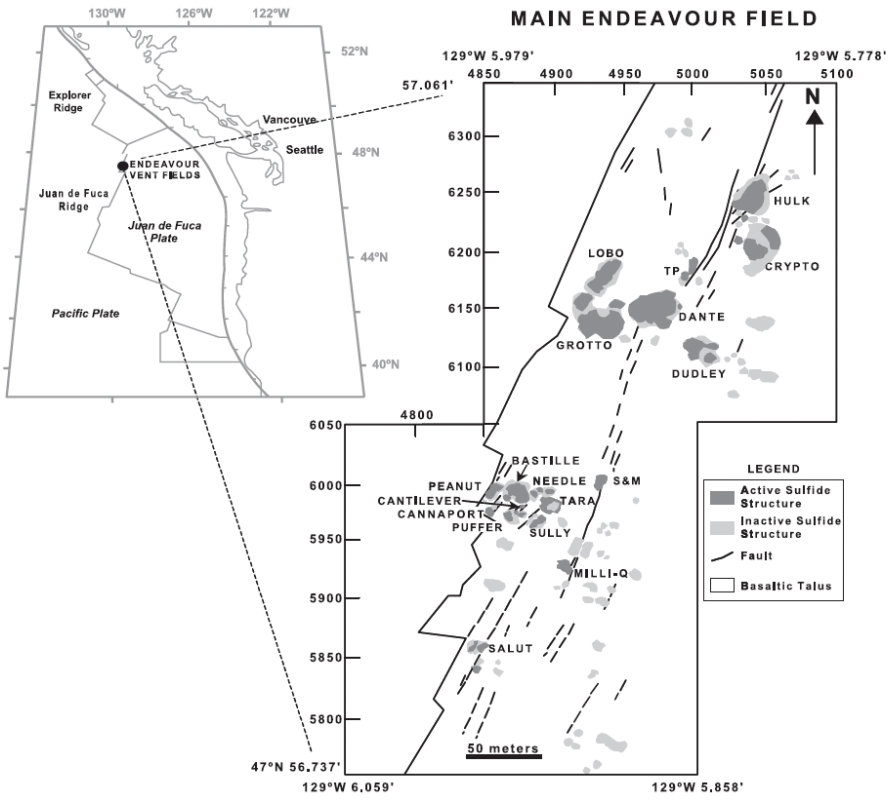

Figure 3.3 Geologic map of the Main Endeavour vent field, Northern JdF. The figure was modified after *Delaney et al.* [1992, 1997], and *Butterfield et al.* [1994] by *Foustoukos et al.* [2004].

High Rise Vent Field lies to the north of MEF on a central horst, youngest tectonic feature 150 m wide and at least 500 m long within the axial valley at an average depth between ~2,150 and 2,200 m [*Robigou et al.,* 1993]. Active venting occurs through ten large structures with volumes ~10^3-10^4 m^3 on top of the horst (**Figure 3.4**). In contrast to the MEF, High Rise structures are characterized by complex flared-top vent structures, with an average height of 10 to 15 m, exhibiting abundant horizontal flanges typically tens of cm thick and a few meters long protruding from the side of the main vertical structure (**Figure 3.5**). Pools of high-temperature fluid often form beneath the flanges. Several venting chimneys of 2 to 3 m high occur on the summit of the structures,

discharging high-temperature hydrothermal fluid through orifices 3 to 10 cm in diameter [*Robigou et al.,* 1993].

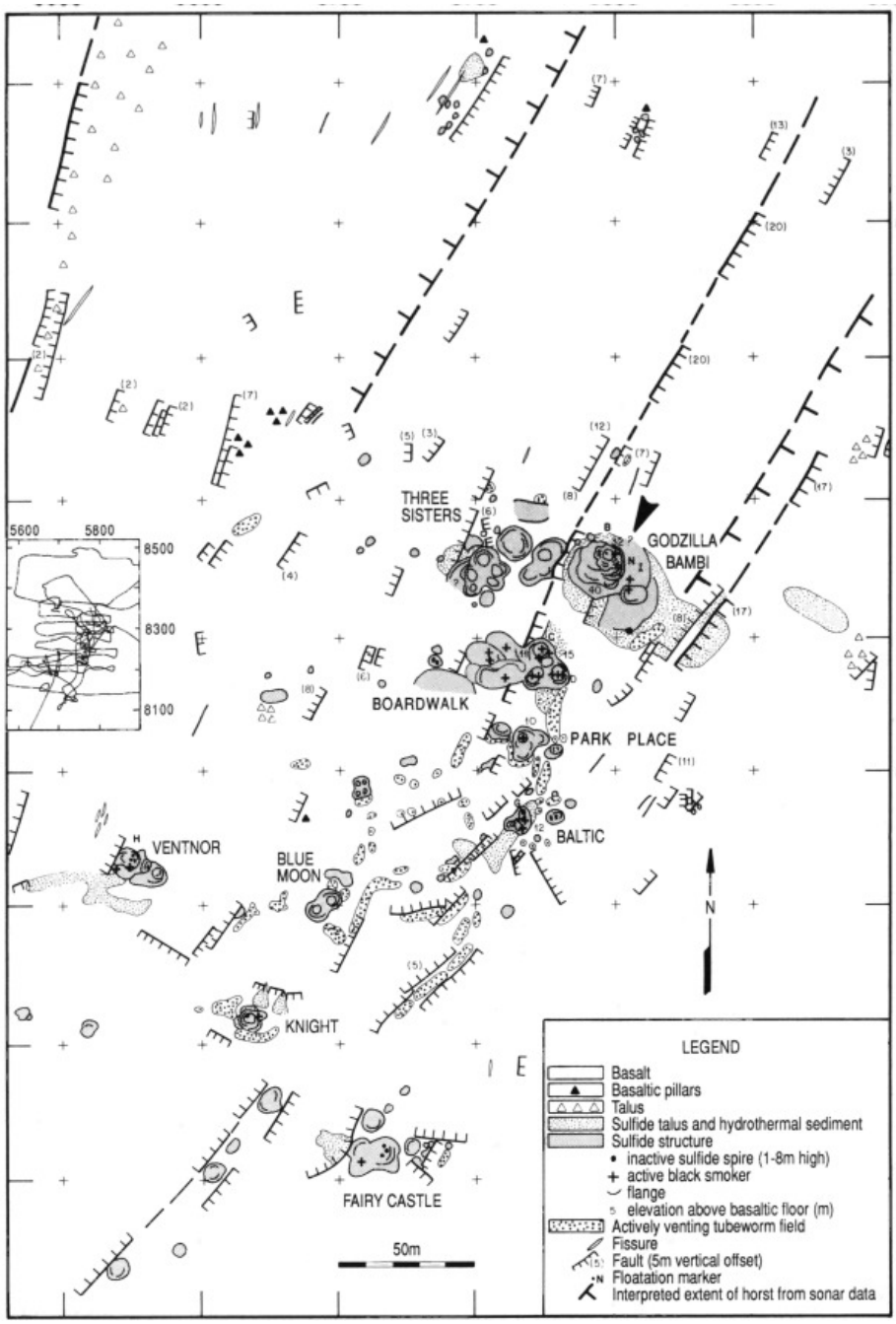

Figure 3.4 Detailed geological map of the High Rise hydrothermal vent field based on 9 dives in 1991 [*Robigou et al.,* 1993].

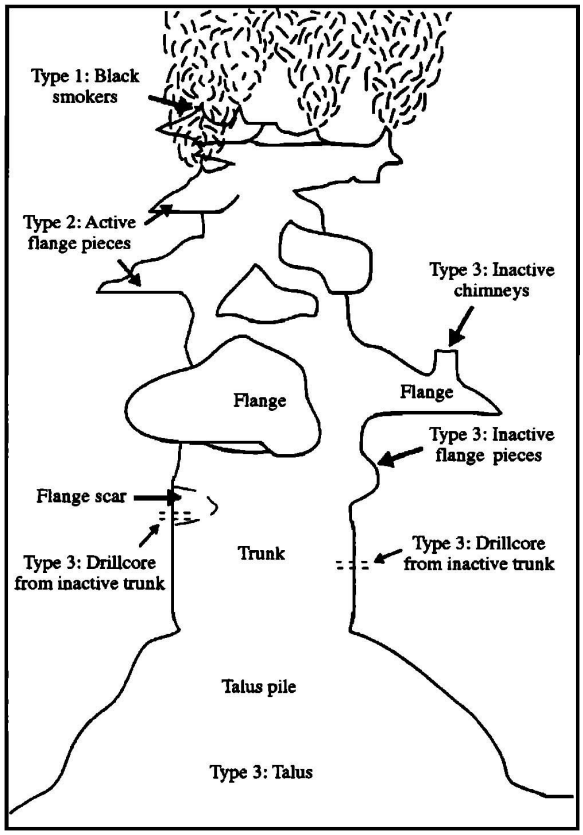

Figure 3.5 A cartoon showing a typical Endeavour sulfide edifice. The sulfide edifices are generally up to ~20 m high in the MEF and ~45 m high in the High Rise vent field and consist of a basal talus pile, a nearly vertical trunk, numerous tiers of flanges, and a "summit" with both active and inactive chimneys [after *Robigou et al.,* 1993, from *Tivey et al.,* 1999].

The most southern and largest in areal extent of the known five hydrothermal vent fields along the Endeavour segment, the Mothra hydrothermal vent field is located near 47°55.2'N, 129°06.3'N, at a water depth of 2270 m and 2.7 km south of the Main Endeavour vent field [*Glickson et al.,* 2007]. It incorporates six major active sulfide clusters (Cauldron, Twin Peaks, Faulty Towers, Crab Basin, Cuchulain, Stonehenge from north to south) located 40 to 200 m apart from each other (**Figure 3.6**). Mothra uniquely hosts sulfide clusters which consist of steep-sided pinnacles of up to ~20 m above the floor [*Kelley et al.,* 2001] and significantly less black smoker numbers compared to the

Main Endeavour and High Rise vent fields which are in contrary associated with large sulfide structures usually with overlapping, stepped flanges and various black smokers [e.g., *Tivey and Delaney,* 1986; *Delaney et al.,* 1992; *Robigou et al.,* 1993]. The venting system in Mothra is governed by up to 25 m-long sulfide pinnacles with less number of black smokers venting vigorous flow (≥ 300° C) on the outer surfaces which are covered by shimmering mixture of ambient seawater and hydrothermal fluid of low- to moderate-temperature (≤ 200° C) [*Kelley et al.,* 2001].

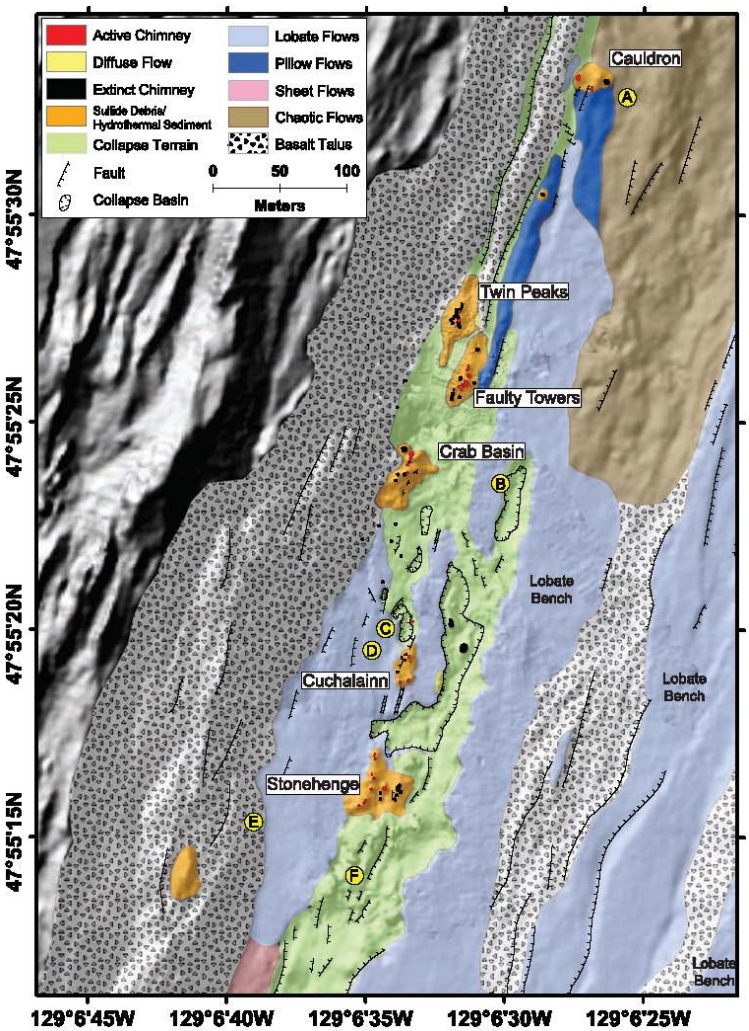

Figure 3.6 Geological map of the Mothra vent field that shows six active sulfide clusters based on visual imagery from 14 *Alvin* and remotely operated vehicle (ROV) dives, coregistered sonar and multibeam bathymetry [*Glickson et al.,* 2007].

3.3 Collection and Analysis of Heat Flow Data

3.3.1 Fluid flow devices

To determine heat output directly from discrete sources, we used two devices, the cup anemometer and turbine flow meter. The cup anemometer (**Figure 3.7**) used on the cruises in July and August, 2008 consists of an array of cups mounted such that the cups rotate about a horizontal axis. The device is placed over the vent using *Alvin*'s mechanical arm; the flow rate is then determined by analyzing the rate of rotation from the video record and using a calibration curve to obtain the linear velocity. The turbine flow meters (**Figure 3.8**) were used on the cruises in 2009 and 2010. They both consist of a vertically oriented cylindrical tube with rotor blades oriented at an angle of 45° to 65° to the symmetry axis. The operation and analysis is similar to that of the cup anemometer. The design details, additional figures and engineering drawings of the anemometer and turbine flow meters, and calibration curves are given in Chapter 2.

(a) **(b)**

Figure 3.7 Front view of the cup anemometer with no cone attachment **(a)** in the lab and **(b)** at a diffuse flow site, at Dante during the July 2008 cruise (*Alvin* dive 4422). The device size is 14.7 x 14.2 x 7.8 cm and it is attached to the handle. Notice the cups are colored in white and green for monitoring purposes and for data analysis from video imagery.

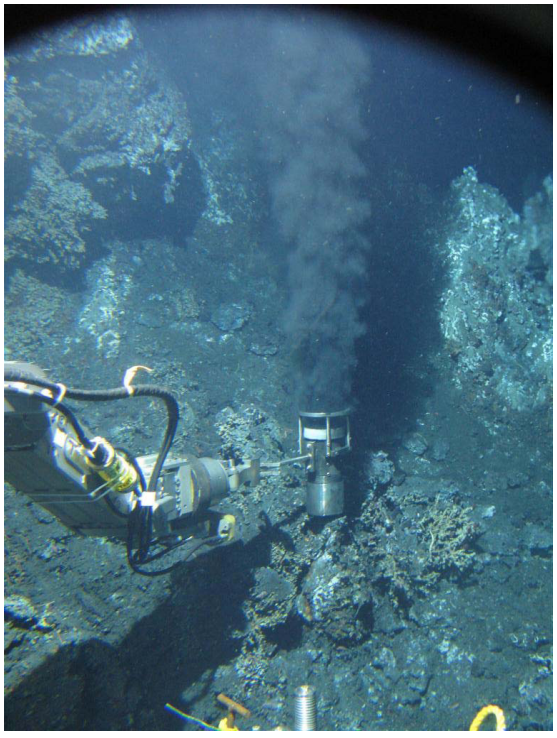

(a) **(b)**

Figure 3.8 (a) Front view of the turbine flow meter with attached handle in the lab. **(b)** Deployment of the turbine flow meter device from *Alvin* over a black smoker vent chimney at North Dante during the June 2009 cruise (*Alvin* dive 4518).

3.3.2 Measurements and Data Analysis

Measurements of fluid flow, when linked to geochemical data can be used to estimate geochemical fluxes. This is described more fully in Section 3.5.3. To determine hydrothermal heat output, we measured fluid temperature at the discharge site, ambient fluid temperatures, and the area of discharge, in addition to fluid flow velocity. Heat output *H* at a particular site is then calculated from the formula

$$H = C_f v \Delta T A \qquad (3.1)$$

where the volumetric heat capacity of the fluid, C_f = 4×10^6 J/(m^3 °C), *v* is the fluid velocity, Δ*T* is the difference between hydrothermal fluid temperature and ambient seawater temperature; and *A* is the area over which the heat flow measurement is performed.

At each discharge site, one of *Alvin*'s manipulator arms held the submersible's temperature probe along the centerline of the chimney orifice or diffuse flow site either just before or just after the fluid flow measurement was made. We measured the flow rate by placing the cup anemometer or turbine flow meter over each chimney or diffuse flow area and video recording the rotations of the paddle wheel or rotor about its axis (**Figures 3.7b** and **3.8b**). While recording the rotations on *Alvin's* video system, which was held as orthogonal to the flow meter by the other mechanical arm, we also observed the device for several minutes to insure that steady rotations were taking place.

Flow velocity of hydrothermal fluid was estimated from advancing the video images frame by frame with a precision of 0.07 s and then counting the number of full

revolutions of the paddle wheel or the turbine rotor during a time *t*. We marked the cups of the paddle wheel with numbers and colored them to help identify the rotations. As for the turbine flow meter, we drew a thick white perpendicular line across the upper support element of the turbine flow meter that is connected to the turbine rotor, to provide a visual observation mark which proves the rotation of the rotor itself. Once the rotation rate was determined, the linear velocity was obtained from the calibration curves (**Figures 2.9** and **2.10** in Chapter 2). Each flow velocity represents an average of at least five determinations of rotation rate made at nearly equally distributed time slots over a time interval of approximately between three to ten minutes.

We used 2-D tools to determine dimensions of an orifice (diameter, *d*) or a diffuse flow site (length, *l* and width, *w*). Our simple method involved obtaining estimates of target heat source sizes, using measuring tools of Adobe Acrobat Professional following the initial gathering of internal still photographs of relevant dives or best digital screen shots of frames from video imagery with *IrfanView*, a non-commercial graphic view software. We scaled the dimensions of the heat source with respect to those of a measuring device (e.g., our flow meter, *Alvin*'s temperature probe) available on the same relevant image. For simplicity we assumed the orifice to be circular. The area is then calculated as $\pi d^2/4$. For low-temperature flow *A* is the entire area of diffuse venting on a sulfide structure or the area of seafloor over which shimmering flow is observed. The area of diffuse discharge was typically observed to be rectangular in shape and calculated as *lw*.

3.4 Results

Table 3.1 summarizes the results from four different expeditions (AT15-34, 15-36, 15-47, 15-67) between 2008 and 2010. 33 dives in total [dive numbers: 4414, 4415, 4416, 4418, 4420, 4422, 4439, 4441, 4446, 4447, 4449, 4452, 4516, 4518, 4525, 4526, 4621, 4623, 4626, 4627, 4628] were executed in the Main Endeavour, Mothra and High Rise vent fields. There were a total of 25 dives at MEF: 11 dives at Dante, 8 dives at Hulk, 1 dive at S&M, 4 dives at Grotto, 1 dive at Crypto; 2 dives at Mothra both at Faulty Towers; 6 dives at High Rise: 1 dive at Godzilla (High Rise Vent Field), 1 dive at Park Place (High Rise Vent Field), 1 dive at Fairy Castle (High Rise Vent Field), 1 dive at Ventnor (High Rise Vent Field), 1 dive between Fairy Castle and Ventnor, and 1 dive at Boardwalk (High Rise Vent Field). We completed forty-six flow measurements, with co-registered temperature measurements at individual orifices. Of these, forty measurements were made at MEF, 3 at Mothra, and 3 at High Rise. **Table 3.1** also lists 12 additional flow measurements; 9 at MEF, and 3 in High Rise for which temperature data were not available or recorded. **Table 3.1** shows heat outputs for individual orifices ranging between 0.007 MW and 17 MW, with average values of 2 MW at MEF, 11 MW at Mothra, and 9 MW at High Rise. Heat output from diffuse flow sites were obtained only at MEF, where they ranged between 0.01 and 4 MW.

Table 3.1 Results of hydrothermal heat output estimates from the flow measurements between 2008 and 2010 in the Main Endeavour, Mothra and High Rise vent fields, along the Endeavour segment of JdF. Superscripts [a] and [f] denote "adjacent orifices"; [b] "identical smokers"; [c] and [d] "very close measurement locations"; and [e] for "faulty *Alvin* coordinates". Diffuse heat output estimates are shown in bold color and red-colored hydrothermal fluid temperature values represent either those measured during previous dives at these sites or average values determined for these sites.

Vent structure name	Cruise / Dive	*Alvin* coordinates X,Y (m)	Mean velocity (cm/s)	T (°C)	Flow area (cm^2)	Heat output (MW)
		Main Endeavour vent field				
Hulk	AT 15-34 / 4414	5045, 6254	54.62	322	12.56	0.88
		5041, 6230	76.47	313	29.80	2.85
		5035, 6236	25.92	312	8.87	0.29
	AT 15-34 / 4416	5034, 6251	11.77	304	4.99	0.071
		5034, 6253	21.76	136	169.5	2.01
		5036, 6256	10.66	256	14.30	0.16
		5040, 6245[a,b]	15.27	272	67.40	1.12
		5040, 6245[a,b]	22.45	279	120.18	3.01
		5045, 6253[b]	16.6	260	127.88	2.21
	AT 15-34 / 4420	5041, 6260	8.20	213	3.30	0.023
	AT 15-36 / 4447	5047, 6246	14.5	308	12.57	0.22
	AT 15-36 / 4449	5043, 6243	12.97	324	50.3	0.84
		5047, 6262	26.97	320	19.64	0.68
	AT 15-36 / 4452	5068, 6262	62.29	328	28.27	2.31
		5068, 6262	14.1	85	50.27	0.24
	AT 15-67 / 4626	5041, 6245	21.01	288	13.00	0.31
		5053, 6259	53.26	316	79.00	5.32
	Average		*27.58*			*1.33*
	AT 15-67 / 4627	5043, 6252[c]	3.30	50	2400.00	**1.58**
		5042, 6252[c]	9.69	50	200.00	**0.39**
	Average		*6.50*			***0.99***
Dante	AT 15-34 / 4415	4976, 6144	73.1	319	21.80	2.03
	AT 15-34 / 4422	4968, 6146	6.5	250	1.1	0.0068
		4969, 6160	24.1	328	25.1	0.79
		4972, 6163	66.8	333	48	4.27
		4977, 6154	22.1	210	20.8	0.39
		4965, 6135	21.2	300	4.2	0.11
		4987, 6172[d]	6.7	333	57.8	0.51
		4987, 6172[d]	9.2	333	29.80	0.37
		4987, 6172	7.9	142	94.2	0.42
		4988, 6170	9.5	312	27.4	0.32
		4984, 6175	22.4	236	253.9	5.38
	AT 15-36 / 4439	4973, 6162	49.9	328	12.6	0.82
	AT 15-36 / 4441	4954, 6165	51.80	328	28.3	1.92
		4977, 6157	73	325	38.5	3.65
	AT 15-36 / 4447	5096, 6054[e]	61.8	337	44.2	3.68
		4980, 6163	28.90	337	41.9	1.63
	AT 15-36 / 4452	4974, 6153	5.9	163	12.60	0.048
	AT 15-47 / 4518	4999, 6135	92.00	326	17	2.04
	AT 15-47 / 4525	4966, 6167	104.00	326	79.00	10.71
	AT 15-67 / 4626	4966, 6163	38.73	326	79.00	3.99
	Average		*38.78*			*2.15*
	AT 15-34 / 4420	4997, 6182	7.3	52	7.30	**0.011**
	AT 15-47 / 4518	5005, 6168	8.00	50	2400	**3.84**
	Average		*7.65*			***1.93***
Grotto	AT 15-36 / 4439	4923, 6145	54	324	3.1	0.22
		4935, 6146	53.2	330	132.7	9.32
	AT 15-67 / 4626	4945, 6160	57.57	320	79.00	5.82
	AT 15-67 / 4621	4933, 6154	17.79	327	9	0.21
	Average		*45.64*			*3.89*
	AT 15-67 / 4627	4945, 6160	5.59	50	300	**0.34**
	AT 15-67 / 4627	4954, 6153	11.12	55	600	**1.47**
	Average		*8.36*			***0.91***
S&M	AT 15-36 / 4446	4938, 6013	5.1	49	112.00	**0.11**
Crypto	AT 15-36 / 4452	5051, 6219	65.9	328	12.6	1.09
		Mothra vent field				
Faulty Towers	AT 15-34 / 4418	4152, 3319[f]	36	322	132.7	6.15
		4152, 3319[f]	36	322	254.5	11.80
	AT 15-67 / 4628	4156, 3297	33.3	322	314	13.48
	Average		*35*			*10.48*
		High Rise vent field				
Godzilla	AT 15-47 / 4516	5769, 8313	154	349	79	16.98
Park Place		5736, 8258	64	348	14	1.25
Between Fairy Castle & Ventnor		5604, 8196	121	348	4	0.67
Fairy Castle	AT 15-47 / 4526	5710, 8137	80	348	44	4.9
Ventnor		5620, 8201	113	332	79	11.86
Boardwalk	AT 15-67 / 4623	5786, 8290	24.1	364	20	0.7
	Average		*92.68*			*8.61*

3.5 Discussion

3.5.1 Main Endeavour Field

The hydrothermal vents at MEF have been intensely studied for more than 20 years. It is particularly interesting in the context of the present study because there have been numerous estimates of heat output from MEF over the course of these studies and a variety of techniques have been used [*Baker and Massoth,* 1987; *Rosenberg et al.,* 1988; *Thompson et al.,* 1992; *Schultz et al.,* 1992; *Bemis et al.,* 1993; *Ginster et al.,* 1994; *Stahr et al.*, 2000; *Thompson et al.*, 2005; *Veirs et al.*, 2006]. Heat output estimates of *Baker and Massoth* [1987], *Rosenberg et al.* [1988], and *Thompson et al.* [1992] are all made on the segment scale and hence include the heat output from all five major hydrothermal fields on the Endeavour segment. These estimates are typically in the range of more than 10^3 MW. For MEF, *Baker* [2007] calculates an average heat output of 423 $\pm$ 212 MW based on integrated measurements and 302 $\pm$ 88 MW based on point measurements of high-temperature vents by *Bemis et al.* [1993] and *Ginster et al.* [1994]. From *Ginster et al.*'s [1994] point measurements, hydrothermal heat output appears to be concentrated on the larger structures such as Hulk, Dante, Grotto and Crypto in the northern part of the MEF than from the smaller, though slightly higher structures such as Peanut and Bastille in the southern part of the field (see **Table 3.2**). *Thompson et al.* [2005] suggest that heat output from MEF has declined by a factor of 2 between the ABE surveys in 2000 and 2004.

Table 3.2 High-temperature heat output estimates from the vent structures in MEF and total focused heat output for MEF

High-temperature venting				
Vent sites	**Minimum measured site heat output (MW) [*This study*]**	**Extrapolated vent field heat output (MW) [*This study*]**	**Estimated site heat output (MW) [*Ginster et al.,* 1994]**	**Estimated site heat output (MW) [*Bemis et al.,* 1993]**
Dante	**43**		87	29 - 88
Hulk	**23**		59	7 - 26
Grotto	**16**		34	8 - 28
Crypto	**1**		59	-
Lobo			11	2 - 7
Dudley			13	-
TP			39	7 - 41
Bastille			23	2 - 10
Peanut			11	-
S&M *Cathedral*				
***Total high-temperature heat output* (MW)**	**83**	**119**	**364**	**63 - 219**

The MEF continues to be an area of active plume study. Acoustic methods, which eliminates most of the optical limitations such as rapid attenuation of light in water or patchy behavior of the distribution of diffuse flow zones which makes them hard to map, have been used and are in constant development to image, visualize and quantify hydrothermal flow both from diffuse flow sources and discrete vents. Such methods vary from imaging buoyant plumes from black smokers using backscatter of an acoustic pulse from small suspended particles [*Palmer and Rona,* 2005] or turbulent temperature fluctuations [*Ostashev,* 1994; *Ross,* 2003] or using a Doppler algorithm to measure flow velocity and mean vertical velocity [*Jackson et al.,* 2003]. *Rona et al.* [2010] describe a Vent Imaging Pacific (VIP) experiment in July 2000 which acoustically imaged and quantified hydrothermal diffuse and discrete flows at vent clusters in the Main Endeavour field and provided heat partitioning by using a sonar system (Simrad SM

2000) on ROV Jason. Three methods of analysis were: (a) visualization techniques of backscatter from suspended particulates and density discontinuities in plumes, (b) Doppler algorithm method to measure vertical plume velocity and to determine volume flux through different plume altitudes, and (c) Acoustic Scintillation Thermography (AST) [*Rona and Jones,* 2009] to detect and map irregular distribution of diffuse flow areas. Based on the preliminary results they obtained from a sulfide edifice in the Grotto vent cluster and additional information from AST and in-situ flow rate and temperature measurements, they suggested the diffuse heat flux to be significantly larger than plume heat flux (smokers ~50 MW/diffuse flow ~900 MW) [*Di Iorio et al.,* 2012].

To continuously monitor integrated vigorous hydrothermal plumes and investigate temporal variability in physical properties such as temperature or flow velocity, an alternate method; the acoustic scintillation method has been also applied in the Main endeavor field [*Xu,* 2010]. This method is based on the approach of recovering properties of the medium by measuring fluctuations of the acoustic signal passing through the plume [*Di Iorio et al.,* 2005]. By using this method *Xu and Di Iorio* [2011] estimated the heat transport of the plume — at 20 m above the orifice — from Dante to be ~62 MW by using a mean vertical velocity value of 0.14 m/s, temperature of the plume of 2.4° C, and ambient temperature of 1.7° C.

To this database we add nearly 42 measurements of heat output at high-temperature vents and 7 measurements of diffuse heat output within the MEF (**Table 3.1**). All of the high-temperature measurements and six of the diffuse flow

measurements were made at the large structures, Dante, Hulk, Grotto and Crypto in the northern part of the vent field; one diffuse flow measurement was also made at S&M in the southern part of the vent field.

3.5.1.1 High-temperature heat output

From **Table 3.2**, our total measured high-temperature heat output from Dante, Hulk, Grotto and Crypto is 83 MW, but this is a lower estimate for MEF because we have not measured heat output at all the active sulfide structures in this field [e.g., Lobo, Dudley, TP, Bastille]. We obtained a good distribution of heat flow estimates from high-temperature vent chimneys on Hulk, Dante (at about half of the vents predicted to actively vent on both of these structures), and Grotto, but we obtained a significantly more sparse distribution of heat flow measurements at Crypto which is known to host five black smokers. However we observed that the sum of heat flux estimates obtained by *Ginster et al.* [1994] and *Bemis et al.* [1993] in buoyant plumes from Dante, Hulk, Grotto and Crypto constitutes approximately 70% of the total estimated focused heat output from the whole vent field (MEF). Based on the assumption that this ratio of 70% still holds for MEF, we extrapolate our minimum estimate to the entire area of this field and determine the total high-temperature output to be 119 MW. This value is only 33% of the total estimated high-temperature output of *Ginster et al.* [1994] and 54% of the upper estimate predicted by *Bemis et al.* [1993]. These observations clearly indicate that the heat output from MEF has been decaying with time. This prediction is also consistent with that of *Thomson et al*. [2005].

3.5.1.2 Partitioning of Heat Output

We measured diffuse heat output at 7 separate locations in the Main Endeavour vent field. Two of these were performed at Dante, both on tubeworms covering the surface of a vent chimney: one was from Boss Sampler which was located within close proximity to Dante and the other was from a tiny chimney venting gray smoke with no co-registered temperature estimate. The third measurement was at S&M and the two diffuse flow measurements were recorded at Hulk and the last two at the Grotto vent structure. The hydrothermal fluid temperatures and velocities ranged between 49° and 55° C and 3 to 11 cm/s respectively. The area of the diffuse flow zone where we obtained measurements were all assumed to be visually associated with patches of sulfide edifices or areas of seafloor (between 7 and 2400 cm^2) mostly around sulfide structures where diffuse shimmering was significantly observed from *Alvin*. To determine a lower and upper limit for total diffuse and combined (discrete and diffuse) heat outputs and flux ratios, we assumed two distinct diffuse flow conditions; one condition under which diffuse venting occurs over 1% of the entire area of MEF, and the other over 10% of the total area of MEF (**Table 3.3**). We used an average diffuse heat flux value of 14.25 MW/m^2. As reported on **Table 3.3** we estimated a range of 460 to 4598 MW for the total diffuse heat output from MEF, by using an estimated area ranging from 32.27- 322.7 m^2 for the total area of active diffuse venting in this field [*Schultz et al.,* 1992]. The total combined hydrothermal heat output is predicted to amount to at least 579 MW and as high as 4717 MW. High-temperature venting is only associated at most with 21% of this estimate and could even be as low as 3%. For a

better understanding of heat partitioning, diffuse flow needs to be measured more frequently, densely and accurately and a few previous estimates of diffuse heat flow need to be revisited and compared by future work [*Schultz et al.,* 1992; *Ginster et al.,* 1994] as this study does.

Table 3.3 Total diffuse heat output and total combined (diffuse and discrete) heat output estimates for MEF

Low-temperature venting						
Diffuse flow sites & assumed diffuse flow conditions	**Diffuse heat output from Table 3.1 (MW)**	**Diffuse heat flux (MW/m^2)**	**Diffuse flow area (m^2)**	**Total diffuse heat output (MW)**	**Total combined heat output (MW)**	**Heat flux ratio (focused / diffuse)**
Hulk	0.99	13				
Grotto	0.91	18				
Dante	1.93	16.00				
S&M	0.11	10.00				
Average	**0.99**	**14.25**				
1% of total area of MEF			32.27	460	579	0.26
10% of total area of MEF			322.7	4598	4717	0.026

3.5.2 Heat output from High Rise and Mothra

The data presented in **Table 3.1**, though sparse, represent the only point estimates of heat output for these vent fields. All previous estimates have come from segment scale studies [*Baker,* 2007] and from the ABE survey of *Thompson et al.* [2005], who estimate the heat output from High Rise, MEF, and Mothra to be 500 MW, 300 MW, and 100 MW, respectively.

Our point measurement data from High Rise is too limited to provide an accurate estimate of the total high-temperature heat output, though we have measured heat output as high as 17 MW and fluid flow rates as high as 1.5 m/s there. This is higher than

from any black smoker at MEF or Mothra. Based on the geological map prepared by *Robigou et al.* [1993] from 9 dives during 1991, High Rise hosts ~26 active black smokers in total at Boardwalk, Godzilla, Baltic, Ventnor, Knight, Park Place and Fairy Castle vent structures. If we further extrapolate our average estimated heat output from the vent orifices in High Rise where we made measurements to the whole vent field, we predict the total high-temperature heat output from this field to be 448 MW assuming each black smoker possessed at least 2 venting chimneys. This assumption is not unrealistic considering most of the large sulfide-sulfate-silica structures in High Rise are associated with several active chimneys. The reported data and the approximate estimate that we determined for the total heat output from this field are shown to be consistent with that estimated by *Thompson et al.* [2005].

The few data points from Mothra are from the most vigorous black smoker cluster (Faulty Towers) there. The average orifice heat flux (11 MW) is higher than the fluxes at the most vigorous black smoker orifices at MEF; however the venting activity there is significantly different than in MEF. Each cluster in Mothra has chimney walls which are often awash in diffusively venting fluids of 30° to 220° C, but black smoker chimneys venting vigorous smoke of > 300° C are rare [*Kelley et al.,* 2001; *Glickson et al.,* 2007], in contrast to MEF which hosts more than 100 active chimneys venting hydrothermal fluids up to 380° C [*Delaney et al.,* 1992; *Lilley et al.,* 2003]. In total there are 34 active smoker chimneys at Mothra and the majority of these chimneys (14 out of 34) are located on Faulty Towers. It would not be realistic to provide an estimate for the total focused heat output from Mothra due to two main reasons:

(a) We don't have any information concerning how many of these 14 above-stated chimneys are located on three black smokers [*Kelley et al.,* 2001] which were potentially associated with the most vigorous flow.

(b) Our estimate for the average orifice heat flux may not necessarily indicate a representative value for the heat flux from any vent smoker in Mothra and it is probably an overestimate since it is associated with the chimneys on the Main Tower vent discharging the most robust focused flow in this field.

3.5.3 Initial Estimates of Geochemical Fluxes and the Implications

Hydrothermal vents play an important role in global cycles of sulfur, carbon, nitrogen, and many metals, by hosting productive communities [*Fischer et al.*, 2007]. Despite lacking or limited knowledge on heat and geochemical flux characterization from low-temperature diffuse flow areas and the key function of diffuse fluids in geochemical fluxes to the ocean [*Von Damm and Lilley,* 2004; *Butterfield et al.,* 2004; *Johnson et al.,* 1986; *Le Bris et al.,* 2006; *Proskurowski et al.,* 2008; *Walker et al.,* 2008], the geochemical role of diffuse flows to the global ocean has been estimated to exceed that of focused high-temperature flows [*Elderfield and Schultz,* 1996; *Schultz et al.,* 1992]. In order to improve our poor understanding of vent biogeochemistry and the effects of low-temperature diffuse fluids in biogeochemical cycles through subsurface activity, we collaborated with biogeochemists to couple our direct flow measurement results from our flow meter with those from *in situ* geochemical analyses. *Wankel et al.* [2011] reports and discusses the results of this collaborative study and provides the initial estimates of geochemical flux in the Main Endeavour and Mothra hydrothermal

vent fields from both high-T focused and low-T diffuse fluids, the latter rich in metals, volatiles and known to reside longer in the subsurface biosphere and hence naturally favor biogeochemical transformations.

During the *Alvin* cruise AT15-34 in July 2008 measurements of fluid volatile concentration of CH_4, $CO_{2(aq)}$, H_2 were successively made with our measurements of heat flow velocity on three dives at discrete heat flow sources (focused flow vent chimneys or diffuse flow milieus) on various vent structures (Dante, Hulk, Faulty Towers) in the Main Endeavour and Mothra hydrothermal vent fields at JdF (see Table 1 on *Wankel et al.* [2011]). The hydrothermal fluid temperatures from these sources were also concurrently measured by direct sampling from DSV *Alvin*. Flow rates were measured by using our positive displacement cup anemometer the design details and development stages of which can be located in Chapter 2 along with the drawings and figures. Further details on the method of in-situ measurement and post-dive data analysis from collected digital imagery to estimate the rotation rate and heat source area for each individual orifice or diffuse flow patch are also discussed in Chapter 2. Direct concentration measurements were made using an *in situ mass spectrometer* (ISMS) deployed from the submersible DSV *Alvin*. The ISMS was developed based on the basic principles of a membrane inlet mass spectrometry (MIMS) commonly used for an extensive selection of dissolved gases encountered both in industry and laboratory through the last decade [*Johnson et al.,* 2000; *Ketola et al.,* 2002] but improved and modified to adapt to sub-sea hydrothermal environments [*Wankel et al.,* 2011]. More explanation on the characteristics of communications to the instrument, its response, its

configuration during the deployments and its integration with the submersible is presented in detail in *Wankel et al.* [2010]. Estimated flow rates vary from 7.3 cm/s at Dante to 35.5 cm/s at Main Tower based on visual observations from video analysis with co-registered hydrothermal fluid temperatures ranging from 156° to 321° C. And volumetric flow rates extend along a range from as low as 3.5 m^3/day at a small focused flow source on Hulk ("Hulk Slurp2") up to 767 m^3/day and higher at a large focused flow source on Faulty Towers ("Main Tower") (See Table 2 on *Wankel et al.* [2011]).

Concentrations of H_2, CH_4, and $CO_{2(aq)}$ are measured to range respectively between 0.3-103 µM, 8-1153 µM, and 86-8029 µM, from various sampling environments either low-temperature diffuse fluids or high-temperature focused fluids. Overall the concentrations of H_2, CH_4, and $CO_{2(aq)}$ are observed to decrease at North JdF after 1999 eruption [*Lilley et al*., 2003; *Seyfried et al*., 2003].

Geochemical fluxes are subsequently determined by coupling the estimates from direct concentration measurements with ISMS with those from heat flow measurements with our flow meter and using the estimates of heat source area. The values of mass transport of H_2, CH_4, and $CO_{2(aq)}$ from the individual orifices range between 0.02-19.2 kmol yr^{-1}, 0.2-252 kmol yr^{-1}, and 2-1510 kmol yr^{-1} respectively, giving flux values of ~900, 11000 and 64300 kmol m^{-2} yr^{-1} for large focused flow sites and ~40, 600, and 8800 kmol m^{-2} yr^{-1} for those which are relatively smaller. The most vigorous fluxes are observed to be associated with larger chimney orifices. At relatively smaller sulfide structures, average fluxes are calculated to be ~5 to 14% of those from larger orifices which are usually associated with higher direct volatile concentration values. The

geochemical flux from a diffuse flow area on an active sulfide edifice called “Finn” in the Mothra hydrothermal vent field is also determined by estimating the areal extent of diffuse flow based on the visual distribution of microbial mat, macrafaunal growth, or simply shimmering water from video imagery and by coupling geochemical data with an assumed average linear diffuse flow velocity of 5 cm s^{-1}. The average area normalized fluxes of 5, 92, and 940 kmol m^{-2} yr^{-1} for H_2, CH_4, and $CO_{2(aq)}$ respectively are predicted to be significantly low when compared to those from focused, high-temperature sources (see Table 3 on *Wankel et al.* [2011]). However by taking into the consideration the total areal coverage of diffuse flow on Finn, the diffuse mass transport of H_2, CH_4, and $CO_{2(aq)}$ are calculated as 21, 380, and 3600 kmol yr^{-1} at this structure at the top of which focused mass transport values are estimated to be 30, 380, 2200 kmol yr^{-1}. The measurement results show that geochemical flux of certain volatile concentrations (e.g., $CO_{2(aq)}$, H_2) from low-temperature diffuse flow areas may be identical to or even greater than that from high-temperature focused flow areas.

Through reported in-situ data it is shown that geochemical flux associated with diffuse flows constitutes at least half of the net geochemical flux which may be affected by subsurface microbial activity and it is therefore emphasized that diffuse flow from hydrothermal settings play a significant role in geochemical flux to the ocean. Yet the role of diffuse flows in geochemical flux should be better constrained at hydrothermal vents exhibiting diverse topography and hydrology, at both slow- and fast-spreading centers, and even in serpentinization-dominated systems.

3.6 Conclusions

This chapter reports on an extensive database of 58 separate direct heat flow and heat flux measurement results from discrete and diffuse point sources in the Main Endeavour, Mothra and High Rise vent fields on the Endeavour segment of JdF along with some results from in-situ geochemical flux measurements in the Main Endeavor and Mothra vent fields. To the best of our knowledge, the reported values of heat output from Mothra and High Rise are the first results determined through direct measurements along this segment as well as the preliminary in-situ estimates for the geochemical flux from hydrothermal flows. We predicted the total high-temperature heat output to be 119 MW based on a simple extrapolation and which suggests that the heat loss from MEF has been decreasing with time as *Thomson et al*. [2005] has predicted. The heat output for High Rise in comparison was much greater at 448 MW. Based on two distinct diffuse flow conditions, we also estimated the total combined hydrothermal heat output (diffuse and focused) in MEF to be at least 579 MW and as high as 4717 MW which provides a heat partitioning fraction of only 3 to 21% for high-temperature venting. Finally we validated that geochemical flux from diffuse flows is associated at least with half of the net geochemical flux. Therefore the crucial role of diffuse flow in geochemical flux to the ocean and hence geochemical cycles needs to be thoroughly investigated at both spreading centers and serpentinization-dominated systems. The heat flow data can furthermore constrain models of hydrothermal flow and the effects of seismic and volcanic events on hydrothermal systems. Heat

partitioning between discrete and diffuse components of flow seems to have a major significance for understanding basic physics of hydrothermal systems.

3.7 References

Baker, E.T. (2007), Hydrothermal cooling of Mid-Ocean Ridge axes: Do measured and modeled heat fluxes agree?, *Earth and Planetary Science Letters, 263*(1-2), 140-150.

Baker, E.T., and G.J. Massoth (1987), Characteristics of hydrothermal plumes from two vent fields on the Juan de Fuca Ridge, Northeast Pacific Ocean, *Earth and Planetary Science Letters, 85,* 59-73.

Baker, E.T., G.J. Massoth, S.L. Walker, and R.W. Embley (1993), A method for quantitatively estimating diffuse and discrete hydrothermal discharge, *Earth and Planetary Science Letters, 118*(1-4), 235-249.

Baker, E.T., and C.R. German (2004), On the global distribution of hydrothermal vent fields, *Mid-Ocean Ridges: Hydrothermal Interactions Between the Lithosphere and Oceans, 148,* 245-266.

Bemis, K.G., R.P. Von Herzen, and M.J. Mottl (1993), Geothermal heat flux from hydrothermal plumes on the Juan de Fuca Ridge, *Journal of Geophysical Research, 98,* 6351-6365.

Burd, B.J., R.E. Thomson, and G.S. Jamieson (1992), Composition of a deep scattering layer overlying a Mid-Ocean Ridge hydrothermal plume, *Marine Biology, 113*(3), 517-526.

Butterfield, D.A. R.E. McDuff, M.J. Mottl, M.D. Lilley, J.E. Lupton, and G.J. Massoth (1994), Gradients in the composition of hydrothermal fluids from the Endeavor Segment vent field: Phase separation and brine loss, *Journal of Geophysical Research, 99,* 9561-9583.

Butterfield, D.A., I.R. Jonasson, G.J. Massoth, R.A. Feely, K.K. Roe, R.E. Embley, J.F. Holden, R.E. McDuff, M.D. Lilley, and J.R. Delaney (1997), Seafloor eruptions and evolution of hydrothermal fluid chemistry, *Phil. Trans. R. Soc. Lond. A., 355,* 369-386.

Butterfield, D.A., K.K. Roe, M.D. Lilley, J.A. Huber, J.A. Baross, R.W. Embley, and G.J. Massoth (2004), Mixing, reaction and microbial activity in the subseafloor revealed by temporal and spatial variation in diffuse flow vents at Axial Volcano, *Geophysical Monograph, 144,* 269-289.

Converse, D.R., H.D. Holland, and J.M. Edmond (1984), Flow rates in the axial hot springs of the East Pacific Rise (21°N): Implications for the heat budget and the formation of massive sulfide deposits, *Earth and Planetary Science Letters, 69,* 159-175.

Corliss, J.B., J. Dymond, L.I. Gordon, J.M. Edmond, R.P. Von Herzen, R.D. Ballard, K. reen, D. Williams, A. Bainbridge, K. Crane, and T.H. Van Andel (1979), Submarine thermal springs on the Galapagos Rift, *Science, 203*(4385), 1073-1083.

Cowen, J.P., G.J. Massoth, and R.A. Feely (1990), Scavenging rates of dissolved manganese in a hydrothermal vent plume, *Deep Sea Research Part A: Oceanographic Research Papers, 37*(10), 1619-1637.

Delaney, J.R., V. Robigou, R.E. McDuff, and M.K. Tivey (1992), Geology of a vigorous hydrothermal system on the Endeavour Segment, Juan de Fuca Ridge, *Journal of Geophysical Research, 97*(B13), 19663-19682.

Delaney, J.R., D.S. Kelley, M.D. Lilley, D.A. Butterfield, R.E. McDuff, and J.A. Baross (1997), Temporal/spatial exploration of physical, chemical and biological linkages in a submarine hydrothermal laboratory: the Endeavour Ridge, *Eos Trans AGU, 78*(46): Abstract F756.

Di Iorio, D., D. Lemon, and R. Chave (2005), A self-Contained acoustic scintillation instrument for path-averaged measurements of flow and turbulence with application to hydrothermal vent and bottom boundary layer dynamics, *Journal of Atmospheric and Oceanic Technology, 22*(10), 1602-1617.

Di Iorio, D., J.W. Lavelle, P.A. Rona, K. Bemis, G. Xu, L.N. Germanovich, R.P. Lowell, and G. Genc (2012), Measurements and models of heat flux and plumes from hydrothermal discharges near the deep sea floor, *Oceanography, 25*(1), 169-179.

Edmond, J.M., J.B. Corliss, and L.I. Gordon (1979), Ridge crest-hydrothermal metamorphism at the Galapagos spreading center and reverse weathering, In Deep Drilling Results in the Atlantic Ocean: Ocean Crust, (eds. M. Talwani et al.) *Amer. Geophys. Union, Ewing Series, 2,* 383-390.

Elderfield, H., and A. Schultz (1996), Mid-Ocean Ridge hydrothermal fluxes and the chemical composition of the ocean, *Annual Review of Earth and Planetary Science, 24,* 191-224.

Fisher Jr., C.R., K. Takai, and N. Le Bris (2007), *Hydrothermal vent ecosystems, Oceanography, 20(1),* 14-23.

Foustoukos, D., R. James, M. Berndt, and W. Seyfried (2004), Lithium isotopic systematics of hydrothermal vent fluids at the Main Endeavour Field, Northern Juan de Fuca Ridge, *Chemical Geology, 212*(1-2), 17-26.

Ginster, U., M.J. Mottl, and R.P. Von Herzen (1994), Heat flux from black smokers on the Endeavour and Cleft Segments, Juan de Fuca Ridge, *Journal of Geophysical Research, 99,* 4937-4950.

Glickson, D.A., D.S. Kelley, and J.R. Delaney (2007), Geology and hydrothermal evolution of the Mothra hydrothermal field, Endeavour Segment, Juan de Fuca Ridge, *Geochemistry Geophysics Geosystems, 8*(6), Q06010.

Grassle, J.F. (1985), Hydrothermal vent animals: distribution and biology, *Science, 229*(4715), 713.

Grassle, J.F. (1986), The ecology of deep-sea hydrothermal vent communities, *Advances in Marine Biology, 23,* 301-362.

Jackson, D.R., C.D. Jones, P.A. Rona, and K.G. Bemis (2003), A method for Doppler acoustic measurement of black smoker flow fields, *Geochemistry, Geophysics, Geosystems, 4*(11), 1095.

Jannasch, H.W. (1995), Microbial interaction with hydrothermal fluids, *Geophysical Monograph-American Geophysical Union, 91,* 273.

Johnson, K.S., C.L. Beehler, C.M. Sakamoto-Arnold, and J.J. Childress (1986), In situ measurements of chemical distributions in a deep-sea hydrothermal vent field, *Science, 213,* 1139-1141.

Johnson, R., R. Cooks, T. Allen, M. Cisper, and P. Hemberger (2000), Membrane introduction mass spectrometry: trends and applications, *Mass Spectrometry Reviews, 19*(1), 1-37.

Kappel, E.S., and J.M. Franklin (1989), Relationships between geologic development of ridge crests and sulfide deposits in the Northeast Pacific Ocean, *Economic Geology, 84*(3), 485.

Karl, D.M. (1995), Ecology of free-living, hydrothermal vent microbial communities, In *The Microbiology of Deep-Sea Hydrothermal Vents* (ed. D.M. Karl), 35-124, CRC Press, Boca Raton, FL.

Kelley, D.S., J.R. Delaney, and D.R. Yoerger (2001), Geology and venting characteristics of the Mothra hydrothermal field, Endeavour Segment, Juan de Fuca Ridge, *Geology, 29*(10), 959.

Ketola, R.A., T. Kotiaho, M.E. Cisper, and T.M. Allen (2002), Environmental applications of membrane introduction mass spectrometry, *Journal of Mass Spectrometry, 37*, 457-476.

Le Bris, N., B. Govenar, C. Le Gall, and C.R. Fisher Jr. (2006), Variability of physic-chemical conditions in 9°50'N EPR diffuse flow vent habitats, *Marine Chemistry, 98,* 167-182.

Lilley, M.D., D.A. Butterfield, J.E. Lupton, and E.J. Olson (2003), Magmatic events can produce rapid changes in hydrothermal vent chemistry, *Nature, 422,* 878-881.

Lister, C. (1983), On the intermittency and crystallization mechanisms of sub seafloor magma chambers, *Geophysical Journal of the Royal Astronomical Society, 73*(2), 351-365.

Liu, L., and R.P. Lowell (2009), Models of hydrothermal heat output from a convecting, crystallizing, replenished magma chamber beneath an oceanic spreading center, *J. Geophys. Res., 114,* B02102, doi:10.1029/2008JB005846.

Lowell, R.P. (2010), Hydrothermal circulation at slow spreading ridges: Analysis of heat sources and heat transfer processes, In *Diversity of Hydrothermal Systems on Slow Spreading Ocean Ridges, Geophys. Monogr. Ser., 188* (eds. P.A. Rona, C. Devey, J. Dyment, and B. Murton), 11-26, AGU, Washington, D.C., doi:10.1029/2008GM000758.

Lowell, R.P., B.W. Crowell, K.C. Lewis, and L. Liu (2008), Modeling multiphase, multicomponent processes at oceanic spreading centers, Magma to Microbe: Modeling Hydrothermal Processes at Ocean Spreading Centers, 15-44.

Lowell, R.P., and L.N. Germanovich (1994), On the temporal evolution of high-temperature hydrothermal systems at ocean ridge crests, *J. Geophys. Res., 99,* 565-575.

Lowell, R.P., and L.N. Germanovich (2004), Hydrothermal processes at mid-ocean ridges: Results from scale analysis and single-pass models, G*eophysical Monograph,* 148, 219-244.

Lowell, R.P., and D.K. Burnell (1991), Mathematical modeling of conductive heat transfer from a freezing, convecting magma chamber to a single-pass hydrothermal system: implications for seafloor black smokers, *Earth and Planetary Science Letters, 104*(1), 59-69.

Lowell, R.P., and P.A. Rona (1985), Hydrothermal models for the generation of massive sulfide ore deposits, *Journal of Geophysical Research, 90*(B10), 8769-8783.

Lutz, R.A., L.W. Fritz, and R.M. Cerrato (1988), A comparison of bivalve (Calyptogena magnifica) growth at two deep-sea hydrothermal vents in the eastern Pacific, *Deep Sea Research Part A: Oceanographic Research Papers, 35*(10-11), 1793-1810.

Macdonald, K.C., K. Becker, F.N. Spiess, and R.D. Ballard (1980), Hydrothermal heat flux of the “black smoker” vents on the East Pacific Rise, *Earth and Planetary Science Letters, 48,* 1-7.

Morton, J.L., and N.H. Sleep (1985), A Mid-Ocean Ridge thermal model: Constraints on the volume of axial hydrothermal heat flux, *Journal of Geophysical Research, 90*(B13), 11345-11353.

Ostashev, V. (1994), Sound propagation and scattering in media with random inhomogeneities of sound speed, density and medium velocity, *Waves in Random Media, 4*(4), 403-428.

Proskurowski, G., M.D. Lilley, and E.J. Olson (2008), Stable isotopic evidence in support of active microbial methane cycling in low-temperature diffuse flow vents at 9°50'N East Pacific Rise, *Geochimica et Cosmochimica Acta, 72,* 2005-2023.

Pruis, M.J., and H.P. Johnson (2004), Tidal modulation of hydrothermal effluent temperature, *Journal of Geophysical Research*, submitted.

Ramondenc, P., L.N. Germanovich, K.L. Von Damm, and R.P. Lowell (2006), The first measurements of hydrothermal heat output at 9°50'N, East Pacific Rise, *Earth and Planetary Science Letters, 263,* 140-150.

Robigou, V., J.R. Delaney, and D.S. Stakes (1993), Large massive sulfide deposits in a newly discovered active hydrothermal system, the High Rise field, Endeavour Segment, Juan De Fuca Ridge, *Geophysical Research Letters, 20*(17), 1887-1890.

Rona, P.A., and D.A. Trivett (1992), Discrete and diffuse heat transfer at ASHES vent field, Axial Volcano, Juan de Fuca Ridge, *Earth and Planetary Science Letters, 109,* 57-71.

Rona, P., N. Brunswick, and C. Jones (2009), Acoustic scintillation thermography, *Measurement Techniques, Platforms & Sensors: A Derivative of the Encyclopedia of Ocean Sciences,* 376.

Rona, P.A., K.G. Bemis, C.D. Jones, D.R. Jackson, K. Mitsuzawa, and D.R. Palmer (2010), Partitioning between plume and diffuse flow at the Grotto Vent cluster, Main Endeavour Vent Field, Juan de Fuca Ridge: Past and present, *Eos Trans AGU,* 91(52): Fall Meeting Abstract OA21C-1519.

Rosenberg, N.D., J.E. Lupton, D. Kadko, R. Collier, M.D. Lilley, and H. Pak (1988), Estimation of heat and chemical fluxes from a seafloor hydrothermal vent field using radon measurements, *Nature, 334,* 604-607.

Ross, T. and R. Lueck (2003), Sound scattering from oceanic turbulence, *Geophys. Res. Lett., 30,* 1344-1347.

Roth, S.E., and J. Dymond (1989), Transport and settling of organic material in a deep-sea hydrothermal plume: evidence from particle flux measurements, *Deep Sea Research Part A: Oceanographic Research Papers, 36*(8), 1237-1254.

Sarrazin, J., P. Rodier, M.K. Tivey, H. Singh, A. Schultz, and P.M. Sarradin (2009), A dual sensor device to estimate fluid flow velocity at diffuse hydrothermal vents, *Deep Sea Research Part I: Oceanographic Research Papers, 56*(11), 2065-2074.

Schultz, A., J.R. Delaney, and R.E. McDuff (1992), On the partitioning of heat flux between diffuse and point source seafloor venting, *Journal of Geophysical Research, 97*(B9), 12299-12314.

Schultz, A., P. Dickson, and H. Elderfield (1996), Temporal variations in diffuse hydrothermal flow at TAG, *Geophysical Research Letters, 23*(23), 3471-3474.

Sclater, J.G., C. Jaupert, and D. Galson (1980), The heat flow through oceanic and continental crust and the heat loss of the Earth, *Reviews in Geophysics, 18,* 269-311.

Seyfried Jr., W., J. Seewald, M. Berndt, K. Ding, and D. Foustoukos (2003), Chemistry of hydrothermal vent fluids from the Main Endeavour Field, Northern Juan de Fuca Ridge: Geochemical controls in the aftermath of June 1999 seismic events, *J. Geophys. Res, 108*(B9), 1-23.

Stahr, F., R. McDuff, D. Yoerger, A. Bradley, and K. Nakamura (2000), Heat flux measurements at the Main Endeavour vent field, Juan de Fuca Ridge, *Eos Trans AGU, Fall Meet Suppl, 81,* 48.

Stein, C., S. Stein, and A. Pelayo (1995), Heat flow and hydrothermal circulation, *Geophysical Monograph-American Geophysical Union, 91,* 425-445.

Stein, C.A., and S. Stein (1994), Constraints on hydrothermal heat flux through the oceanic lithosphere from global heat flow, *J. Geophys. Res, 99*(B2), 3081-3095.

Thompson, G. (1983), Hydrothermal fluxes in the ocean, *Chemical Oceanography, 8,* 271-337.

Thomson, R.E., J.R. Delaney, R.E. McDuff, D.R. Janecky, and J.S. McClain (1992), Physical characteristics of the Endeavour ridge hydrothermal plume during July 1998, *Earth and Planetary Science Letters, 111,* 141-154.

Thomson, R.E., M.M. Subbotina, and M.V. Anisimov (2005), Numerical simulation of hydrothermal vent-induced circulation at Endeavour Ridge, *Journal of Geophysical Research, 110*(C1), C01004.

Tivey, M.K., D.S. Stakes, T.L. Cook, M.D. Hannington, and S. Petersen (1999), A model for growth of steep-sided vent structures on the Endeavour segment of the Juan de Fuca Ridge: Results of a petrologic and geochemical study, *Journal of Geophysical Research, 104*(B10), 22859-22883.

Tivey, M.K., and J.R. Delaney (1986), Growth of large sulfide structures on the Endeavour Segment of the Juan de Fuca Ridge, *Earth and Planetary Science Letters, 77*(3-4), 303-317.

Tunnicliffe, V. (1991), The biology of hydrothermal vents: ecology and evolution, *Oceanogr. Mar. Biol. Ann. Rev., 29,* 319-407.

Van Ark, E.M. (2007), Seismic and gravitational studies of melting in the mantle's thermal boundary layers, Ph.D. thesis, MIT-WHOI Jt. Program, Cambridge, Mass.

Veirs, S.R. (2003), Heat flux and hydrography at a submarine volcano: Observations and models of the Main Endeavour vent field in the northeast Pacific, Ph.D. thesis, University of Washington.

Veirs, S.R., R.E. McDuff, and F.R. Stahr (2006), Magnitude and variance of near-bottom horizontal heat flux at the Main Endeavour hydrothermal vent field, *Geochemistry Geophysics Geosystems, 7,* 1-16.

Von Damm, K.L., and M.D. Lilley (2004), Diffuse flow hydrothermal fluids from 9°50'N East Pacific Rise: Origin, evolution and biogeochemical controls, *Geophysical Monograph, 144,* 245-268.

Walker, B.D., M.D. McCarthy, A.T. Fisher, and T.P. Guilderson (2008), Dissolved inorganic carbon isotopic composition of low-temperature axial and ridge-flank hydrothermal fluids of the Juan de Fuca Ridge, *Marine Chemistry 108,* 123-136.

Wankel, S.D., S.B. Joye, V.A. Samarkin, S.R. Shah, G. Friederich, J. Melas-Kyriazi and P.R. Girguis, New constrants on methane fluxes and rates of anaerobic methane oxidation in a Gulf of Mexico brine pool via in situ mass spectrometry, *Deep Sea Res. II., 57,* 2022-2029.

Wankel, S.D., L.N. Germanovich, D.L. Marvin, G. Genc, C.J. DiPerna, A.S. Bradley, E.J. Olson, and P.R. Girguis (2011), Influence of subsurface biosphere on geochemical fluxes from diffuse hydrothermal fluids, *Nature Geoscience, 4,* 461-468.

Wilcock, W.S.D., and A. McNabb (1996), Estimates of crustal permeability on the Endeavour Segment of the Juan de Fuca Mid-Ocean Ridge, *Earth and Planetary Science Letters, 138*(1-4), 83-91.

Wilcock, W.S.D., S.D. Archer, and G.M. Purdy (2002), Microearthquakes on the Endeavour Segment of the Juan de Fuca Ridge, *J. Geophys. Res., 107*(B12), 2336, doi:10.1029/2001JB000505.

Williams, D.L., and R.P. Von Herzen (1974), Heat loss from the earth: new estimate, *Geology, 2*(7), 327.

Wolery, T.J., and N.H. Sleep (1976), Hydrothermal circulation and geochemical flux at Mid-Ocean Ridges, *The Journal of Geology, 84,* 249-275.

Xu, G. (2010), The Investigation of Hydrothermal Plumes by the Acoustic Scintillation Method, Ph.D. thesis, University of Georgia.

Xu, G., and D. Di Iorio (2011), The relative effects of particles and turbulence on acoustic scattering from deep-sea hydrothermal vent plumes, *The Journal of the Acoustical Society of America, 130,* 1856.

CHAPTER 4

DEFORMATION AND SURFACE UPLIFT ASSOCIATED WITH SERPENTINIZATION AT MID-OCEAN RIDGES AND SUBDUCTION ZONES

Abstract. We employ the classical problem of an inclusion in an elastic half-space to model two- and three-dimensional effects of sub-surface serpentinization on crustal deformation, change of stress state, and surface uplift. We calculated the transformation strain associated with spherically, cylindrically and elliptically shaped inclusions in an elastic half space to determine the resulting crustal deformation, stress change, and surface uplift. We showed that if the normalized depth, $h/(2a)$ of the inclusion was greater than ≈0.75, the resulting surface uplift was relatively insensitive to the shape and orientation of inclusions with the same volume. At the TAG hydrothermal field on the Mid-Atlantic Ridge, the model suggests that an anomalous salient 3 km in diameter and 100 m high that projects 3.5 km westward from the east valley wall may have resulted from a relatively deep-seated serpentinized body exhibiting between 20 and 40 % transformational strain. Such large strains would likely result in sub-surface fracturing or faulting, but surface uplift may be relatively insensitive to these effects as well as to the exact depth and shape of the serpentinized region. Serpentinization of a region beneath the footwall of the TAG detachment fault will tend to promote slip along some overlying normal faults, which may then result in fluid pathways to the deeper crust to continue the serpentinization process. Our solution for the Miyazaki Plain above

the Kyushu-Palau subduction zone in SW Japan explains the observed uplift of ≈120 m, but elastic transformational strain needs only be 3%. The small transformational strains associated with serpentinization in this region may promote thrust-type events in the aseismic slip zone near the upper boundary of the subducting Philippine Sea Plate. The rate of serpentinization needed to produce the observed uplift at the Miyazaki Plain ($\sim 8\times10^3$ kg/s) is significantly greater than that needed at TAG (~10 kg/s), though significantly smaller on per unit volume basis. Thermal effects of serpentinization in both regions are small.

4.1 Introduction

Serpentinization is a term describing a number of exothermic olivine hydrolysis reactions that occur when seawater reacts with ultramafic rocks and the primary minerals olivine and pyroxene are replaced by serpentine [*Fyfe and Londsdale*, 1981; *Macdonald and Fyfe*, 1985; *Allen and Seyfried*, 2003]. All of these reactions, which typically occur between 100-500^{o} C [*Cannat et al.*, 1992; *Früh-Green et al.*, 1996; *Mével and Stamoudi*, 1996; *Agrinier et al.*, 1997], are exothermic releasing about 290 kJ/kg [*Fyfe and Londsdale*, 1981; *MacDonald and Fyfe*, 1985]. In addition to releasing heat, serpentinization generally results in volume expansion ranging between 25% and 53% [*Coleman*, 1971; *O'Hanley*, 1992].

Both geologic and geophysical data suggest that partially serpentinized peridotites and serpentinites are a significant part of the oceanic lithosphere especially that formed at slow-spreading ridges [e.g., *Rona et al.*, 1987; *Carlson and Miller*, 1997; *Escartin et al.*, 2001]. Serpentinization is observed in outcrops at ridge offsets,

preferentially at inside corner highs (ICHs) [*Dick*, 1989; *Tucholke and Lin*, 1994; *Cannat et al.*, 1995], along ridge segments accreting with low magma supply [*Cannat et al.*, 1997; *Escartin and Cannat*, 1999], in upper mantle portions of ophiolites [*Bonatti*, 1976; *Bonatti and Hamlyn*, 1981; *Nicolas*, 1989; *Cannat*, 1993], and in cores recovered from shallow mantle of ocean ridges by the Ocean Drilling Program [*Gillis et al.*, 1993; *Früh-Green et al.*, 1996; *Karson and Lawrence*, 1997].

Serpentinization is also important in other submarine settings such as rifted margins [e.g., *Reston*, 2009], the ocean-continent transition zone [e.g., *Skelton and Jakobsson*, 2007], and subduction zones [e.g., *Faccenda et al.*, 2008; *Tahara et al.*, 2008; *Hilairet and Reynard*, 2009]. The relationships between slow earthquakes and aseismic slip [*Hirauchi et al.*, 2010] and the serpentine mud volcanoes of the Mariana forearc, where fluids exsolved from the downgoing slab serpentinize the overlying mantle and ascend to the surface through faults, are of particular interest in this context [e.g., *Fryer and Mottl*, 1992; *Fryer*, 1996a, 1996b; *Mottl et al.*, 2003; *Wheat et al.*, 2008].

Mounting evidence indicates that serpentinization plays a role in structural deformation and uplift at mid-oceanic ridges where it is commonly associated with the formation of oceanic core complexes and detachment faults [e.g., *Francis,* 1981; *Zonenshain et al.*, 1989; Bougault et al., 1993; *Cann et al.*, 1997; *Tucholke et al.*, 1998; *Escartin and Hirth*, 1997; *Escartin et al*., 2001; *Blackman et al.*, 2002; *Mével*, 2003; *Boschi et al.*, 2006; *Ildefonse et al.*, 2007; *Macleod et al.*, 2009; *Miranda and Dilek*, 2010]. The connection between serpentinization and tectonics is complicated; however, some simple conceptual models exist. For example, *Dziak et al.* [2000], based on the

interpretation of seismic data, suggested that the uplift of the Blanco Ridge is caused by serpentinized peridotite diapirs. *Francis* [1981] proposed the concept of serpentinization fault; that is, a fault triggered, induced, or affected by stress changes in a crustal region undergoing serpentinization and corresponding volumetric expansion. One of his scenarios, shown in **Figure 4.1a**, although not quantified, is partially consistent with the uplift observed at inside corner highs (ICHs) at ridge-transform intersections, though some of the uplift may be dynamically driven [*Tulcholke and Lin*, 1994; *Tucholke et al.*, 1998].

Palmer [1996] was among the first to develop a model of uplift assuming a characteristic volume expansion of 46% [*Coleman*, 1971; *O'Hanley* 1992] of fully serpentinized peridotite and taking into account the changes in the density of oceanic crust. In his model, serpentinization occurs in a 1-D layer that expands causing the uplift. Although *Palmer's* [1996] conclusion that the tectonics of slow-spreading ridges and their topography might result from serpentinization, in his 1-D model surface topography simply mimics the subsurface geometry of the serpentinized layer (**Figure 4.1b**).

This model cannot be used to construct the 2-D features proposed by *Dziak et al.* [2000] or *Francis* [1981] (**Figure 4.1a**); or the more complex 3-D geomorphic features that might be attributed to subsurface serpentinization-driven deformations. For example, *Zonenshain et al*., [1989], investigating tectonics of the Mid-Atlantic ridge, suggested that the serpentinization leads not only to narrow serpentinized protrusions along fault planes, but also embraces relatively wide areas beneath the crust and

induces uplift of large crustal blocks above the serpentinized layer. They argue that rift mountains and abnormal rift valley slopes are surface expressions that result from the serpentinization of mantle peridotite.

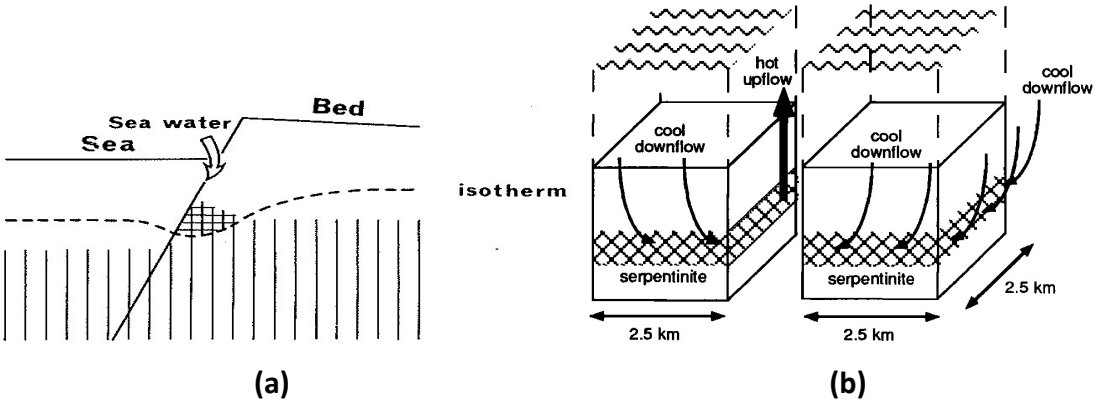

Figure 4.1 (a) Serpentinization at the footwall of a normal fault [*Francis*, 1981]. Rocks beneath the footwall of a normal fault hydrate as a result of seawater infiltrating down the fault, so that serpentinization occurs generating more movement on the fault and uplift [*Francis*, 1981]. **(b)** Cartoon of 1-D uplift resulting from serpentinization of oceanic crust [*Palmer*, 1996].

As a particular case, a component of deformation at the TAG hydrothermal field may have been produced by volumetric expansion caused by serpentinization superimposed on a complex detachment fault structure. The central portion of the walls of the axial valley of spreading segments on slow-spreading ocean ridges is generally straight. In contrast, the central portion of the east wall of the axial valley, where some of the hydrothermal zones in the TAG field occur, exhibits an anomalous bulge about 6 km long between 26°08.0'N and 26°11.0'N that includes a salient centered at 26°08.3'N that projects about 3.5 km westward over the valley floor [*Rona et al.*, 1993] as shown on **Figure 4.2**. The salient is bounded by the 3725 m (base) and 3625 m (top) isobaths and exhibits dome-shaped relief of about 100 m with a diameter of about

3000 m. *deMartin et al.* [2007] report two distinct clusters of microseismicity at depths of ~2-5 km below the seafloor with composite focal mechanisms consistent with normal faulting. One cluster conforms to the western edge of the bulge including the salient [*deMartin et al.*, 2007, Figure 1A]. The second cluster is aligned with the axial valley axis (23^{o}N) where the bulge intersects the east wall. The eastern wall including the bulge is underlain at depths below 1 km by a high-velocity anomaly (seismic velocity exceeding 6.5 km/s), which according to *deMartin et al.* [2007], is indicative of "the presence of lower crustal and/or lower serpentinized upper mantle rocks at anomalously shallow depths." They report that the velocity anomaly dips westward toward the spreading axis at an angle of about 20^{o} and passes under the active high-temperature TAG sulfide mound at a depth of ~1 km. They interpret these and related observations to support the existence of a major detachment fault in the east wall that projects up to ≈7 km downward [*deMartin et al.*, 2007]. The detachment fault may be a conduit for the flow of water into the upper mantle where serpentinization occurs. Boron levels in high-temperature hydrothermal fluids sampled from the TAG active sulfide mound (**Figure 4.2**) are lower than in seawater indicating ongoing uptake of boron by underlying serpentinization reactions [*Palmer*, 1996]. The salient and larger bulge may be a surface expression of deformation produced by a volume of serpentinized mantle located in the footwall beneath the hanging wall of the detachment fault [*Zonenshain et al*., 1989; *Rona*, 2008]. In this paper, we develop a model showing that at least the anomalous salient in the east wall, if not the entire bulge, may be produced by expansion of an underlying volume of serpentinized mantle.

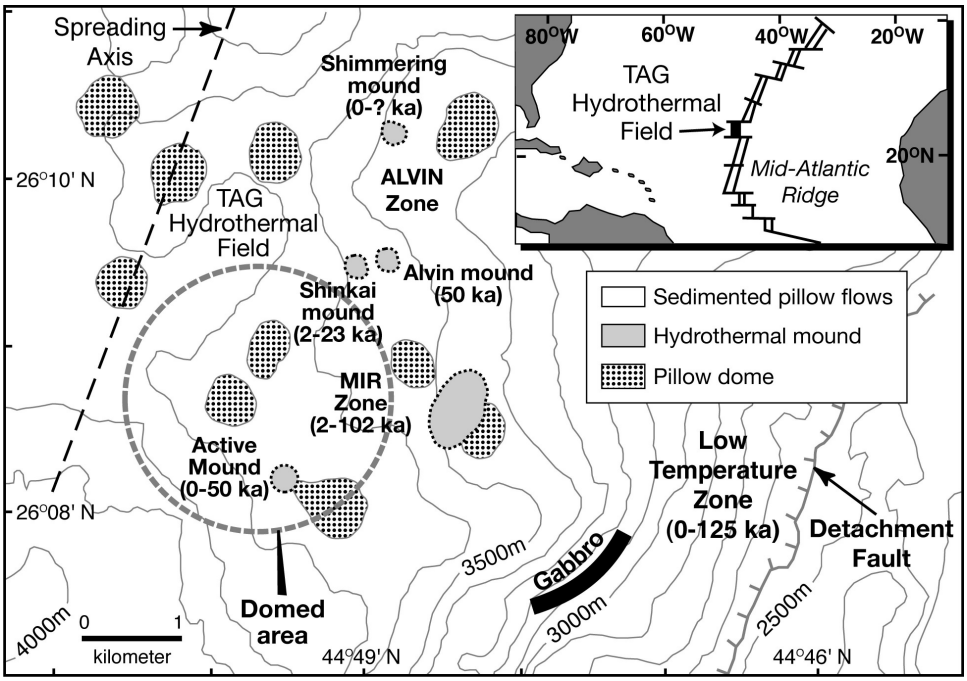

Figure 4.2 Bathymetric map of TAG hydrothermal field on the east wall of the axial valley of the Mid-Atlantic Ridge showing anomalous dome-shaped salient (encircled) centered near 26°08.7′N, 44°49.6′W with 100 m relief between 3725 m (base) and 3625 m (top) isobaths [modified from *Rona*, 2008]; the TAG field is inferred to lie on the hanging wall of a major detachment fault that crops out several kilometers to the east (lower left corner; see also *deMartin et al.* [2007]).

Serpentinization of the mantle wedge near subduction zones [e.g., *Hyndman et al.*, 1997] can also result in deformation and uplift. For example, serpentinization of the mantle wedge near the subducted Kyushu-Palau Ridge may be related to the inferred regions of aseismic slip beneath the Kyushu region of Southwestern Japan [*Yagi and Kikuchi*, 2003] and to the crustal uplift of ~10^2 m of the overlying Miyazaki Plain during the past ~1.2×10^5 years [*Nagaoka et al.*, 1991; *Tahara et al.*, 2008]. From seismic tomography data, *Tahara et al.* [2008] and *Saiga et al.* [2010] infer the existence of a region of low seismic velocity and high Poisson's ratio (**Figures 4.3a** and **4.3b**) that may be associated with serpentinization near the subducted Kyushu-Palau Ridge. *Saiga et al.*

[2010] depict this region as a quasi-elliptical inclined domain at a depth of 20 - 40 km beneath the Miyazaki Plain (**Figure 4.3b**). In addition, they show another sub-horizontal, quasi-elliptical region of low seismic velocity and near-normal Poisson's ratio (**Figure 4.3b**). Both *Tahara et al.* [2008] and *Saiga et al.* [2010] hypothesized that this sub-horizontal region denotes a zone of low-density buoyant material associated with subduction of the Kyushu-Palau Ridge, which may contribute to uplift of Kyushu Mountains. *Tahara et al.* [2008] proposed a similar mechanism for the Quaternary uplift of the Miyazaki Plain. In principal, buoyancy associated with a relatively low density of serpentinized material may certainly contribute to the crustal uplift, but we suggest that volume expansion resulting from incremental serpentinization of both of these regions could also result in the observed uplift of the Miyazaki Plain and Kyushu Mountains.

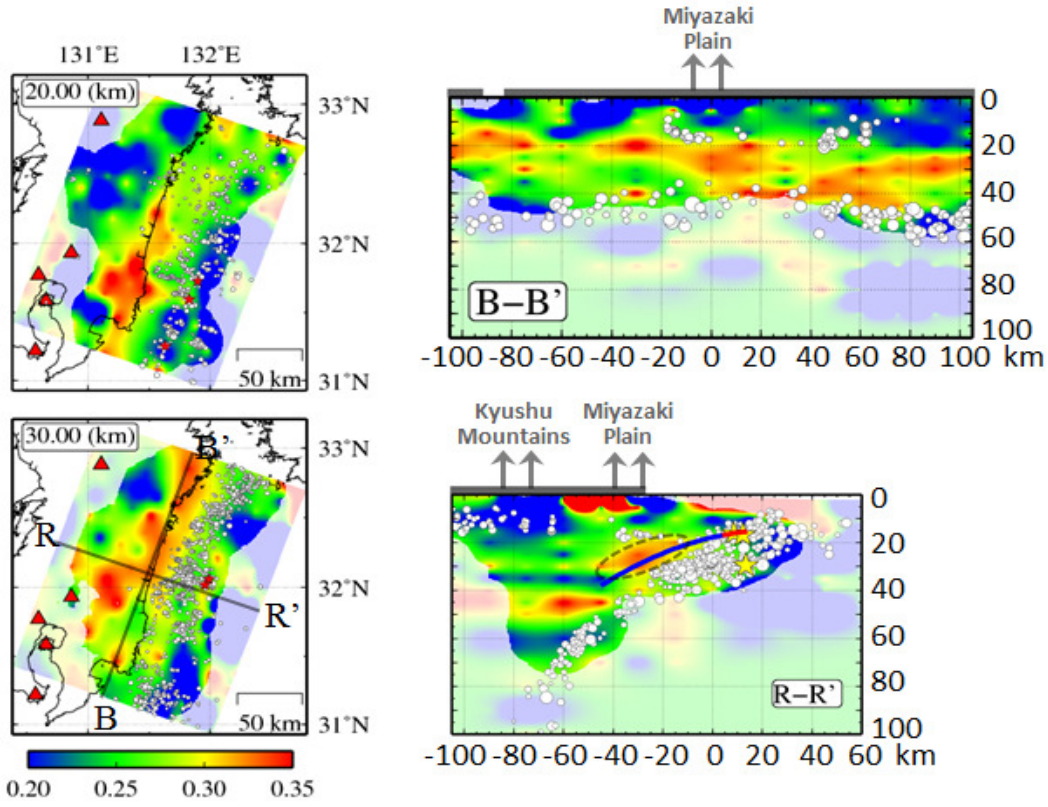

(a)

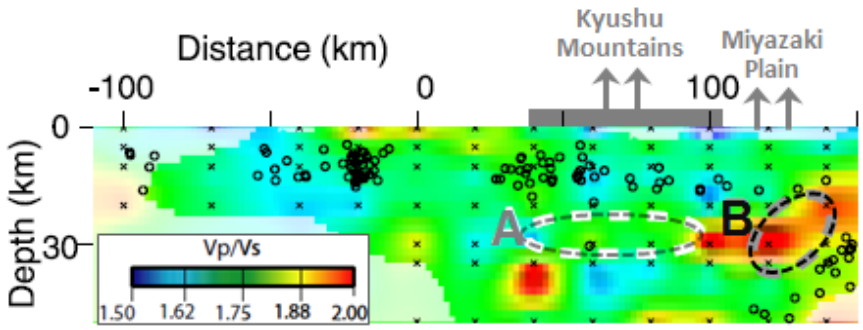

(b)

Figure 4.3 (a) Kyushu island (black coastline) and Poisson's ratio distribution at the depth of 20 km and 30 km (left), vertical cross-section underneath the line of B-B' along the coastline of the Kyushu island (upper right), and vertical cross-section along the line of R-R' in the direction of Philippine plate subduction (upper right) [modified after *Tahara et al*., 2008]. The land region is shown by gray, bold line in the figures on the right. Based on these and other cross-sections, regions with high Poisson's ratio (≥ 0.3 – yellow and red colors) were interpreted by *Tahara et al*. [2008] as quasi-elliptical, serpentinized domains similar to regions A and B in **Figure 4.3b.** Intersection of lines R-R' and B-B' is on the Miyazaki Plain. Red triangles show the active volcanoes. Circles indicate inter-plate earthquakes [see details in *Tahara et al.*, 2008]. Gray vertical arrows indicate the aseismic crustal uplift. **(b)** Vertical cross-section located approximately along the line of R-R' (**Figure 4.3a**) [modified after *Saiga et al*., 2010]. Colors represent ratio, of the ratio of P- and S-wave velocities, V_p/V_s, which is related to the Poisson's ratio [e.g., *Mavco et al*., 2003]. Gray rectangle above the vertical cross-section panel shows Kyushu Mountains. Ellipses represent regions with low velocity and high (gray dashed line A) or low (black dashed line B) ratio V_p/V_s [see details in *Saiga et al*., 2010]. White circles indicate earthquake locations in the Philippine Sea Plate that converges under the Eurasia Plate.

The 2-D and 3-D deformations described above that may result from serpentinization beneath the seafloor will also lead to large strains in the neighborhood of region undergoing serpentinization. Such large strains are likely to result in faulting or tensile fracturing that would be difficult to account for in the 1-D model developed by *Palmer* [1996]. Moreover, these processes are likely to be important for promoting the serpentinization process by creating new permeability and allowing fluid access to fresh peridotite. To explore these issues, we consider a first-order model of crustal

deformation and seafloor uplift resulting from volume expansion associated with the subsurface serpentinization. We employ a classic problem of an inclusion undergoing transformation strain in an elastic half-space. Using solutions of such problems for inclusions of different shapes, orientations and depths, we calculate the seafloor uplift. We discuss the topographic features at the TAG hydrothermal field (**Figure 4.2**) and uplift of the Miyazaki Plain and Kyushu Mountains as examples.

The importance of our analyses stems from treating the stress and strain effects resulting from serpentinization as an isolated process. We apply these results to the TAG hydrothermal field and the Miyazaki Plain in Southwestern Japan and discuss possible connections between serpentinization and fault slip. A detailed analysis of the connection between serpentinization, microseismicity, and faulting in a region of large serpentinization strain that may be associated with the observed topographic salient at TAG is beyond the scope of this paper. We show, however, that serpentinization beneath the footwall of the detachment fault at TAG may enhance fault slip on the overlying normal faults. For the smaller strains that explain the uplift of the Miyazaki Plain, we show that serpentinization will tend to promote trust-type events in some parts of the slip zone located near the upper boundary of the subducting Philippine Sea Plate underneath the Miyazaki Plain. Finally, we show that the rate of serpentinization needed to account for the uplift at TAG is likely too small to drive hydrothermal flow. The rate of serpentinization needed to produce the observed uplift at the Miyazaki Plain is significantly greater than that needed at TAG, though significantly smaller on per unit

volume basis. As a result, the effects of serpentinization on the thermal regime in forearc wedge beneath the Miyazaki Plain may be small.

4.2 Scaling of Seafloor Uplift

To incorporate two- or three-dimensional effects, we consider strain resulting from large-scale serpentinization based on the problem for an inclusion in the elastic half-space. The inclusion experiences homogeneous transformation strain (similar to homogeneous heating), ε_0, which is the homogeneous volumetric strain when the inclusion is allowed to expand freely. The physical nature of the transformation strain is attributed to the volumetric expansion resulting from the serpentinization reactions. Consider, for example, an inclusion of a given shape and volume V with a point, designated as the inclusion center, at the depth of h (**Figure 4.4a**). As a result of homogeneous serpentinization, the inclusion volume increases while its shape does not change. In a linearly elastic body, all displacements and stresses are proportional to the "loading" parameter, ε_0. In particular, the greatest vertical displacement on the seafloor, w_0, is also proportional to ε_0. Because the inclusion shape does not change, it can be characterized geometrically by its volume, V, in the 3-D case, and by its vertical cross-sectional area, S, in the 2-D case (e.g., when the inclusion is cylindrical, not necessarily circular, with its axis parallel to the half-space surface). Then, dimensional analysis suggests that w_0 is independent of the rock Young's modulus, E, and that in the 3-D case,

$$w_0 = \varepsilon_0 \frac{V}{h^2} f(\nu) \tag{4.1}$$

where $f(\nu)$ is the dimensionless function of the Poisson's ratio, ν. **Table 4.1** lists symbols used and parameter values. Because the displacement of the half-space surface is given by that of the same plane within a full space, increased by a factor of $4(1 - \nu)$ [*Mindlin and Chen*, 1950; *Davies*, 2003], $f(\nu)$ in equation (4.1) is proportional to $1 + \nu$, which also follows directly from the well known results for the case of arbitrary 3-D distribution of mismatch strain in an infinite medium [*Goodier*, 1937; *Timoshenko and Goodier*, 1970].

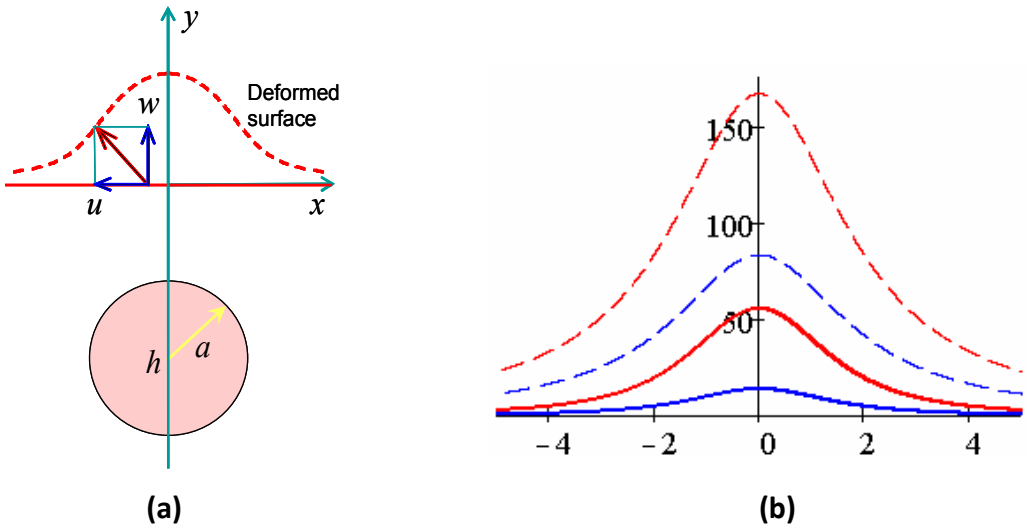

Figure 4.4 (a) A model of surface doming caused by subsurface serpentinization. Dashed line indicates the deformed surface over the center of the cylinder in the 2-D case and sphere in 3-D (with horizontal coordinate x replaced by the radial coordinate r). **(b)** Distribution of uplift, $-w$, for spherical (solid lines) and cylindrical (dashed lines) inclusions of the same radius a = 1 km located at the depth of 2 km (red lines) and 4 km (blue lines). The uplift is given in meters (vertical axes) and the lateral coordinates r or x (horizontal axes) in kilometers.

Table 4.1 List of symbols

SYMBOL	DEFINITION	VALUE
	Latin Symbols	
a	major semi-axis of an elliptical inclusion	
a	radius of a cylindrical or spherical inclusion	
a_1, a_2	major semi-axes of inclined and sub-horizontal inclusions, respectively (**Figure 4.9**)	20, 30 km
a_1, a_2, …	complex coefficients in equation (4.B5)	
A	mean stress in the inclusion in an infinite plane (equation (4.9))	
b	minor semi-axis of an elliptical inclusion	
b_1, b_2	minor semi-axes of inclined and sub-horizontal inclusions, respectively (**Figure 4.9**)	7.5, 5 km
B	Skempton coefficient	0 - 1
c_1, c_2, …	complex coefficients in equation (4.B3)	
d	thickness of serpentinized layer in *Palmer's* [1996] 1-D model	~1 km
$D(z)$	auxiliary function (equation (4.8))	
E	Young's modulus	10^{10} Pa
$f(\nu)$, $g(\nu)$	dimensionless functions of Poisson's ratio in equations (4.1), (4.2)	
h	depth of the inclusion center	
L	inclusion size in horizontal direction (perpendicular to the plain of drawing in **Figure 4.9**)	~100 km
$P(z)$	polynomial defined by asymptotic behavior of $D(z)$ at infinity	
r	radial coordinate	
R	$(a + b)/2$	
R_1	$[\xi^2 + (\eta + \eta_0)^2]^{1/2}$ (**Appendix 4A**)	
R_2	$[\xi^2 + (\eta - \eta_0)^2]^{1/2}$ (**Appendix 4A**)	
S	cross-sectional area of a 2-D inclusion	
t	time	
u	horizontal or radial displacement	
V	inclusion volume	
V_p/V_s	ratio of P- to S-wave velocities	
w	vertical displacement	
w_P	vertical displacement of the seafloor in *Palmer's* [1996] 1-D model	~100 m
w_0	largest vertical displacement of the seafloor	
x, y	Horizontal and vertical coordinates	
X, Y	rotated coordinate set with X-axis aligned along the long axis of the inclusion and parallel to the fault plane or slip zone	
$z = x + iy$	complex coordinate	

z_0	complex coordinate of the inclusion center (**Appendix 4B**)	
	Greek Symbols	
β	angle between the major axis of the inclusion and *x*-axis	
$\delta_1 = \varepsilon_0(1 + \nu)/3$	linear transformation strain in plain-strain conditions	
ΔI_1	change of the first stress invariant $\sigma_{xx} + \sigma_{yy} + \sigma_{zz}$	
$\Delta p = -B\Delta I_1/3$	pore pressure change due to the Skempton effect	
ΔT	Coulomb stress on the fault plane or slip zone	
$\Delta\varepsilon_0$	incremental transformation strain	
$\Delta\sigma_{YY}$	normal stress change on the fault or slip zone plane	
$\Delta\tau_{XY}$	shear stress change on the fault or slip zone plane	
$\Delta\tau_{XY}$, $\Delta\sigma_{YY}$	changes of the normalized shear, and normal stresses	
ε	small parameter $(a^2 - b^2)^{1/2}/h$	
ε_0	volumetric transformation strain	
$\zeta = \xi + i\eta$	complex coordinate on the infinite plane	
$\eta = y/a$	normalized vertical coordinate (**Appendix 4A**)	
$\eta_0 = h/a$	dimensionless depth of the inclusion (**Appendix 4A**)	
θ	fault angle in counter-clock direction with respect to the horizontal	
$\kappa = 3 - 4\nu$	plain-strain modulus	2
λ	complex coefficients (equation (4.B3))	
μ	shear modulus	
$\dot{M}$	mass rate of serpentinization	
ν	Poisson's ratio	0.25
$\xi = x/a$	normalized horizontal coordinate (**Appendix 4A**)	
$O(\varepsilon)$	a quantity of the order of ε	
$\rho = x/h, r/h$	dimensionless lateral or radial coordinate (Section 4.2)	
ρ_r	density of serpentine	≈2500 kg/m^3
σ_{xx}, σ_{yy}, σ_{zz}, τ_{xy}	stress components in (*x*, *y*) coordinate set	
τ_0	background (initial) tectonic shear stress on the fault or slip zone plane	
$\varphi(z)$, $\psi(z)$	*Muskhelishvili's* [1979] stress functions	
ϕ	serpentinized fraction of the inclusion volume	6% and 40%
$\omega(\zeta)$	conformal mapping of inclusion exterior onto the exterior of the unit circle in the infinite plane	
$\omega^{-1}(z)$	inverse function of $\omega(\zeta)$	

Similarly, dimensional analysis suggests that in the 2-D case,

$$w_0 = \varepsilon_0 \frac{S}{h} g(\nu) \tag{4.2}$$

where $g(\nu)$ is a dimensionless function of Poisson's ratio, ν, and, again, w_0 is independent of the rock Young's modulus, *E*. Note that hereafter, we use the same

parameter of *volumetric* transformation strain, ε_0, for both 2-D and 3-D cases. This strain characterizes *free* expansion of an unconstrained body and is usually measured in laboratory experiments. In this work, however, we assume plain strain conditions in the 2-D case, when "free" expansion is constrained in one direction and the volumetric strain is $(2/3)(1 + \nu)\varepsilon_0$. Since the results are often expressed through the plain-strain, 'free' linear expansion strain $\delta_1 = (1/3)(1 + \nu)\varepsilon_0$ [e.g., *Ru*, 1999; *Aderogba and Berry*, 1971], it is worth mentioning that in equation (4.2) and below, we use the same volumetric, transformation strain, ε_0, as in equation (4.1). In this formulation, 2-D and 3-D cases do not differ and, therefore, $g(\nu)$ in equation (4.2) is also proportional to $1 + \nu$. Using δ_1 instead of ε_0 in equations (4.1) and (4.2) would eliminate their dependence on ν, and, therefore, w_0 would be independent of material properties.

Now consider a spherical inclusion of radius a, with its center at depth h, in the half-space $y < 0$ as shown in **Figure 4.3a.** We use the cylindrical coordinate system (r, y), with horizontal coordinate r replacing the radial coordinate x, and the surface $y = 0$ represents the seafloor. Assuming that the inclusion lies entirely below the half-space surface ($h \geq a$), vertical and radial displacements of the seafloor, can be calculated as [*Mindlin and Chen*, 1950; *Nowacki*, 1986]

$$w = -\frac{w_0}{(1+\rho^2)^{3/2}}, \qquad u = \frac{w_0 \rho}{(1+\rho^2)^{3/2}} \tag{4.3}$$

respectively, where $w_0 = (1 + \nu)V\varepsilon_0/(3\pi h^2)$, $\rho = r/h$ is the normalized radial coordinate, and the inclusion volume $V = (4/3)\pi a^3$. In this case, therefore, $f(\nu) = (1 + \nu)/(3\pi)$. Note

that w in equation (4.3) is negative because of our choice, $y < 0$, of the coordinate set associated with the half-space.

Figure 4.3a shows schematically the surface deformation resulting from serpentinization of a spherical volume. Equation (4.3) suggests that, depending on parameters h (a few km) and V ($\sim 1 - 10$ km^3), maximum surface uplifts range between a few tens and a few hundreds of meters for $\varepsilon_0 \sim 0.1 - 0.5$. Such projected uplifts are similar to those estimated by *Palmer* [1996] using a 1-D model. In his model, the vertical displacement of the seafloor is uniform and, if the lateral strain is negligible, equals to $w_P = (1 + \nu)\varepsilon_0 d/[3(1 - \nu)]$, where d is the thickness of the serpentinized layer (**Figure 4.1b**). For $d \sim 1$ km and $\varepsilon_0 \approx 50\%$, $w_P \sim 100$ m. The horizontal extent of the uplifted area and uplift distribution cannot be estimated from *Palmer*'s [1996] model, however. As discussed below, these are naturally included in the 2- and 3-D models of serpentinized inclusion. In addition, w_P is independent of the depth of the serpentinized layer, whereas the uplift caused by a finite domain decreases with the depth according to equations (4.1) and (4.2).

In the model of spherical inclusion, w_0 depends upon both the inclusion radius and depth, but the shape of the uplift in equation (4.3) is independent of the radius. According to equation (4.1), the horizontal extent of the uplifted region (**Figure 4.4a**) scales with $\rho = 1$, where the vertical displacement becomes $2^{-3/2} w_0 \approx w_0 /2.8$. In other words, it scales with the inclusion depth, but is independent of its size (volume).

Let us now consider a cylindrical inclusion of radius a, with the center at a depth of h in a cylindrical coordinate system, with horizontal coordinate x replacing the radial

coordinate r in **Figure 4.3a**. In this case, the distribution of surface displacements is given by expressions

$$w = -\frac{w_0}{1+\rho^2}, \qquad u = \frac{w_0 \rho}{1+\rho^2} \tag{4.4}$$

similar to equations (4.3) and obtained by integrating the solution of *Mindlin and Chen* [1950] for a dilation center in a half-space (see also **Appendix 4A**). Here $w_0 = 2(1 + \nu)S\varepsilon_0/(3\pi h)$, $\rho = x/h$ is the dimensionless lateral coordinate, and the cross-sectional area of the inclusion $S = \pi a^2$. Hence, $g(\nu) = 2(1 + \nu)/(3\pi)$ in equation (4.2). As in the case of the spherical inclusion, the maximum of the surface uplift depends on both inclusion size and depth, whereas the shape of the surface uplift is independent of size but scales with the inclusion depth.

The largest vertical displacement on the seafloor for a spherical inclusion is $[(1+\nu)(2/9)(a/h)]^{-1}$ times smaller than for a cylindrical one of the same radius. To place this in context, we plotted the uplift distributions given by equations (4.3) and (4.4) in **Figure 4.4b**. As expected, serpentinization in an extended cylindrical region would result in larger surface displacement than that resulting from a more compact spherical region.

4.3 An Elliptical Inclusion

Although the simple scaling considered above provides some insight into understanding—multi-dimensional uplift process caused by the subsurface serpentinization, to address the effect of the inclusion shape, one needs solutions for displacements and stresses inside and outside of the inclusion of various shapes. In

order to perform a parametric analysis, it is preferable to have closed form solutions. For this purpose, we consider here a half-space containing an inclusion of elliptical shape. This solution is sufficiently general for a wide variety of settings, and it reduces to the simple cylindrical and spherical solutions above. We will then discuss applications of these solutions to the TAG region on the Mid-Atlantic Ridge (**Figure 4.2**) and the Kyushu region above the subducting Philippine Sea plate (**Figure 4.3**).

To perform the stress-strain analysis for an elliptical inclusion in a half-space, we employ the complex variable technique. The elastic field can be represented by the well-known expressions [*Muskhelishvili*, 1979]

$$\begin{cases} \sigma_{xx} + \sigma_{yy} = 2[\varphi(z) + \overline{\varphi(z)}], \quad \sigma_{yy} - \sigma_{xx} + 2i\tau_{xy} = 2\left[\bar{z}\varphi'(z) + \psi(z)\right] \\ 2\mu(u + iw) = \kappa\varphi(z) - z\overline{\varphi'(z)} - \overline{\psi(z)} \end{cases} \tag{4.5}$$

where σ_{xx}, σ_{yy}, and τ_{xy} are the stress components in (x, y) coordinate set (**Figure 4.5**), u and w, are the verticals and horizontal displacements in the half-space, $z = x + iy$, bars represents complex conjugates, $\kappa = 3 - 4\nu$ in plain strain conditions, $\mu = E/2(1 + \nu)$ is the shear modulus, ν is the Poisson's ratio, and $\varphi(z)$ and $\psi(z)$ are the *Muskhelishvili*'s [1979] stress functions. For an inclusion of arbitrary shape undergoing homogeneous transformation strain, ε_0, in an elastic half-space, these functions can be written as [*Ru*, 1999; *Ru et al.*, 2001]

$$\varphi(z) = A[\overline{D(\bar{z})} - \overline{P(\bar{z})} - z/2], \quad \psi(z) = -A[z\overline{D'(\bar{z})} - z\overline{P'(\bar{z})} - P(z)] \tag{4.6}$$

inside the inclusion, and

$$\varphi(z) = A[\overline{D(\bar{z})} - \overline{P(\bar{z})}], \quad \psi(z) = -A[z\overline{D'(\bar{z})} - z\overline{P'(\bar{z})} + D(z) - P(z)] \tag{4.7}$$

outside. Here

$$D(z) = \overline{\omega\,[1/\overline{\omega^{-1}(z)}]} \tag{4.8}$$

and

$$A = (4/3)\mu(1+\nu)\varepsilon_0 / (\kappa+1) \tag{4.9}$$

is equal to the mean homogeneous stress, $(\sigma_{xx} + \sigma_{yy})/2$, caused by the same transformation strain, ε_0, inside the same inclusion if it were located in the infinite plane. This can be shown by using the corresponding solution for the 2-D Eshelby inclusion [e.g., *Jaswon and Bhargava*, 1961] or directly from equations (4.5), (4.6), (4.7), and (4.11) (see below) as the inclusion depth $h \to \infty$.

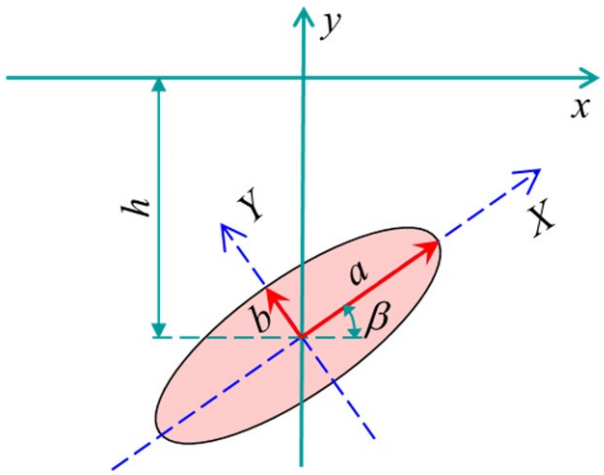

Figure 4.5 A model of elliptical domain of subsurface serpentinization. The domain is located in the half-space $y \le 0$, $-\infty < x < \infty$ and the major ellipse axis is aligned with coordinate axis, *X*, in rotated coordinate set *X*, *Y*.

In equations (4.6) – (4.8), $z = \omega(\zeta)$ is conformal mapping of the region outside the inclusion in the infinite complex plane $z = x + iy$ onto the exterior of the unit circle, $|\zeta| = 1$, on the infinite complex plane $\zeta = \xi + i\eta$, $\omega^{-1}(z)$ is the inverse function of $\omega(\zeta)$, and *P*(z) is the polynomial of finite degree defined from the asymptotic behavior $D(z) = P(z) + o(1)$ $(z \to \infty)$ of *D*(z) at infinity. This means that $\omega(\zeta)$ cannot be arbitrary but should result in function *D*(z), defined by equation (4.8), with such a property. Specifically, function *D*(*z*) should be analytic everywhere in the exterior of the inclusion except, perhaps, at infinity where it has a pole of finite degree [*Ru*, 1999]. Fortunately, such functions $\omega(\zeta)$ describe a rather broad class of domains, which includes inclusions of elliptical or more general shapes (see **Appendix 4B**).

Because *P*(*z*) is obtained directly from *D*(z), the advantage of *Ru*'s [1999] representation equations (4.6) – (4.8) is that two unknown functions, $\varphi(z)$ and $\psi(z)$, are expressed through one auxiliary function *D*(z). In addition, the same mapping $\omega(\zeta)$ is

used for the problem of an inclusion in the infinite plane and in the semi-plane. Choosing function *D*(z) in the form of equation (4.8) guarantees that stress functions equations (4.6), (4.7) result in continuous tractions and displacements on the interface between the inclusion and host medium. These functions also satisfy the boundary conditions of zero tractions on the free half-space boundary [*Ru*, 1999].

Inclusion shape and functions *D*(z) and *P*(z) are fully defined by the conformal mapping $\omega(\zeta)$. Once functions *D*(z) and *P*(z) are found, the stress state and displacements are computed using equations (4.5). Using mapping $\omega(\zeta) = R\zeta + (R\zeta)^{-1}d^2 - hi$, *Ru* [1999] obtained these functions for an elliptical inclusion with one axis parallel to the half-space boundary and its center located at depth *h* on the coordinate axis (i.e., when $\beta = 0$ in **Figure 4.5**). If the inclusion is inclined (**Figure 4.5**) and the angle between the inclusion and *x*-axis is β, the function $\omega(\zeta)$ and its inverse $\omega^{-1}(z)$ can be written as (**Appendix 4B**)

$$\omega(z) = ih + \frac{e^{i\beta}}{2}\left[(a+b)\zeta + \frac{a-b}{\zeta}\right], \qquad \omega^{-1}(z) = \frac{e^{-i\beta}(z-ih)}{a+b}\left[1+\sqrt{1-\frac{e^{2i\beta}(a^2-b^2)}{(z-ih)^2}}\right] \quad (4.10)$$

We then find (**Appendix 4B**) that in this case,

$$D(z) = -ih + \frac{(a+b)e^{-i\beta}}{2\omega^{-1}(z)} + \frac{e^{-i\beta}(a-b)}{2}\omega^{-1}(z), \quad P(z) = ih + \frac{a-b}{a+b}e^{-2i\beta}(z-ih) \qquad (4.11)$$

Since functions *D*(z), *P*(z) are known from equations (4.11), stresses and displacements everywhere in the half-space and inclusion can now be computed using equations (4.5), (4.6), and (4.7). Taking into account that $z = \overline{z} = x$ on the surface $y = 0$

of the half-space $y < 0$, we obtain (**Appendix 4B**) the serpentinization-induced displacements

$$u(x,0)+iw(x,0)=\frac{4ab\varepsilon_0}{a^2-b^2}(1+\nu)e^{2i\beta}(x-ih)[1-U(x)] \tag{4.12}$$

and stresses

$$\sigma_{xx}(x)=-\frac{16\mu\varepsilon_0}{\kappa+1}ab\left[\frac{1}{(z+ih)^2(1+\overline{U(x)})\overline{U(x)}}+\frac{1}{(z-ih)^2(1+U(x))U(x)}\right] \tag{4.13}$$

on the seafloor. Here

$$U(x)=\sqrt{1-\frac{e^{-2i\beta}(a^2-b^2)}{(x-ih)^2}} \tag{4.14}$$

Stresses $\sigma_{xx} = \tau_{xy} = 0$ are the boundary conditions on the half-plane boundary. Note that the quantity in brackets in equation (4.13) is real because it is the sum of two conjugate complex numbers.

When $a^2 - b^2 << h^2$, the fraction term under the square root in equation (4.14) is small, and equation (4.12) reduces to equations (4.4) for a cylindrical inclusion, except now $S = \pi ab$ is the cross-sectional area of the elliptical inclusion. This shows that when $b \to a$, equation (4.4) is recovered from equations (4.12) and (4.14) as a particular case. This also shows that for a deep inclusion ($h \to \infty$ or $h >> a$), the uplift is independent of the inclusion orientation and aspect ratio, but is only affected by its volume (or area), where material is transformed by serpentinization. Furthermore, because the *Mindlin and Chen*'s [1950] solution for the dilation center in a half-space can be used as a Green's function, such a deep inclusion does not need to be elliptical, but can be of

arbitrary shape that has cross-sectional area *S*, and equations (4.4) are still applicable to describe the surface deformation. Likewise, stress σ_{xx} at the seafloor in equation (4.13) is also independent of inclusion shape for a sufficiently deep inclusion. In this case, σ_{xx} is the same as that for a circular inclusion of the same cross-sectional area *S* or for the corresponding point (linear) source of dilation.

4.4 Uplift Resulting from Subsurface Serpentinization

4.4.1 Effects of depth and shape of serpentinized domain

To understand possible effects of subsurface serpentinization on the seafloor uplift, we plotted the distribution of the surface displacements when the serpentinized domain with aspect ratio $a/b = 5$ is located at the depth of $h/a = 1.5$ and inclined at the angle of $\beta = 20^\circ$ to the horizontal (solid lines in **Figure 4.6**). For comparison, we also plotted the seafloor displacements that would be caused by a circular region of the same area *S* as an ellipse and located at the same depth *h* (dotted lines in **Figure 4.6**). Hereafter in this section, displacements are normalized by the maximum vertical uplift $w_0 = 2(1 + \nu)S\varepsilon_0/(3\pi h)$ that would be caused by the circular domain while coordinates are normalized by the inclusion depth.

Because the elliptical domain is inclined in this example, the vertical uplift (blue, solid line in **Figure 4.6**) is asymmetric. Neither vertical nor horizontal displacements, however, differ significantly for the cases of elliptical and circular inclusions. This means that the asymptotic approximation of large depth ($h >> a$) is applicable even for a relatively shallow inclusion ($h/a = 1.5$ in **Figure 4.6**). Because the asymptotic solutions

corresponding to large depth do not include the inclusion angle (equations (4.4)), however, this also means that the uplift is relatively insensitive to the angle. In the case of a vertical inclusion of the same aspect ratio ($a/b = 5$) and depth (dashed lines in **Figure 4.6**), the distance, $h - a$, between the upper end of the vertical inclusion and the seafloor is only 5% of the inclusion size, $2a$. Even in this relatively extreme case, the uplift generated by the vertical inclusion differs from that resulting from a circular inclusion of the same volume by no more than by 20%; and even this difference is only noticeable directly above the top of the inclusion (**Figure 4.6)**.

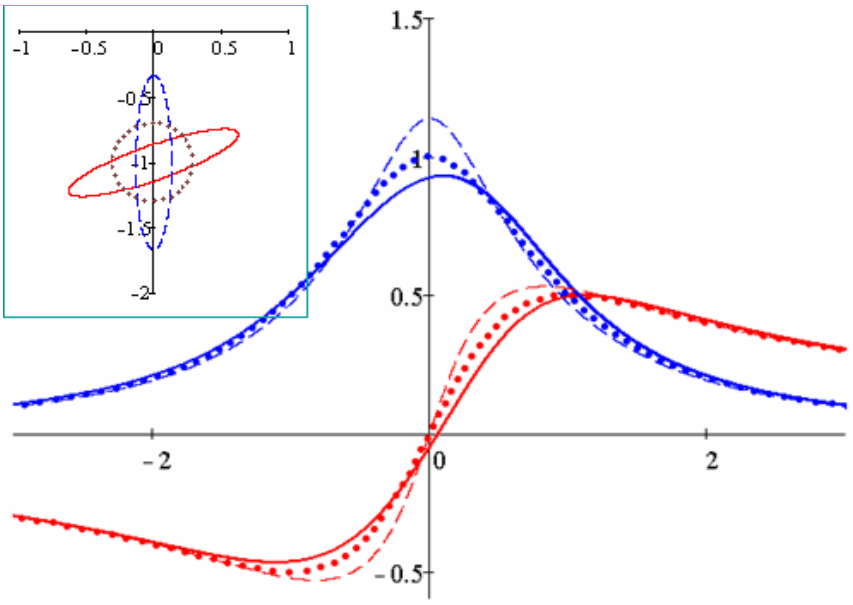

Figure 4.6 Normalized vertical (w/w_0, blue lines) and horizontal (u/w_0, red lines) surface displacements over serpentinized regions (inclusions) as functions of normalized horizontal coordinate (x/h). Dashed and solid lines correspond to the vertical and inclined ($\beta = 20°$) elliptic ($a/b = 5$) inclusions, respectively. Dotted line corresponds to the circular ($a/b = 1$) inclusion. The inclusions are shown in the insets in normalized coordinates (x/h, y/h), located at the same depth ($h/a = 1.5$), and have the same cross sectional area ($S/h^2 = 4\pi/45 \approx 0.279$).

Figure 4.7a shows vertical displacements generated by inclusions with $h/a = 1.8$. The uplifts caused by the inclusions of three different inclinations (0, 45°, and 90°) do not differ from the case of equivalent circular domain by more than 7%. This does not mean that the difference cannot be more significant, however. An example for $a/b = 10$, $h/a = 0.4$, and $\beta = 10°$ is shown in **Figure 4.7b**. In this case, the approximation by an equal-area inclusion (shown on the inset) may not be sufficiently accurate as the difference compared to the exact solution (ellipse on the inset in **Figure 4.7b**) can be nearly 100%.

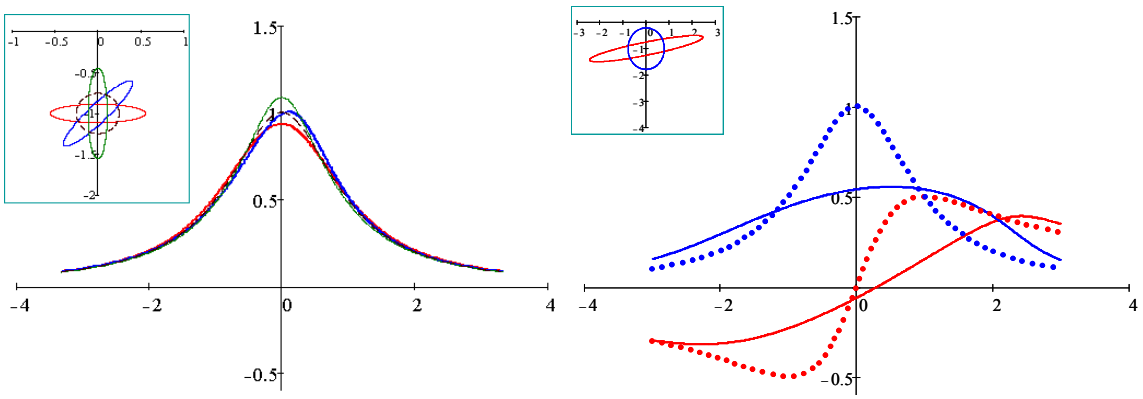

(a) **(b)**

Figure 4.7 Normalized surface displacements caused by sub-surface serpentinization in different domains (shown in the insets in normalized coordinates x/h and y/h) as functions of normalized horizontal coordinate (x/h). **(a)** Normalized uplifts, w/w_0, caused by elliptical ($a/b = 5$) inclusions of different inclinations (horizontal – red line, vertical – green line, and inclined at 45° – blue line) and circular inclusion (dashed line) of the same cross-sectional area ($S/h^2 = 4\pi/45 \approx 0.279$) and depth ($h/a = 1.8$). **(b)** Normalized vertical (w/w_0, blue lines) and horizontal (u/w_0, red lines) surface displacements over inclined elliptical ($\beta = 10°$, $a/b = 10$, solid lines) and circular ($a/b = 1$, dotted lines) inclusions that are located at the same depth ($h/a = 0.4$) and have the same cross sectional area ($S/h^2 = 5\pi/8 \approx 1.963$).

4.4.2 Application to TAG

Figure 4.2 shows the central portion of the east wall of the axial valley at the TAG hydrothermal field (Mid-Atlantic Ridge). The rounded area centered near 26°08.7'N, 44°49.6'W exhibits an anomalous salient that projects about 3.5 km westward into the axial valley. The salient encompasses a domed area about 3 km in diameter (**Figure 4.2**) bounded by the 3725 m and 3625 m isobaths thus indicating a relief of about 100 m. We hypothesize that the observed salient may be a result of serpentinization of a crustal region and determine the volume and the depth of this region that would be consistent with the observed uplift (**Figure 4.2**).

We use equations (4.3) for a sub-surface spherical inclusion to model the TAG salient (**Figure 4.2**). As in 2-D case, it can be shown that uplift resulting from a deep 3-D inclusion ($h >> a$) is independent of the inclusion shape and is only affected by its volume. In other words, such a deep inclusion need not be spherical, but can be of *arbitrary* shape with the same volume V, and equations (4.3) still adequately describe the surface deformation. Furthermore, as shown in the previous section, the asymptotic approximation of large depth ($h >> a$) is applicable in 2-D even for $h/a = 1.5$ (or $h/(2a) = 0.75$). Because the interaction between the inclusion and the surface is weaker in 3-D than in 2-D, the solution (4.3) for large depth is applicable even for shallower inclusions.

According to equations (4.3), the horizontal extent of the uplifted region scales with the inclusion depth. Hence, the 3.5-km-wide TAG salient could have resulted from serpentinization in a region centered at a depth of 1.5 to 2.5 km. The blue dashed lines

in **Figure 4.8** show the distribution of vertical uplift resulting from partial serpentinization, $\varepsilon_0 = 20$ %, in a volume $V = 25$ km^3 centered at a depth of $h = 2.5$ km. The radius of a spherical inclusion corresponding to this volume would be $a = 1.8$ km (dashed line in the inset in **Figure 4.8a**), but the inclusion does not need to be spherical because in this case $h/a = 1.4$, and the asymptotic expression (4.3) is sufficiently accurate (and, in-fact, more accurate than in 2-D case). The red solid lines in **Figure 4.8** show uplift resulting from more complete serpentinization, $\varepsilon_0 = 40$ %, in a smaller volume, $V = 5$ km^3, centered at a depth of $h = 1.6$ km. The corresponding equivalent spherical domain has a radius $a = 1.1$ km, and the ratio $h/a = 1.5$ indicates again that, within limits, the domain can be of arbitrary shape.

For example, suppose that a 3-D elliptically-shaped inclusion, considered in 2-D in Section 4.4.1 ($a/b = 5$, $h/a = 1.5$, $\beta = 20°$) (**Figure 4.5**), is located on the footwall side of the TAG detachment fault (Section 4.2), where gabbro outcrop [Figure 2a; *Zonenshain et al*., 1989] and seismic data suggests the presence of lower crustal and/or serpentinized upper mantle rocks at anomalously shallow depths [*deMartin et al*., 2007; *Canales et al*., 2007]. In this case, the inclusion dimensions could be $2a = 4$ km and $2b = 0.8$ km ($V = \pi a^2 b = 5$ km^3). If the inclusion center were located at the depth of $h = 1.6$ km, the salient topography would again be given by the red solid lines in **Figure 4.8** and would be reasonably close to the observed topography (**Figure 4.2**).

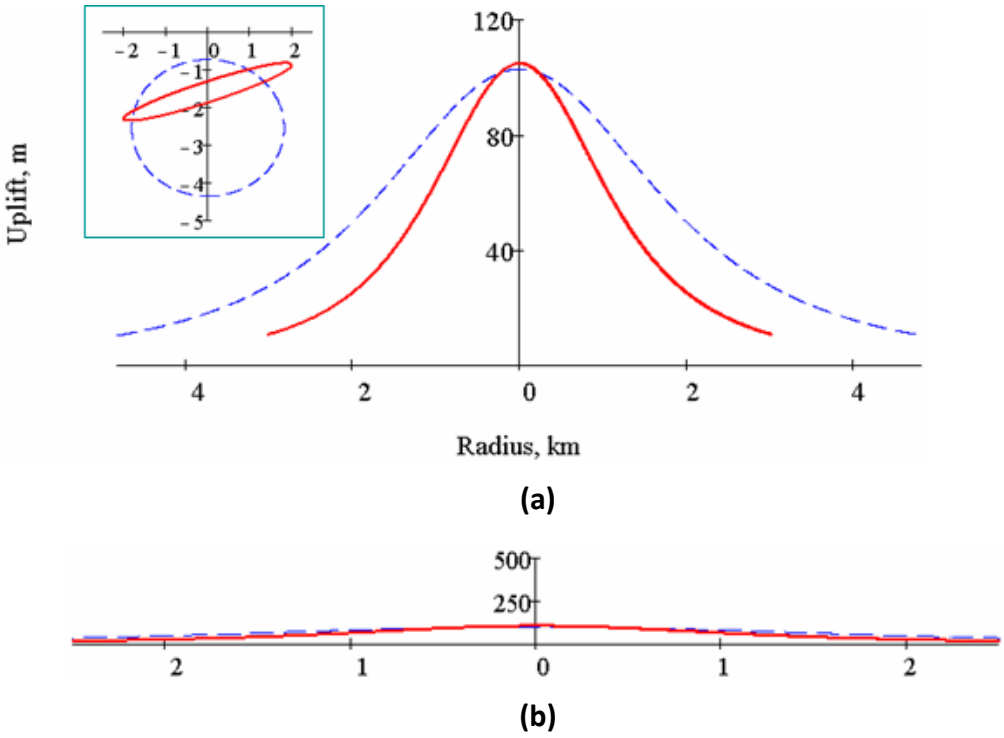

Figure 4.8 An elastic model of the TAG salient topography resulting from partial serpentinization (ε_0 = 20 %) of 25 km^3 of rock at the depth of 2.5 km (dashed line) and massive serpentinization (ε_0 = 40 %) of 5 km^3 at the depth of 1.6 km (solid line). **(a)** Uplift scale (vertical axis) is increased for better visualization. The corresponding geometries and depths of possible serpentinized bodies are shown on the inset. The elliptical inclusion is inclined to the horizontal at the angle of β = 20°. **(b)** Same as (a) but vertical and horizontal scales are equal.

Based on structural observations and seismic and magnetic data, a detachment fault is present in the wall of the axial valley along the eastern margin of the salient. The fault consists of roughly two segments. The shallow segment is inclined at ≈20° and the deep part of the fault has an angle of ≈70° [*deMartin et al.*, 2007]. The salient is underlain by the shallow part of the fault at a depth of ~2 km. The detachment fault may be a conduit for the flow of water into the mantle rock where serpentinization occurs. Our model suggests that the observed salient may have been produced by serpentinization of upper mantle peridotite rocks that were displaced by faulting to a

relatively shallow depth of ~2 km. As **Figure 4.7** indicates, serpentinization of 5 to 25 km^3 located beneath the footwall of the TAG detachment fault would be consistent with the existence of the salient on the seafloor.

It is important to mention, however, that 20 to 40% of transformation strain would most likely be beyond the elastic limit of serpentinized rock [*Jaeger et al.*, 2007]. Hence, plots in **Figure 4.8** probably correspond to the lower limit of the expected seafloor deformation. After serpentinization begins, multiple faulting and fracturing events would probably occur at a transformation strain of several percent, which is much lower than the 40% volume expansion corresponding to massive serpentinization. Such events may occur both inside and outside the serpentinized region and thus may contribute to the development of the detachment fault, rock permeability, and water flow required for serpentinization.

The age of TAG mound $\sim 10^5$ years is nearly the same as the lithospheric age [*Lalou et al.*, 1995]. Therefore, the transformation strain of 20 to 40% can be interpreted as total strain rather than the strain increment. In the next section, we consider an example of transformation strain corresponding to the serpentinization increment that may be small compared to the overall serpentinization level.

4.4.3 Application to the Kyushu-Palau subduction zone

Tahara et al. [2008] attribute the observed Quaternary uplift of the Miyazaki Plain (**Figure 4.3**) to the subduction of the Kyushu-Palau Ridge. They hypothesize that the Ridge might have been detached from the subducted slab below 30 km depth by some mechanism. They further conjecture that the subducting slab may steeply bend

due to a loss of buoyancy beneath the Kyushu Island [Figs. 2 and 8 in *Tahara et al.*, 2008] causing the detached Kyushu-Palau Ridge to move upwards [Fig. 14b in *Tahara et al.*, 2008]. Based on this argument, *Tahara et al*. [2008] suggest that relatively low density materials of the Kyushu-Palau Ridge might have caused the significant aseismic crustal uplift of ~120 m during the past ~120 thousand years at the Miyazaki Plain.

While buoyancy may indeed be an important factor for the crustal uplift observed on the Miyazaki Plain, an alternative and somewhat simpler mechanism could be the volume expansion in the serpentinized regions identified by seismic studies [see *Tahara et al*., 2008 and references therein]. In this scenario, the crustal uplift may have resulted from the serpentinization of mantle rock in the inclined region beneath the Miyazaki Plain and, perhaps, in a sub-horizontal region located near the base of the crust west of the subducted Kyushu-Palau Ridge (see **Figure 4.3**).

A serpentinized region in the mantle forearc beneath the Miyazaki Plain is consistent with seismic data [*Tahara et al*. 2008; *Saiga et al.*, 2010] suggesting an elevated Poisson's ratio (**Figure 4.3)**. Serpentinization likely occurs as water fluxed from the downgoing slab and sediments ascends to the forearc [e.g., *Hyndman et al.*, 1997]. Thermal modeling suggests that maximum temperatures are 350-400° C in the region beneath Hyuganada [*Hyndman et al.*, 1995], which is favorable for serpentinization. Hence, based on the seismic data presented by *Tahara et al*. [2008] and *Saiga et al*. [2010], a 2-D elliptical inclusion could be used to model this region (**Figure 4.3).**

The nature of the sub-horizontal low-velocity, near-normal or low Poisson's ratio region A (**Figure 4.3**) is less clear. *Saiga et al*. [2010] conclude that ratio V_p/V_s of *P*- and

S-wave velocities is low in this region. They hypothesize the accretion of low-density rocks (of a detached Kyushu-Palau Ridge) at the bottom of the crust at the depth of ~30 km beneath the Kyushu Mountains [*Saiga et* al., 2010; Fig. 15]. *Tahara et al.* [2008] offer a similar explanation. Because the mechanisms of mantle hydration in the sub-horizontal region is not obvious [*Salah and Seno*, 2008], we consider below both possibilities of ongoing (but small) and absent serpentinization in this region. We represent the sub-horizontal ellipse shown in domain A in **Figure 4.3b** by a 3-D ellipsoidal inclusion.

We assume the characteristic inclination $\beta \approx 25^\circ$ of the inclined region and its characteristic size (in the vertical cross-section) of $2a_1 \sim 40$ km. The sub-horizontal region appears to be somewhat larger (**Figure 4.3b**), so we assume $2a_2 \sim 60$ km. We finally assume that both regions are located approximately at the same depth of $h \sim 30$ km and have the same cross-sectional area, which results in the thicknesses of $2b_1 \sim 15$ km and $2b_2 \sim 10$ km for the inclined and sub-horizontal inclusion, respectively (**Figure 4.3b**).

Figure 4.9a shows the individual uplift distributions above the horizontal (red dashed line) and inclined ($\beta = 25^\circ$, blue dashed line) elliptical inclusions with such parameters (**Figure 4.9b**). From the solution discussed in Section 4.3, one can compute stresses and displacements not only for a single elliptic inclusion, but also for multiple inclusions in the half-space as long as inclusions do not overlap and do not intersect the half-space boundary. Furthermore, this superposition is permissible even for 2-D (inclined) and 3-D (sub-horizontal) inclusions.

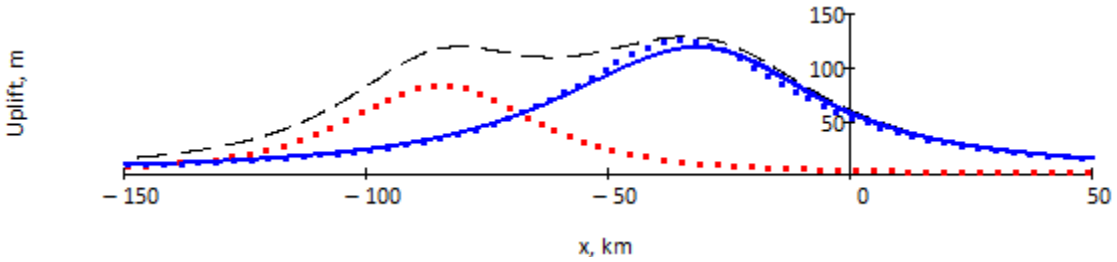

(a)

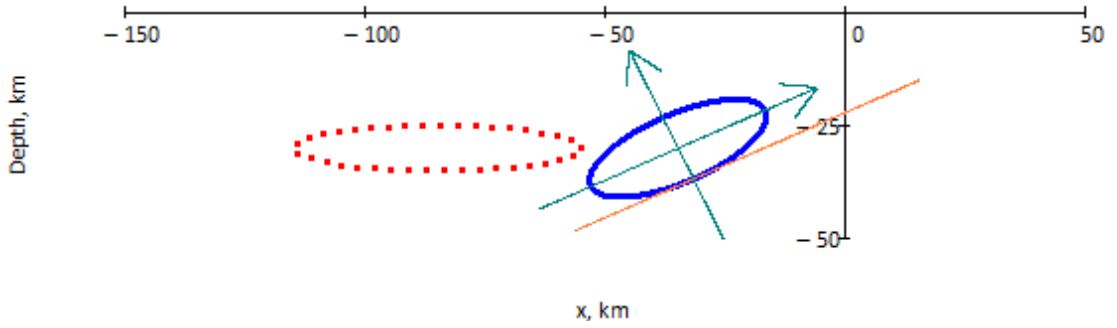

(b)

Figure 4.9 An elastic model of the uplift on Kyushu Island resulting from partial serpentinization (ε_0 = 3 %) of mantle and lower crust. **(a)** Individual uplifts caused by the sub-horizontal (red dotted line) and inclined (blue solid line) serpentinized regions and the resulting uplift (black dashed line) caused by these regions together. **(b)** A configuration of two inclusions representing serpentinized regions (with higher Poisson ratio inferred from the seismic tomography data) in **Figure 4.3**. The inclined (β = 25°) and sub-horizontal regions are modeled by elliptic inclusions, centers of which are located at the depth of h = 30 km. The inclusions have the thickness of $2b_1$ = 15 km and $2b_2$ = 10 km, respectively, and they have the lengths of $2a_1$ = 40 km and $2a_2$ = 60 km. They can be viewed as representing the sub-horizontal region A and inclined region B in **Figure 4.3b**. The coordinate set X, Y is shown by the thin green lines with X-axis along the major axis of the inclined inclusion and parallel to the upper boundary of the subducting plate (and slip zone), indicated by thin orange line (Section 4.5.2).

The combined uplift caused by both inclusions (dashed line in **Figure 4.9a**) is significantly more uniform than the uplifts that would have been caused by each inclusion separately (solid and dashed lines in **Figure 4.9a**). A transformation strain of ε_0 = 3 %, used for calculations shown in **Figure 4.9**, generates uplift close to the detected ~120 m of the Quaternary uplift of the Miyazaki Plain and the mountain range at central

part of the Kyushu Island (west of the Miyazaki Plain in **Figures 4.2b** and **4.8**). The horizontal extent of the uplifted region is $\sim 10^2$ km (**Figure 4.9a**), which is consistent with the scales of topographical features on the Kyushu Island. Because the inclined inclusion is sufficiently deep ($h/a_1 = 1.5$), the difference between the exact solution (blue solid line in **Figure 4.9a**) and that for the equivalent circle (blue dotted lines in **Figure 4.9a**) is negligible. For the 3-D sub-horizontal inclusion, $h/a_1 = 1$. Since the interaction between the inclusion and the surface is weaker in 3-D than in 2-D, we used the equivalent sphere (or point source) solution to plot the surface displacement caused by the sub-horizontal inclusion (red dotted line in **Figure 4.9b**). Because the surface displacements decay faster in 2-D than in 3-D with the increasing distance from the inclusion, the sub-horizontal inclusion does not significantly affect the surface uplift of the Miyazaki Plain (i.e., above the inclined inclusion). In contrast, the 2-D like inclined region contributes nearly 30% of the uplift of the Kyushu Mountains above the sub-horizontal low-velocity region. We are not aware of uplift data north of the Miyazaki Plain, but it would be informative to compare the prediction of our model to the actual uplift in the coastline area east of the Kyushu Mountains. Since the sub-horizontal inclusion would not significantly affect the uplift there, we expect uplift in the range of $\sim 10^2$ m.

We note that the uplift associated with serpentinization occurs over ~120 ka whereas subduction has been occurring for more than 10 Ma [*Seno and Maruyama*, 1984]. Hence, the serpentinization process may be viewed as incremental. That is, $\varepsilon_0 = 3$ % may be a $\Delta\varepsilon_0$ superimposed on previous serpentinization processes. The inferred larger value of Poisson's ratio in this region would not necessarily be

inconsistent with a 6% increment in the amount of serpentinization occurring in the past 120 ka. On the other hand, in the region beneath Northern Kyushu, elevated Poisson's ratio above the subducting slab may be a result of fluid-filled cracks induced by the slab dehydration [*Salah and Seno*, 2008]. In this case, the total level of serpentinization may be small (e.g., several percent) and only slightly contribute to an elevated value of Poisson's ratio.

Similarly, ratio V_p/V_s in the sub-horizontal, low-velocity region, identified by *Saiga et al.* [2010] beneath the Kyushu Mountains (**Figure 4.3b**), may be relatively low because the serpentinization in this region does not exceed a few percent. The aseismic uplift of the Kyushu Mountains appears to be ongoing over the last 2 Ma [*Kamata and Kodama*, 1999; *Saiga et al*., 2010]. If during this time period, the uplift has been primarily caused by the serpentinization processes, the total level of serpentinization in the low-velocity region A in **Figure 4.3b** is unlikely to exceed several percent in order to be consistent with the uplift of $\sim 10^2$ m. Our results, therefore, may help to constrain the level of serpentinization in this region.

In general, the geological situation near Kyushu Island is quite complicated (e.g., **Figure 4.3**) and other mechanisms may be contributing to the ongoing crustal uplift. Yet our simple elastic model appears to adequately describe the uplift magnitude, and it is consistent with the geological structure inferred from the seismic data as well as with available data on the Quaternary crustal uplift determined from the shoreline heights [*Shimoyama et al.*, 1999; *Nakada*, 2002]. The required serpentinization strain increment

of 3% is much smaller than in the TAG salient case (Section 4.4.2), and could be more consistent with the assumption of linear elastic model.

4.5 Localized Failure Associated with Serpentinization

In previous sections we focused primarily on the uplift associated with a serpentinized region at depth by calculating the elastic strains caused by subsurface inclusions of different shapes. Based on the formulation of the problem in this manner also allows elastic stresses and strains to be determined everywhere in the half space. In the case of large transformational strains, such as may be associated with the anomalous topography at the TAG hydrothermal field, faulting and fracturing may occur in addition to simple surface deformation and uplift. The pattern of faulting and/or fracturing that might occur is likely to depend on the shape of the inclusion even though the surface uplift may not. Although large-strain and failure-based analyses may provide better constraints on the geometry of the serpentinized region at TAG, we further use the linear elastic model (Sections 4.2 and 4.3) to estimate the effect of serpentinization on faulting underneath the TAG region. On the other hand, only relatively small 3% transformational strain increment associated with serpentinization appears to be required to explain uplifts of the Miyazaki Plain and Kyushu Mountains (**Figures 4.3** and **4.9**). For such small strains, the elastic theory presented here is more likely to be adequate.

4.5.1 Failure criterion

To first order, the effect of serpentinization on the tendency of the fault to slip could be considered based on the Mohr-Coulomb criterion [e.g., *Jaeger et al*., 2007]. The simplest approach would be to neglect the effect of the fault itself on the deformation and assume that stress changes resulting from serpentinization develop on the background of existing tectonic stresses. This is similar to describing the tendency of the fault to become unstable as a result of petroleum production [e.g., *Segall and Fitzgerald*, 1998; *Rudnicki*, 1999; *Chanpura and Germanovich*, 2004] where the petroleum reservoir deforms in response to changing pore pressure and causes the stress state to deviate towards or away from failure. Here we use a similar approach considering failure along the identified fault plane or slip zone

According to the Mohr-Coulomb criterion, the approach of the stress state on a fault plane towards the failure envelope can be described by the Coulomb stress

$$\Delta T = \mathrm{sign}(\tau_0)\Delta\tau_{XY} + (\Delta\sigma_{YY} + \Delta p)\tan\varphi \qquad (4.15)$$

where τ_0 is the background (initial) tectonic shear stress on the fault plane, $\Delta\tau_{XY}$ and $\Delta\sigma_{YY}$ represent changes of the shear and normal stress components on the fault plane, respectively, Δp is the pore pressure change, and compressive stresses are negative. In all our examples, *X*- axis is aligned along the long axis of the elliptic inclusion (**Figure 4.5**) and is parallel to the fault or slip zone (e.g., **Figure 4.9b**). In general, in the normal faulting regime, $\tau_0 < 0$ if $0 \le \theta < \pi/2$ while $\tau_0 > 0$ if $\pi/2 \le \theta < \pi$, where θ is the fault (*X*-axis) angle in the counter-clock direction with respect to the horizontal ($\theta = \beta$ in **Figure 4.5**). The reverse faulting regime is characterized by $\tau_0 > 0$ if $0 \le \theta < \pi/2$ and $\tau_0 < 0$

if $\pi/2 \leq \theta < \pi$. This is equivalent to the usual sign convention for shear stress such that it is positive when it gives rise to a couple on the plane in the clockwise direction [e.g., *Timoshenko and Goodier*, 1970]. We assume here that the stress changes do not reverse the fault slip direction, so that the quantity $\text{sign}(\tau_0)\Delta\tau_{XY}$ in equation (4.15) is positive in the direction of fault slip.

In various forms, the Coulomb stress concept has been employed in many earthquakes studies [e.g., *King et al*., 1994; *Cocco and Rice*, 2002; *Smith and Sandwell*, 2003; *Steacy et al*., 2005; *Ryder et al*., 2012]. The sign of ΔT characterizes whether the stress state moves closer towards or further away from the failure surface. The stress change has a tendency to *destabilize* the fault when $\Delta T > 0$. In this case, the stress state moves closer to failure. Note that except for the general information on the nature of the regional stress regime (normal faulting or thrust), ΔT in equation (4.15) does not require knowing the initial stresses and only the sign of τ_0 is required. Because equation (4.15) reflects stress increments, rather than their absolute values, the Coulomb stress on the pre-existing fault is only affected by the friction angle, while cohesion of the fault material is not present in equation (4.15) as long as it does not change as a result of deformation.

4.5.2 Serpentinization and faulting at the Miyazaki Plain region

The serpentinization of the forearc mantle may have important tectonic implications [e.g., *Hyndman et al.*, 1997; *Seno*, 2005; *Kirby et al.*, 2006]. In particular, *Tahara et al*. [2008] argue that the well-developed serpentinized mantle wedge may be a plausible cause of aseismic slip and relatively low maximum magnitude of events in

the Hyuganada region. In the Kyushu-Palau subduction zone, the Philippine Sea Plate converges under the Eurasia Plate, which corresponds to a thrust-type tectonic regime in slip zones (**Figure 4.3**) detected by *Yagi and Kikuchi* [2003]. Along the coastline of eastern Kyushu, the depths of Moho discontinuity and the surface of the subducting slab are about 30 km and 40 km, respectively [e.g., *Tahara et al.*, 2008]. The detected region with high Poisson's ratio (**Figure 4.3**) is situated along the upper boundary of the subducting slab [*Tahara et al*., 2008; *Saiga et al*., 2010]. In the Kyushu-Palau subduction zone, most of the interplate, thrust-type earthquakes occur near this boundary–[*Yagi and Kikuchi*, 2003; *Salah and Seno*, 2008]. Hence, in our simplified model (**Figure 4.9b**) of the Miyazaki Plain situation, the slip zone (thin orange line) is located just below the inclined serpentinized inclusion (solid blue line). In general, an inclusion at the hanging wall of a thrust fault (considered in this section) and the Francis's scenario (**Figure 4.1a**) of the serpentinization domain at the footwall of a normal fault (considered in Section 4.5.3) represent two end-members.

Figure 4.10a shows changes of the normalized shear, $\Delta\tau_{XY}/A$ (red line) and normal, $\Delta\sigma_{YY}/A$ (blue line), stresses on the upper boundary of the subducting Phillipine Sea Plate (or aseismic thrust zone shown by thin orange line in **Figure 4.9b**) that underlines the serpentinized domain beneath the Miyazaki Plain (**Figure 4.3**). As above, this domain is represented by the inclined elliptic inclusion in **Figure 4.9b,** and the axis X of the rotated coordinate set (thin green lines) is parallel to "fault plane" and coincides with the axis of the inclined domain in **Figure 4.9b**. The stress distributions in **Figure 4.10a** are almost symmetric with respect to $X = 0$ because of the weak interaction

with the sub-horizontal serpentinization domain (**Figures 4.2b** and **4.8**) and with the Earth surface, $y = 0$. Dotted lines show the stresses on the same fault (slip zone) in the absence of the subhorizontal domain. The interaction is weak because the inclined inclusion is realtively deep ($h/a_1 = 1.5$) and because the sub-horizontal inclusion is three-dimensional, so its effect on the stress state decays as the inversed cube of the distance from the inclusion center. This is why in **Figure 4.10a**, the dotted lines almost coincide with solid lines (showing stresses when both inclusions are present), which suggests that the effect of the sub-horizontal inclusion on the stress state is indeed small. **Figure 4.10a** shows stress distribution in cross-section RR' (**Figure 4.3a**), where the effect of the sub-horizontal inclusion is the strongest. Away from this cross-section, for example along line BB' in **Figure 4.3a**, the interaction between the inclusions is even weaker, so the model of a single 2-D inclined inclusion appears to be adequate. Hereafter, we use the characteristic stress A in equation (4.9) for normalizing stresses. This is convenient because A is independent of the inclusion dimensions. In addition, because A is also proportional to ε_0, the normalized stresses in **Figures 4.10a** and **4.10b** are independent of the transformation strain.

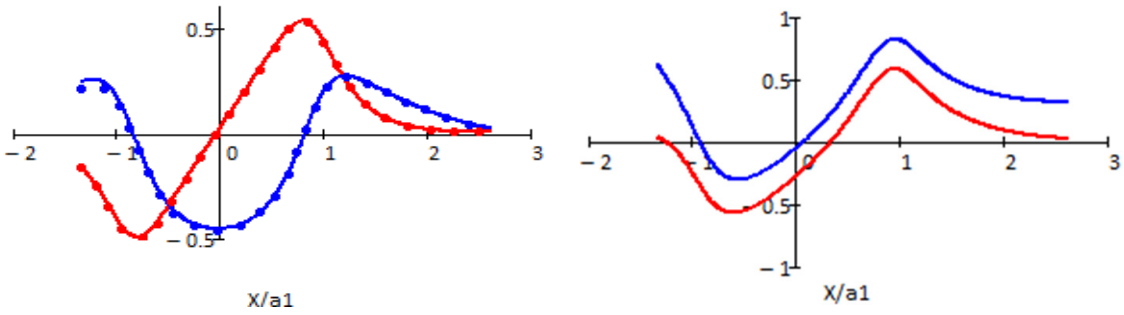

(a) **(b)**

Figure 4.10 (a) Shear (red lines) and normal (blue lines) stress changes on the slip zone, which underlies the inclined serpentinized domain shown in **Figure 4.9b**. Stresses are normalized by the mean stress $A = (4/3)\mu(1 + \nu)\varepsilon_0/(\kappa + 1)$ (equation (4.9)) that would be caused by the same transformation strain inside the same inclusion if it were located in the infinite plane. Solid lines correspond to the case of two inclusions while dotted lines show the stresses along the slip zone without taking into account the sub-horizontal domain. **(b)** Distribution of the normalized Coulomb stress, T/A, along the the slip zone. Skempton coefficients $B = 0$ (red line) and $B = 1$ (black line) correspond to two limiting cases of the drained and (strongest possible) undrained deformations, respectively. Coordinate X (**Figures 4.5** and **4.9b**) along the slip zone is normalized by the major semi-axis, a_1, of the inclined ellipse.

The distribution of the corresponding normalized Coulomb stress, $\Delta T/A$, on the fault plane is given in **Figure 4.10b**. The pressure change Δp in equation (4.15) was estimated using the Skempton relation for a poroelastic material $\Delta p = -B\Delta I_1/3$ [e.g., *Detournay and Cheng*, *1993*], where B is the Skempton coefficient and $\Delta I_1 = \sigma_{xx} + \sigma_{yy} + \sigma_{zz}$ is the first stress invariant. In the case of inclined inclusion, expressions (4.5), (4.6), (4.7), and (4.11) were used to determine transformation stresses σ_{xx} and σ_{yy}, and the plane strain relation $\sigma_{zz} = \nu(\sigma_{xx} + \sigma_{yy}) - E\varepsilon_0/3$ [e.g., *Timoshenko and Goodier*, 1970] between the stresses was used to evaluate σ_{zz}. The contribution of the sub-horizontal inclusion to ΔI_1 was computed based on the axisymmetric solution of *Mindlin and Chen* [1950].

In general, the Skempton coefficient B ranges between the thermodynamic bounds of 0 and 1 [*Detournay and Cheng*, *1993*]. The case of $B = 0$ (red line in **Figure 4.10b**) corresponds to the drained case, when the fluid pressure does not change as the transformation strain is accumulated. The case of $B = 1$ (blue line in **Figure 4.10b**) represents another extreme of the (strongest possible) undrained deformation. The limited available data suggests that the Skempton coefficient is in the range of 0.5 - 0.9 for igneous rocks [*Detournay and Cheng*, *1993*]. We are not aware of data for the Skempton coefficient for metamorphic rocks, but in any event, the Skempton relation characterizes the undrained response of the pore pressure to stress changes (unless $B = 0$). It is often used for computing Coulomb stresses in earthquake studies [e.g., see *Cocco and Rice*, 2002, and reference therein], when the rock loading is relatively fast. For much slower deformational processes associated with serpentinization reactions, one need to evaluate the relative timescales of stress change and pressure dissipation. Although the drained response is probably more realistic, in **Figure 4.10b** and further in the paper we present both end member cases of $B = 0$ and $B = 1$.

Values of the friction coefficient typically used in calculations of the Coulomb stress range between 0.6 and 0.8 [*Cocco and Rice*, 2002]. Because serpentine has a reduced friction coefficient ($\sim$0.2 according to *Escartin et al.* [1997a, 1997b, 2001]), even partially serpentinized material may considerably decrease the friction coefficient in the slip zone. For **Figure 4.10b** and below, we used a conservative value 0.7, which is consistent with *Byerlee's* [1978] law.

As can be observed from **Figure 4.10b**, the difference between the Coulomb stresses computed in the drained ($B = 0$) and undrained cases ($B = 1$) is not significant. In both cases, the stress change, caused by the serpentinization, is favorable for fault slip and seismic events approximately at $X > 0$ (the coordinate set is shown in **Figures 4.5** and **4.9**) where $T > 0$. The positive sign of the shear stress change in **Figure 4.10a** (red line) is consistent with the thrust-type tectonic shear stresses near the aseismic slip zone in the Kyushu-Palau subduction zone (blue line in **Figure 4.8**). At approximately $X > 0$, $T < 0$, and the stress changes are not favorable for thrust-type events in this part of the slip zone. Therefore, our results indicate a possibility of serpentinization-related strengthening ($T < 0$) of the slip zone $X < 0$ below the central part of the serpentinized domain where the slip zone "touches" the serpentinized domain. Above this place, there is a tendency for serpentinization-enhanced weakening ($T < 0$ and $\Delta\tau_{XY} > 0$) of a significant part $X > 0$ of the slip zone.

It is important to emphasize that the faulting and fracturing activity in slip zones may be related to other subduction processes rather than to serpentinization of the mantle wedge. Also, we computed Coulomb stresses on a specified plane of the potential slip. Instead, Coulomb stress changes can be computed on optimally orientated planes, which presumes that the faults with highest ΔT will be most likely to slip [e.g., *King et al.*, 1994]. The elongated inclined inclusion (**Figures 4.3** and **4.9**) generates tensile stress changes in the surrounding material in the direction parallel to its long axis and compressive stress changes in the perpendicular direction. Because of a relatively mild inclusion inclination (25°), this corresponds to promoting normal-fault

events in the region below the serpentinined domain. This is consistent with *Tahara et al.* [2008] who note that intraplate earthquakes associated with normal faulting occur in the Hyuganada region beneath where serpentinization may be occurring.

4.5.3 Effect of serpentinization on normal faulting

Francis [1981] proposed several scenarios of the effect of serpentinization on faulting. In the case of normal faulting, he suggested that, rocks beneath the footwall of a normal fault hydrate as a result of seawater infiltrating down the fault, so that serpentinization occurs generating more movement on the fault and uplift (**Figure 4.1a**). To quantify this scenario, we consider its simplified version when a circular, serpentinized inclusion is located at the footwall of a normal fault (**Figure 4.11a**). Shear (dotted line), normal (dashed line) and Coulomb (solid lines) stresses, normalized by *A*, are shown in **Figure 4.11b**. The stresses are plotted along the part of the normal fault shown in **Figure 4.11a** by the red line. In general, above the serpentinized domain, Coulomb stress on the fault is positive while the shear stress is negative (**Figure 4.11a**). The latter is consistent with the direction of slip on a normal fault. Consequently, the serpentinization process would tend to enhance the slip on this part of the fault, and, in turn, fault slip may enhance the access of water required for the serpentinization reactions.

4.5.4 Serpentinization and detachment fault at TAG

We note again that the small-strain elastic consideration such as in **Figures 4.10** and **4.11** is only applicable to small transformation strains, probably, no more than a few percent. This is why we do not consider here larger strains such as expected in the TAG region (Section 4.4.2) and for which either large-strain elastic or inelastic considerations would be more appropriate. Instead we consider an increment, $\Delta\varepsilon_0$, of the transformation strain on the background transformation strain, ε_0, that may be happening beneath the TAG field. Assuming that small $\Delta\varepsilon_0$ causes small stress increments, we treat them as being elastic and employ equations (4.5) – (4.11), where we replace ε_0 with $\Delta\varepsilon_0$.

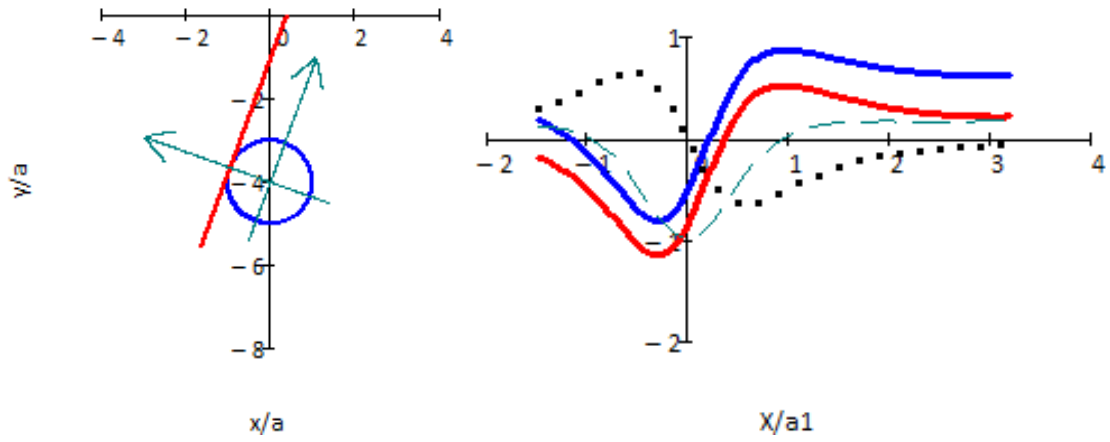

Figure 4.11 (a) A model of *Francis*'s [1981] scenario of serpentinization at the footwall of a normal fault (**Figure 4.1a**). Both vertical and horizontal coordinates are normalized by the radius, *a*, of the circular inclusion. Coordinate set *X*, *Y* is shown by the thin green lines with *X*-axis parallel to the fault. **(b)** Coulomb (solid lines), shear (dotted line), and normal (dashed line) stresses (normalized by *A*) along the fault plane shown in (a).

Figure 4.12a shows a simple model of serpentinization at the footwall of a TAG-like detachment fault. We use the same geometry of the elliptical inclusion as in **Figure 4.7b**. That is, the inclusion center is at the depth of h = 1.6 km and its axes are $2a$ = 4 km and $2b$ = 0.8 km. As discussed in Section 4.4.2, massive serpentinization ($\varepsilon_0 \approx 40\%$) in the 3-D elastic domain is required to cause the observed uplift at TAG (**Figure 4.2**). Here we consider a 2-D inclusion, elongated horizontally along the detachment fault, and analyze the possible effect of serpentinization on both the detachment fault and on normal faults that are typically associated with detachment faults [e.g., *Buck*, 1988; *Lister et al*., 1986] and appear to be present at the TAG area [*deMartin*, 2007]. Examples of such normal faults are shown in **Figure 4.12a** by three parallel lines inclined at the angle of $\theta = 70°$ to the horizontal and connecting the seafloor with the detachment fault. We ignore the effects of the irregularities caused by the faults at the seafloor.

In the extreme case of the strongest Skempton effect (B = 1), Coulomb stresses (not shown in **Figure 4.12b**) are positive on all three normal faults. Shear stresses (solid lines in **Figure 4.12b**) are negative everywhere on the normal faults. Hence, the serpentinization would tend to bring the faults closer to failure because the negative sign of shear stresses is consistent with slip direction on the normal fault ($\tau_0 < 0$ for $0 \le \theta < \pi/2$). In another extreme case, Skempton coefficient B = 0. Then, Coulomb stresses (dashed lines in **Figure 4.12b**) may become negative on deeper normal faults, but are still positive on the shallowest normal fault shown on the right in **Figure 4.12a**. A

real situation would be somewhere in between, although $B = 0$ is probably more realistic for TAG conditions.

This analysis indicates that serpentinization in a relatively shallow domain at the footwall of a detachment fault tends to enhance the permeability of the associated normal faults (**Figure 4.12a**). Hence, normal faulting may provide pathways for water needed for serpentinization reactions. This may be particularly significant because similar computations for the detachment fault suggest that for entire range of the Skempton coefficient ($0 \leq B \leq 1$), serpentinization tends to enhance the slip on the detachment fault above the upper half of the serpentinized inclusion (see also *Francis*'s [1981] and scenario in **Figure 4.11**). This is why shallower normal faults (such as the normal fault on the right in **Figure 4.12a**), may be important water pathways for keeping the serpentinization process going.

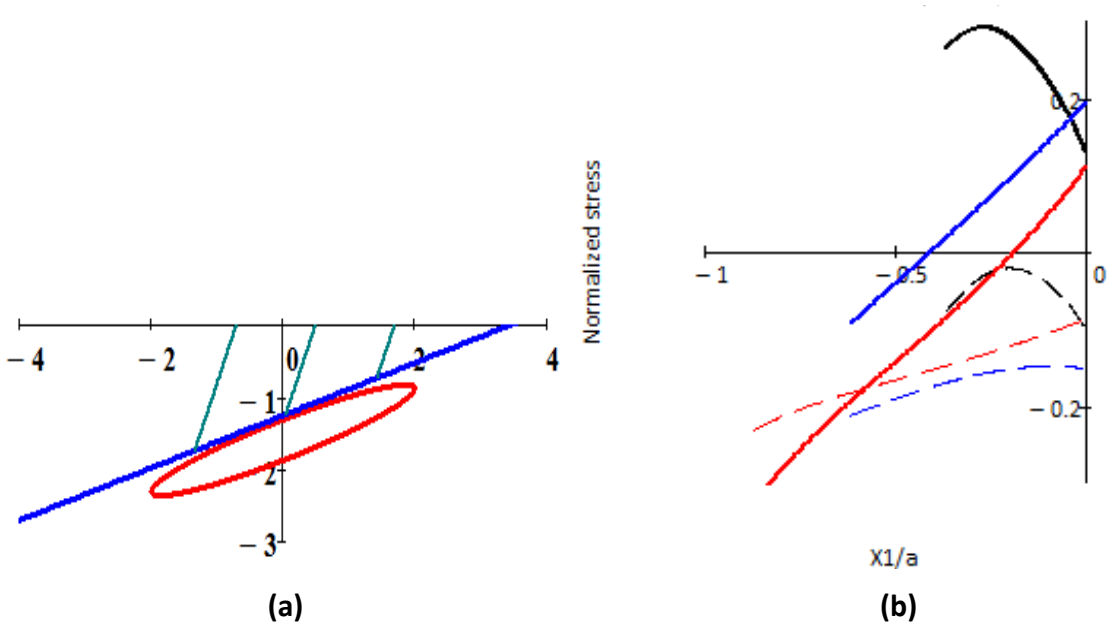

Figure 4.12 (a) A 2-D model of elliptical serpentinization domain (blue line) at the footwall of the TAG detachment fault (red line) and three representative cases of normal faults (green lines inclined at 70° to the horizontal) associated with the detachment fault. The inclusion is located at the depth of $h = 1.6$ km and has axes of $2a = 4$ km and $2b = 0.8$ km. Both vertical and horizontal coordinates are in km. **(b)** Coulomb (solid lines) and shear (dashed lines) stresses (normalized by A) on the normal faults that shown in (a) by green lines. Black, blue, and red lines correspond to the left, middle, and right faults in (a), respectively. Calculations were done for both $B = 1$ and $B = 0$, but only the results for drained conditions ($B = 0$), which is probably more realistic for TAG, are shown. Shear stress is independent of B. For each normal fault, coordinate X is directed along the fault plane with its zero being on the seafloor.

4.6 Discussion

4.6.1 Effects of depth and shape of serpentinized domain on seafloor uplift

While interior displacements caused by a point dilation source differ from those due to a spherical inclusion in the elastic half-space, the surface displacements are identical and expressions (4.3) give the exact solution for both cases. Similarly, solution (4.4) for the surface displacement caused by the circular (cylindrical) inclusion is the same as that for the 2-D point source in the elastic half-plane. Hence, as far as the

surface uplift is concerned, both spherical and circular cylindrical inclusions in the half space can be represented by a point source (3-D or 2-D, respectively) regardless of their depth. This is not the case for inclusions of other shapes.

When the inclusion depth, h, is of the order of its size, $2a$, or greater, the resulting surface uplift is relatively insensitive to the shape and orientation of inclusions with the same volume (Section 4.4.1). In general, it is well known that asymptotic solutions may be applicable even when asymptotic parameters are not necessarily small or large. In particular, this has been observed in solutions for surface subsidence caused by horizontal tunnels [*Pinto and Whittle*, 2006; *Puzrin et al.*, 2012], for surface uplift caused by a pressurized magma chamber [*Segal*, 2010], and for fractures interacting with a body boundary [e.g., *Dyskin et al*., 2000]. For example, *McTigue* [1987] considers a pressurized, spherical magma chamber in an elastic half-space and represents the surface uplift as a series of powers of a/h, where a is the chamber radius and h is its depth. The leading-order term in his expression for the surface uplift is proportional to $(a/h)^3$ and recovers *Mogi*'s [1958] point dilatation model. The second, higher order term accounts for the cavity size, but this correction is rather weak, of the order of $(a/h)^6$. This result allowed *McTigue*'s [1987] to explain why *Mogi's* [1958] approach works reasonably well even when a/h is close to 1.

A similar argument applies for the stress-strain state perturbed by the inclusion considered in this work. For example, when $a^2 - b^2 << h^2$, the fraction term in equation (4.14) is small, so equation (4.14) can be written as

$$u(x,0)+iw(x,0)=2ab\frac{\varepsilon_0(1+\nu)}{3}\frac{x+ih}{x^2+h^2}\left[1+\frac{e^{-2i\beta}(a^2-b^2)}{4}\frac{(x+ih)^2}{(x^2+h^2)^2}+O(\varepsilon^4)\right] \quad (4.16)$$

where $\varepsilon = (a^2 - b^2)^{1/2}/h$ and $O(\varepsilon^4)$ indicates the omitted terms of the higher order. The leading-order terms for the vertical and horizontal surface displacements in equation (4.16) are $O(\varepsilon^2)$ and $O(\varepsilon)$, respectively. The second term in equation (4.16) provides corrections for the inclusion shape and depth that are of the order of $O(\varepsilon^2)$ and $O(\varepsilon^4)$, respectively. Hence, in both cases the correction is two orders higher in the powers of ε. For all computations in this work we used the exact solution (4.13) rather than its asymptotic expansion (4.16). The latter helps, however, to show why the source solution (4.4) works well even when ε is not considerably smaller than one.

In 3-D, the difference between the point-source solution [*Mindlin and Chen*, 1950; *Mogi*, 1958] and its main correction is *three* orders [*McTigue*'s, 1987] rather than two orders in 2-D. Hence, the effect of the free surface and inclusion shape is weaker in three-dimensional geometries than in two-dimensional. We used this observation in Sections 4.4.2, 4.4.3, and 4.5.2.

Currently, the existence of serpentinized mantle associated with the subduction of the oceanic crust is inferred from seismic tomography data [*Salah and Seno*, 2008; *Hyndman and Peacock*, 2003] such as the downdip limit of interplate thrust earthquakes [e.g., *Hyndman et al.*, 1997], intraslab earthquakes within the crust part of the subducting slab [e.g., *Seno*, 2005], low-frequency tremors in the forearc [*Seno and Yamasaki*, 2003; *Matsubara et al.*, 2008], and from the V_p/V_s ratio obtained by seismic tomography [*Salah and Seno*, 2008; *Tahara et al.*, 2008]. Our results indicate that uplift

data may provide an additional constraint on inferring serpentinization from geological and seismological observations.

4.6.2 Tensile fracturing

Based on the *Eshelby* [e.g., *Jaswon and Bhargava*, 1961] or *Mindlin and Chen* [1950] solutions among others, it is expected that tensile stresses could be generated in the material surrounding a dilating body. Tensile stresses may induce or enhance tensile fracturing in rock because typically tensile strength of rocks is relatively low [e.g., *Jaeger et al*., 2007]. In the context of this work, tensile fractures could enhance rock permeability providing better water access to the serpentinizing body. As an example, we evaluate the stress state near the seafloor. Because at or near the free surface, σ_{yy} and τ_{xy} stress components are zero or small due to the boundary conditions, we concentrate on the normal stress σ_{xx}.

This stresses can be easily computed using the exact solution (4.13). To simplify analysis, however, we follow the above consideration for displacements, and consider a deep inclusion. Similar to equation (4.17), when $a^2 - b^2 << h^2$, equation (4.18) can be written as

$$\sigma_{xx}(x) = \frac{16\varepsilon_0(1+\nu)\mu}{3\pi(\kappa+1)} S \frac{h^2 - x^2}{(h^2 + x^2)^2}[1 + O(\varepsilon^4)] \qquad (4.17)$$

where $S = \pi ab$ is the domain cross-sectional area and the small parameter $\varepsilon = (a^2 - b^2)^{1/2}/h$ is the same as in equation (4.16). Expression (4.17) can also be obtained by the integration of the *Mindlin and Chen* [1950] 3-D source solution and represents its 2-D equivalent. Numerical comparison of equations (4.17) and (4.13) shows that in general,

asymptotic expression (4.17) deviates considerably from the exact solution (4.13) only when the inclusion depth becomes smaller than its size.

We see from equation (4.17) that $\sigma_{xx} > 0$ (i.e., tensile) if $-h < x < h$. In other words, the volumetric extension in a relatively deep (i.e., $a^2 - b^2 << h^2$) serpentinization domain may promote tensile fracturing on or near the seafloor just above the domain and regardless of its shape. We note that *Karson and Rona* [1990] and *Bohnenstiehl and Kleinrock* [2011] observed open fissures on the ocean floor in the vicinity of the active hydrothermal mound at the TAG area. While not necessarily created by the serpentinization transformation strain, location of the fissure zone is consistent with our results. Indeed, the fissure zone is located on the hanging wall of the detachment fault and above the possible serpentinization domain inferred by *Palmer* [1996] and *deMartin et al*. [2007] from vent chemistry and seismic observations.

4.6.3 Fluid flow and heat transfer

The exothermic character of serpentinization reactions [*Fyfe and Londsdale*, 1981; *Macdonald and Fyfe*, 1985] and the chemical signatures associated with serpentinization reactions [*Janecky and Seyfried*, 1986; *Berndt et al.*, 1996; *Allen and Seyfried Jr.*, 2003] may provide controls on both physical and biogeochemical aspects of seafloor hydrothermal activity. This is especially relevant at slow-spreading ridges where the magma budget is low [*Lowell and Rona*, 2002; *Rona*, 2008].

The models described here do not include the dynamical processes of fluid and heat transfer associated with large scale serpentinization. As a result of volume expansion associated with serpentinization, permeable pathways may tend to close.

However, as transformational strains grow, the stresses generated are likely to generate new permeable pathways for fluid to access fresh rock. This may be especially relevant when serpentinization occurs near an active fault such as the detachment fault at TAG or Atlantis Massif [*Boschi et al.*, 2006].

To obtain a rough estimate of the rate of serpentinization and the potential for exothermic heat release to impact hydrothermal temperatures, we consider the results for the topographic salient at TAG discussed in Section 4.4.2. The rate of serpentinization $\dot{M}$ is given by

$$\dot{M} \sim \rho_r V \phi / t \tag{4.18}$$

where $\rho_r \approx 2500$ kg/m^3 is the density of serpentine, V is the volume of the body undergoing serpentinization, ϕ is the fraction of the body that has been serpentinized, and t is the time over which reaction occurs. For example, if the TAG salient (**Figure 4.2**) is the result of serpentinization of ≈40% of a 25 km^3 volume over 10^5 years (here, $\phi = 40\%$ corresponds to $\varepsilon_0 \approx 20\,\%$ in **Figure 4.7**), expression (4.17) results in $\dot{M} \approx 10$ kg/s. At this rate, the hydrothermal temperature increase resulting from exothermic heat production would be small compared to the observed black smoker temperatures at TAG [*Lowell and Rona*, 2002], which indicates that serpentinization reactions at TAG are not likely to be the main contributor to the hydrothermal heat output at TAG. Moreover, the small transformation (thermoelastic) strains that would be associated with these small temperature changes are negligible compared with the strains associated with the serpentinization process itself. The domed salient or projection in the east wall of the axial valley beneath the most active part of the TAG

hydrothermal field occurs in the hanging wall of the detachment fault zone above a serpentinized body inferred to occur beneath the underlying footwall (**Figures 4.1a** and **4.10a**). The small scale of this feature suggests that it is not likely a result of flexure of the lithosphere, nor does the salient appear to be a volcanic construct.

The solution for the uplift of the Miyazaki Plain is dominated by the two-dimensional, inclined inclusion with the area undergoing serpentinization of $\pi a_1 b_1$ = 1885 km^2 (**Figure 4.9**). In this case, $\phi \approx 6\%$ of the region is serpentinized over 1.2×10^5 years ($\phi = 6\%$ corresponds to $\varepsilon_0 \approx 3\ \%$ in **Figure 4.9**). Assuming that the third dimension is at least $L \sim 100$ kilometers and using equation (4.18) to estimate the rate of serpentinization, we obtain $\dot{M} \approx 8\times10^3$ kg/s. Therefore, the rate of serpentinization at the Miyazaki Plain site is significantly greater than that at TAG. This is because the volume undergoing serpentinization is much greater than at TAG. The specific serpentinization rate (per rock unit volume) scales as $\dot{M}/V \sim \rho_r \phi / t$, however, and this rate appears to be much greater for TAG ($\sim10^{-2}$ kg/(m^{3}yr)) than for Miyazaki Plain ($\sim10^{-3}$ kg/(m^{3}yr)). Because the rate of serpentinization at the Miyazaki Plain is even smaller than at TAG, its effect on the thermal regime is also expected to be small. The strain and surface uplift associated with the heat release from serpentinization is therefore negligible compared with the transformation strain resulting from serpentinization.

If we assume that approximately 1 mole of H_2O is required to serpentinize each mole of peridotite [*O'Hanley*, 1992], the rate of 8×10^3 kg/s would require a mass flux of H_2O of $\sim10^3$ kg/s. Presumably this water flux could be provided by dewatering of the

subducting slab [*Hyndman et al.*, 1997]. While we recognize that there may be other factors contributing to the uplift, this result may provide an important constraint for modeling the interplay between the serpentinization and the water cycle in subduction zones [e.g., *Rüpke et al.*, 2004].

4.7 Conclusions

In this paper, we calculated the transformation strain associated with spherically, cylindrically and elliptically shaped inclusions in an elastic half space to determine the resulting crustal deformation, stress change, and surface uplift. We showed that if the normalized depth, $h/(2a)$ of the inclusion was greater than ≈ 0.75, the resulting surface uplift was relatively insensitive to the shape and orientation of inclusions with the same volume.

Application of the results to explain the anomalous salient that extends 3.5 km westward from the east wall of the axial valley at the TAG hydrothermal field suggests that this feature may result from a serpentinized body at depth beneath the footwall of a detachment fault. Because the depth of the potential serpentinized region beneath the TAG hydrothermal field appears to be more than the inclusion size, the uplift profile is relatively insensitive to the exact location or shape of the serpentinized domain. Approximately 20% to 40% transformational strain is required to generate the observed uplift. Cracking associated with the expansion produced by the inferred serpentinization should generate a distinctive microseismic signature, which could be identifiable in the abundant ongoing microseismicity recorded in the TAG area [*deMartin et al*., 2007]. The rate of exothermic heat release needed to produce the serpentinized volume over

$\sim 10^5$ years is too small to significantly impact hydrothermal heat output at the TAG mound, except perhaps in the Low Temperature Zone (**Figure 4.2**) where it may contribute to ongoing diffuse flow.

On the other hand, application of the results to an uplift feature associated with the Kyushu-Palau subduction zone in the western Pacific, suggest that simple asymptotic solutions corresponding to a sphere or cylinder are not adequate. Approximately 3% transformational strain in an elliptically-shaped serpentinized region of the mantle wedge near the subducted Kyushu-Palau Ridge may result in the observed uplift on the Miyazaki Plain. The rate of serpentinization needed to produce the uplift is $\approx 8 \times 10^3$ kg/s, yielding fluid mass transfer rate of $\approx 10^3$ kg/s.

Transformation strain affects the stress field in and around the region undergoing serpentinization. Our analysis, based on the Coulomb stress approach, suggests that serpentinization at the footwall of a normal fault [*Francis*, 1981] tends to enhance fault slip and, in turn, fault slip may enhance the access of water required for the serpentinization reactions. Serpentinization of a region beneath the footwall of the TAG detachment fault tends to enhance the slip along some overlying normal faults, which may then result in fluid pathways to the deeper crust to continue the serpentinization process. Depending upon location, serpentinization at the hanging wall of a thrust fault, may result in serpentinization-related strengthening or weakening. Transformational strains associated with serpentinization underneath the Miyazaki Plain may promote thrust-type events in the aseismic slip zone near the upper boundary of the subducting Philippine Sea Plate.

Appendix 4A. Displacements in a half-space caused by cylindrical inclusion

The plain-strain distribution of dimensionless vertical, *w*, and horizontal, *u*, displacements in half-plane $y < 0$ with circular (cylindrical) inclusion (**Figure 4.4a**) are given by

$$\begin{cases} \dfrac{w}{a} = \dfrac{\varepsilon_0(1+\nu)}{6(1-\nu)}\left\{-\left(\dfrac{\eta+\eta_0}{R_1^{\,2}}\right)^{2-m} - (\eta+\eta_0)^{i-1} + \dfrac{(3-4\nu)(\eta-\eta_0)}{R_2^{\,2}} - \dfrac{2\eta[\xi^2-(\eta-\eta_0{}^2)^2]}{R_2^{\,4}}\right\} \\ \dfrac{u}{a} = \dfrac{\varepsilon_0(1+\nu)}{6(1-\nu)}\left\{\left(\dfrac{\xi}{R_1^{\,2}}\right)^{2-m} + \xi^{1-i} + \dfrac{(3-4\nu)\xi}{R_2^{\,2}} - \dfrac{4\xi\eta(\eta-\eta_0)}{R_2^{\,4}}\right\} \end{cases} \quad (4.A1)$$

where $R_1 = \sqrt{\xi^2+(\eta+\eta_0)^2}$, $R_2 = \sqrt{\xi^2+(\eta-\eta_0)^2}$, $m = 1$ and $m = 2$ in the inclusion exterior ($R_1 > 1$) and interior ($R_1 < 1$), respectively, $\xi = x/a$ and $\eta = y/a$ are the normalized, rectangular coordinates, and $\eta_0 = h/a$ is the dimensionless depth of the inclusion**.** Expressions (4.A1) are obtained as a particular case of *Ru*'s [1999] solution for an elliptical inclusion in half-plane (see also **Appendix 4B**) and agree with a more general solution for two adjacent half-planes with different elastic properties and a thermal, circular [*Aderogba and Berry*, 1971] or elliptical [*Ru* et al., 2001] inclusion in one of them. Substituting $\eta = 0$ in (4.A1), we have the distribution (4.4) of surface displacements. Note that in this appendix, parameters with dimension of length are normalized by the inclusion radius, *a*. This is different from the main text and, in particular, from expressions (4.4), where such parameters are normalized by the inclusion depth, *h*.

Appendix 4B. Displacements in a half-space with inclined elliptic inclusion

We use equation (4.7) with equation (4.5) to obtain displacements:

$$u + iw = -\frac{2\kappa\varepsilon_0}{\kappa+1}\{\overline{D(\overline{z})} - \overline{P(\overline{z})} + D(\overline{z}) - P(\overline{z}) - (z-\overline{z})[D'(\overline{z}) - P'(\overline{z})]\} \quad (4.B1)$$

This expression simplifies for the surface points where $y = 0$ and $z = \overline{z} = x$:

$$u + iw = 2\varepsilon_0[\overline{D(x)} - \overline{P(x)}] \quad (y = 0) \quad (4.B2)$$

To find functions $D(z)$ and $P(z)$, we write conformal mapping $\omega(\zeta)$ in equations (4.5) – (4.8) as finite sum of $N + 2$ terms:

$$z = \omega(\zeta) = \lambda\zeta + z_0 + \sum_{k=1}^{N}\frac{c_k}{\zeta^k} \quad (4.B3)$$

where $\zeta = \omega^{-1}(z)$, z_0 is a point located inside inclusion and designated as the inclusion "center", and λ, c_1, c_2, … are complex coefficients. Choosing $\omega(\zeta)$ in this form allows treating many practically-important inclusion shapes [e.g., *Muskhelishvili*, 1979]. Substituting $\zeta = \omega^{-1}(z)$ in equation (4.B3) and the result in equation (4.8) we have

$$D(z) = \frac{\overline{\lambda}}{\zeta} + \overline{z}_0 + \sum_{k=1}^{N}\overline{c}_k\zeta^k\ ,\ \zeta = \omega^{-1}(z) \quad (4.B4)$$

Because on the boundary, $|\zeta| = 1$, of the unit circle, $\overline{\zeta} = 1/\zeta$, on the inclusion boundary, $z = \omega(\zeta) = \omega(1/\overline{\zeta}) = \omega(1/\overline{\omega^{-1}(z)})$. Therefore, function $D(z)$, defined by equation (4.8), satisfies condition $D(z) = \overline{z}$ on the inclusion boundary. *Ru* [1999] used this condition to express *two* unknown stress functions through *one* auxiliary function $D(z)$ (equations (4.6) and (4.7)). To find $P(z)$, recall that this is the polynomial part of $D(z)$ at infinity, where $D(z)$ has a pole of degree N and can be represented as

$$D(z) = \sum_{n=-\infty}^{N} a_n z^n \tag{4.B5}$$

Here a_1, a_2, … are complex coefficients that are determined by substituting equations (4.B3) in equation (4.B5) and comparing coefficients for different powers of ζ. Equations (4.B3) and (4.B4) only slightly differ from those studied by *Ru* [1999] in the case of a real coefficient λ. Using complex λ enables convenient consideration of an inclined elliptical inclusion.

In the case of inclined elliptical inclusion, $N = 1$, $\lambda = e^{i\beta}(a+b)/2$, $c_1 = e^{i\beta}(a-b)/2$, and (4.B4) reduces to

$$D(z) = \frac{\overline{\lambda}}{\omega^{-1}(z)} + \overline{z}_0 + \overline{c}_1 \omega^{-1}(z) \tag{4.B6}$$

which is equivalent to $D(z)$ in equation (4.11) when $z_0 = -ih$ is the coordinate of the inclusion center.

As follows from the second equation in (4.10), or directly from (4.B3),

$$\omega^{-1}(z) = (z - ih)/\lambda + O(1/z) \quad (z \to \infty) \tag{4.B7}$$

Hence, per equation (4.8), $D(z)$ behaves at infinity as

$$D(z) = \overline{z_0} + \frac{\overline{c_1}}{\lambda}(z - z_0) + O\left(\frac{1}{z}\right) \quad (z \to \infty) \tag{4.B8}$$

and the polynomial $P(z)$ with the same behavior at $z \to \infty$ is defined by

$$P(z) = \overline{z_0} + \frac{\overline{c_1}}{\lambda}(z - z_0) \tag{4.B9}$$

This expression is identical to $P(z)$ in equation (4.11) for $z_0 = -ih$.

Substituting equations (4.B6) and (4.B7) into equation (4.B2), and taking into account that on the half-plane boundary $\overline{z} = z = x$, results in

$$u(x,0) + iw(x,0) = \frac{4ab}{a^2 - b^2}\varepsilon_0(1+\nu)e^{2i\beta}(x - \overline{z}_0)\left[1 - \sqrt{1 - \frac{e^{-2i\beta}(a^2 - b^2)}{(x - \overline{z}_0)^2}}\right] \quad \text{(4.B10)}$$

which is identical to equation (4.12), (4.14) when $z_0 = -ih$ (**Figure 4.5**).

Similar to (4.B2), stresses at the half-plane surface $y = 0$ can be obtained by substituting $z = \overline{z} = x$ in equations (4.5) – (4.7):

$$\sigma_{xx}(x,0) = \frac{8\mu}{3(\kappa+1)}\varepsilon_0(1+\nu)[D'(x) - P'(x) + \overline{D'(x)} - \overline{P'(x)}], \quad \sigma_{yy}(x,0) = 0, \quad \tau_{xy}(x,0) = 0 \quad \text{(4.B11)}$$

where

$$D'(x) - P'(x) = -\frac{2ab}{(x - z_0)^2}\left[1 - \frac{e^{-2i\beta}(a^2 - b^2)}{(x - ih)^2} + \sqrt{1 - \frac{e^{-2i\beta}(a^2 - b^2)}{(x - ih)^2}}\right]^{-1} \quad \text{(4.B12)}$$

Second and third expressions in equation (4.B11) simply show that the boundary conditions on the half-plane boundary $y = 0$ are satisfied, but the first one results in equation (4.13) when $z_0 = -ih$.

APPENDIX 4C. Correlation between Poisson Ratio and Serpentinization

Poisson's ratio is defined as the ratio between the radial contraction and the axial elongation a solid material is experiencing and theoretically ranges between 0 and 0.5. It can also be negative implying simultaneous contraction in all directions under compression (e.g., certain directions of single crystals as indicated by *Svetlov et al.* [1988]).

Compression wave velocities provide limited constraint on the crustal composition since many crustal rocks have similar velocities that may not be characteristics of just one type (e.g., *Birch* [1960, 1961]; *Christensen and Mooney* [1995]). Poisson's ratios providing valuable constraints on the composition of the oceanic or continental crust are therefore particularly important to determine.

A relationship between Poisson's ratio (σ) and compression wave velocity (V_p) and shear wave velocity (V_s) has been defined by *Christensen* [1996] for an isotropic medium as follows

$$\sigma = \frac{1}{2}\left[1 - \frac{1}{\left(\frac{V_p}{V_s}\right)^2 - 1}\right] \qquad (4.C1)$$

or alternatively the equation (4.C1) can be given

$$\sigma = \frac{\eta^2 - 2}{2(\eta^2 - 1)} \qquad (4.C2)$$

where $\eta = V_p / V_s$

As seen from the equation (4.C1) once the Poisson's ratio lies between 0 and 0.5, the ratio of V_p / V_s ranges from $\sqrt{2}$ to ∞ [*Christensen,* 1996].

However, rocks are aggregates of rock forming minerals and Poisson's ratios of rocks are related to the volume percentage of these minerals and their Poisson's ratios the determination of which is highly complicated due to anisotropic and often low-symmetric behavior of many common rocks (e.g., feldspars). Nevertheless many averaging methods (e.g., *Hashin and Shtrikman,* [1962]) have been developed to determine average seismic velocities for an aggregate of randomly oriented minerals, based on elastic constants of minerals. These velocities are then used to calculate Poisson's ratio of a rock.

Based on velocity measurements of 1875 cores taken from rock samples, *Christensen* [1996] tabulated the compression (V_p), shear velocities (V_s), and densities (ρ) for various common rock types at pressures up to 1 GPa. Among them serpentinite is reported to have a density of 2566 ± 50 kg/m^3, and a distribution of V_p / V_s ratios between 2.051 to 2.119 at increasing pressures from 200 to 1000 MPa. *Christensen* [1996] also provided Poisson's ratios at these pressures to show the pressure dependence of this property. These results for the serpentinite are summarized after *Christensen* [1996] on **Table 4C.1** that also demonstrated a slight increase in Poisson's ratio (σ) with increasing pressure.

Table 4C.1 Average values of V_p/V_s, and σ as a function of pressure and standard deviations

	200 MPa		400 MPa		600 MPa		800MPa		1000 MPa	
	V_p/V_s	σ	V_p/V_s	σ	V_p/V_s	σ	V_p/V_s	σ	V_p/V_s	Σ
Average	2.051	0.344	2.077	0.349	2.094	0.352	2.108	0.355	2.119	0.357
Standard Deviation	0.053	0.011	0.052	0.010	0.053	0.010	0.056	0.010	0.059	0.011

Along with *Rudnick and Fountain* [1995], *Christensen* [1996] concluded that temperature dependency has not been significant either for most of the rocks (e.g., gneiss, granite, eclogite, peridotite, dunite, etc.) as in the case of pressure dependence.

Among 29 analyzed different lithologies, the serpentinite is predicted to have the highest Poisson's ratio of 0.352 and is associated with a low compression wave velocity, whereas the average Poisson's ratio is calculated to be 0.27 [*Christensen,* 1996].

Hyndman and Peacock [2003] plotted the distribution of wave velocities (compression and shear) and Poisson's ratios for laboratory samples of serpentinized peridotite as a function of serpentinization degree [*Christensen,* 1966, 1978, 1996] under 1 GPa pressure (**Figure 4C.1**). Based on this figure they suggested the average V_p for a sample of 100% peridotite to be ~ 8.4 km/s which was consistent with the results of *Rudnick and Fountain* [1995] and *Christensen and Mooney* [1995] who used a more extensive compilation of unaltered ultramafic rocks. *Hyndman and Peacock* [2003] also suggested that the range of V_p between 7.2-7.6 km/s, which may be representative for

the forearc mantle, is associated with 15 to 30% of degree of serpentinization and a V_p value of only 5.1 km/s with 100% serpentinization.

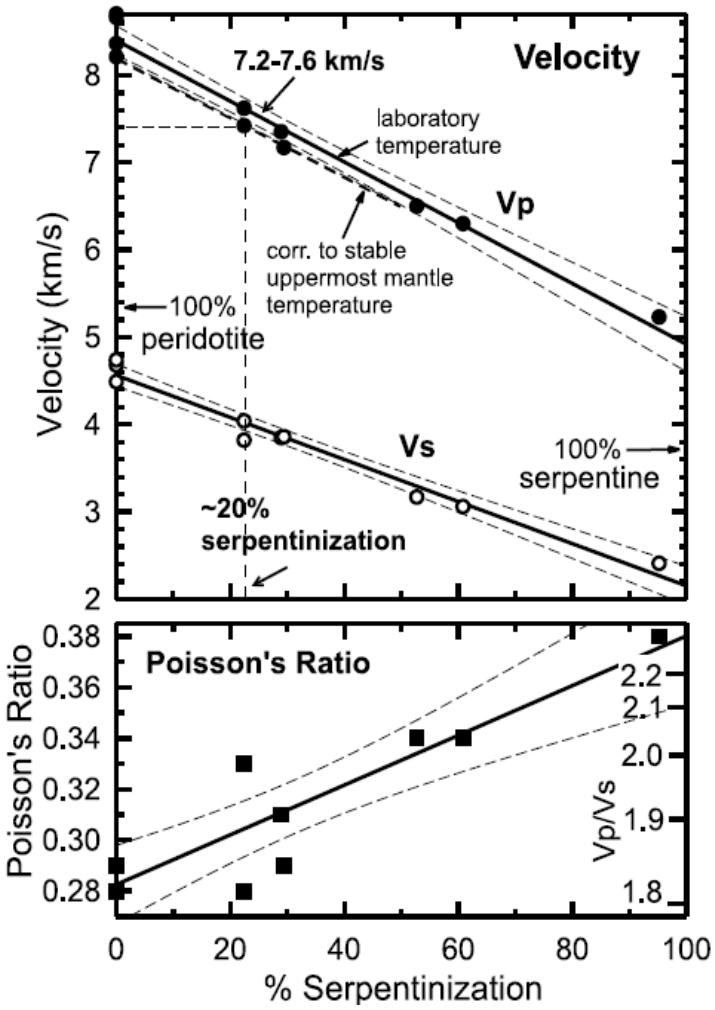

Figure 4C.1 V_p, V_s, and Poisson's ratios of laboratory mantle peridotite as a function of serpentinization degree [*Christensen,* 1966]. The best fit linear relations are also shown [*Hyndman and Peacock,* 2003].

Hyndman and Peacock [2003] observed that the Poisson's ratio may be diagnostic of two important factors:

(a) The degree of serpentinization: For instance in **Figure 4C.1**, the range of Poisson's ratio of 0.26-0.28 for unaltered peridotite increases to ~0.3 at 15% serpentinization and even to 0.38 at 100% serpentinization.

(b) The olivine composition: This dependency is explained by *Christensen* [1996] in a more detailed way.

Hyndman and Peacock [2003] also noted that at serpentinization degrees of 40% and over, the Poison's ratio for serpentinized mantle rocks is significantly higher than the ratio for mafic crustal rocks associated with a similar value of V_p. Such distinction is not observable though between the V_p and Poisson's ratio of unaltered mafic rocks and those of moderately hydrated mantle rocks at ~30% degree of serpentinization.

APPENDIX 4D. Possible Source of Water for Serpentinization

Based on geophysical imaging techniques (e.g., electrical conductivity, electrical resistivity, seismic tomography, etc.), sources of fluids could be mainly categorized into three groups in the Earth: (a) hydration and alteration of basalt at mid-ocean ridges, (b) dehydration of subducting slab in subduction zones, and (c) storage of water in hydrated olivine at high pressure and temperature in the mantle [*Kawakatsu and Watada,* 2007; *Kelbert et al.,* 2009; *Murakami et al.,* 2002; *Reyners et al.,* 2007; *Zhao et al.,* 1997] (**Figure 4D.1**).

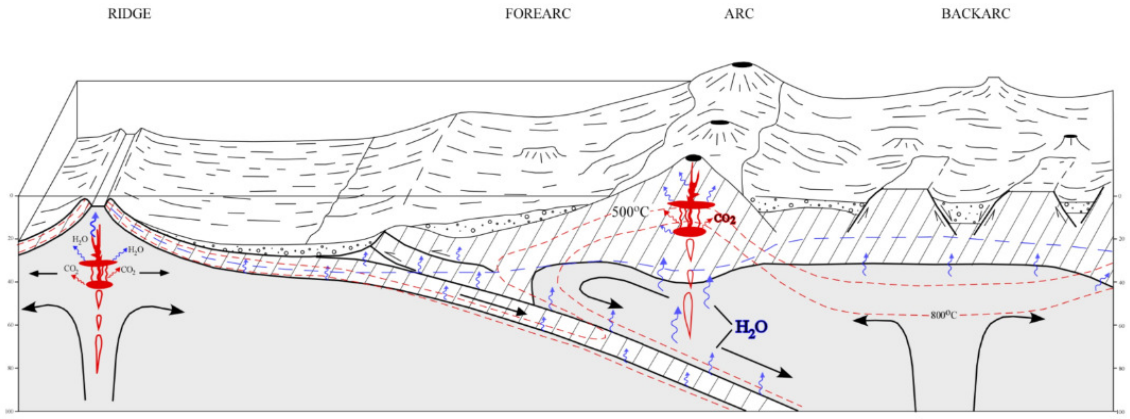

Figure 4D.1 A schematic image showing the ways and paths of fluid circulation through the mantle and its effect on physical Earth processes.

Significant volumes of aqueous fluids are expelled upward from subducting plates [e.g., *Anderson et al.,* 1976] as illustrated in **Figure 4D.2** by dehydration reactions in the subducting oceanic crust and sediments [*Anderson et al.,* 1976; *Peacock,* 1993; *Schmidt and Poli,* 1998] which contain free water in pore spaces and bound water in hydrous minerals. Such fluxes of these fluids were considered to be sufficient to hydrate

the forearc mantle entirely along tens of millions of years [e.g., *Peacock,* 1993; *Schmidt and Poli,* 1998; *Hyndman and Peacock,* 2003].

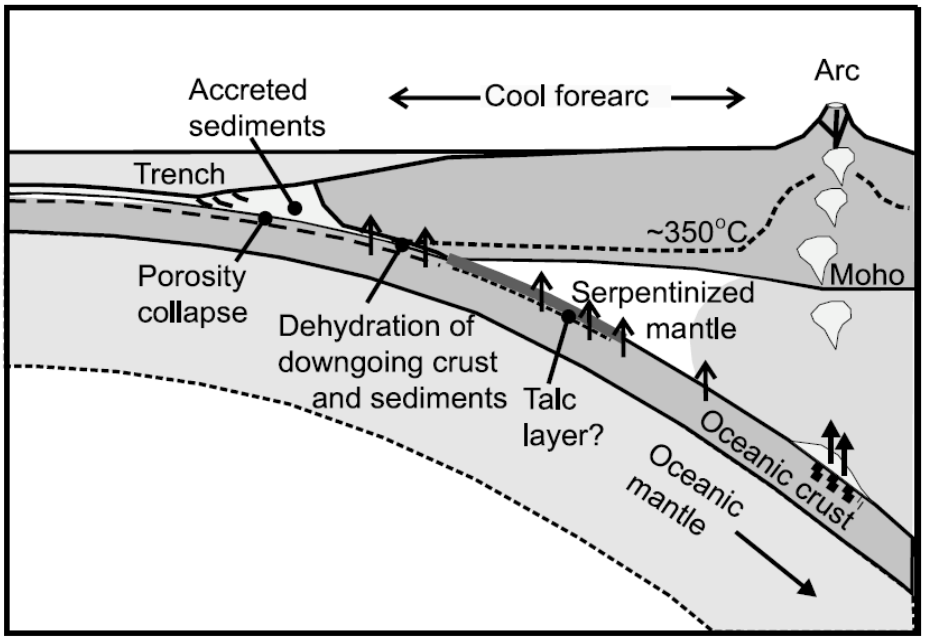

Figure 4D.2 Schematic cross section showing forearc mantle serpentinization due to aqueous fluid expulsion from subducting crust [*Hyndman and Peacock,* 2003].

In the upper oceanic crust, free water is released by compaction of sediments and closing of pores at relatively shallow depths. Whereas at higher depths (up to 200 km and more), progressive metamorphism of hydrous minerals produce fluids through dehydration reactions [e.g., *Peacock,* 1990; *Schmidt and Poli,* 1998]. With increasing depth, production of fluid is generally expected to decrease.

Fyfe and McBirney [1975] were the first to propose the serpentinization of forearc mantle to explain the uplift of coast trenches. In subduction zones, it is initiated once underlying subducting plate releases aqueous fluids rich in H_2O. These fluids then escape into the cool mantle above and hydrate minerals there to produce stable

serpentine and other hydrous minerals. Large volumes of fluids are released upward from the downgoing plate and overlying sediments as the pressure and temperature increases. Therefore physical and mechanical properties of the forearc mantle are significantly constrained by such hydrous minerals and serpentines that would possibly reduce seismic velocities or density and increase Poisson's ratio, electrical conductivity, or magnetization [*Hyndman and Peacock,* 2003].

Hyndman and Peacock [2003] plotted the distribution of fluid flux due to porosity collapse and dehydration reactions as a function of the distance from trench (**Figure 4D.3**). They estimated rates of fluid production as 0.1 mm/yr or 100 m/Myr and suggested the entire forearc mantle could be hydrated by water expelled from the subducting crust and overlying sediments during several tens of Myr. Fluid production rates according to them are mainly controlled by three factors:

(a) The convergence rate:

The rate with which water (free or bound) enters a subduction zone is nearly proportional to the convergence rate.

(b) The thickness of the forearc crust:

In continental subduction zones where the continental crust is thicker (e.g., N Japan and SW Japan), the subduction thrust intersects the forearc crust rather than forearc mantle and most of water is driven to the forearc crust to hydrate it.

(c) The amount of water in the downgoing crust and sediments

Although the amount of available H_2O undergoing chemical reactions with the forearc mantle minerals significantly constrains the degree of serpentinization, serpentinization of the mantle is predicted to be fracture-controlled and heterogeneous. In continental subduction zones where the temperatures are relatively higher (i.e., warm subduction zones), there are two competing factors affecting fluid penetration through fractures and channels [*Hyndman and Peacock,* 2003]:

(a) Faster reaction rates allowing more fluid penetration

(b) Less amounts of fluid available due to relatively thicker continental crust and associated less amount of fluid to dehydrate slab at greater depths

To make a first-order approximation, *Hyndman and Peacock* [2003] assumed sediment of 1000 m with a porosity of 50% to be under thrusting. In **Figure 4D.3**, *Hyndman and Peacock* [2003] showed that at shallow depths the amount of released water is approximately scaled with the thickness of subducted sediments (sections 1, 2, and 3 in **Figure 4D.3**). According to them, the volume of fluid released from the slab is not certain due to two competing factors which may affect the oceanic crust and overlying sediments. These processes are (a) possible fluid loss from free water expelled by porosity collapse and (b) fluid added into low-temperature hydrous minerals. Nevertheless, more than enough water is predicted to exist to entirely hydrate for both sediments and uppermost oceanic crust.

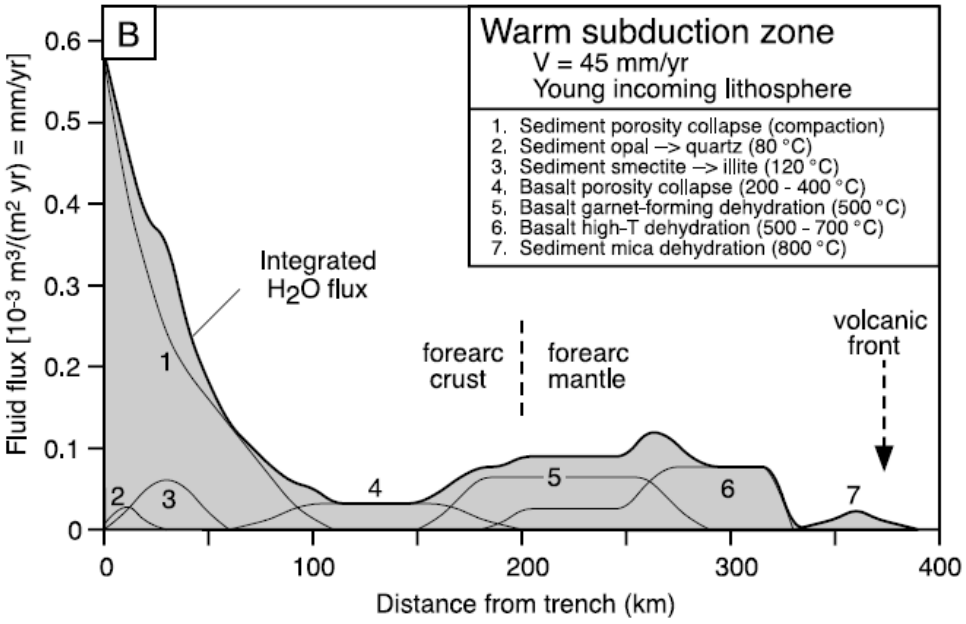

Figure 4D.3 Estimated fluxes of aqueous fluid released from subducted oceanic crust and sediments as function of distance from trench in a warm subduction zone (SW Japan).

Hyndman and Peacock [2003] concluded that in continental subduction zones H_2O, which is released from the subducted oceanic crust (sections 4, 5, 6 in **Figure 4D.3**), majorly occurs beneath the forearc crust through compaction and dehydration of subducted sediments.

4.8 References

Aderogba, K. V., and D. S. Berry (1971), Inclusions in a two-phase elastic space-plane circular and rectangular inclusions, *J. Mech. Phys. Solids, 19,* 285−293.

Agrinier, P., G. Cornen, and M. O. Beslier (1997), Mineralogical, and oxygen isotopic features of serpentinites recovered from the ocean/continent transition in the Iberia Abyssal Plain, Ocean Drilling Program Leg 149, *Scientific Results,* 541−552.

Allen, D. E., and W. E. Seyfried (2003), Serpentinization and heat generation: Constarints from Lost City and Rainbow hydrothermal systems, *Geochimica and Cosmochimica Acta, 68,* 1347−1354.

Anderson, R. N., S. Uyeda, and A. Miyashiro (1976), Geophysical and Geochemical Constraints at Converging Plate Boundaries—Part I: Dehydration in the Downgoing Slab, G*eophysical Journal of the Royal Astronomical Society, 44*(2), 333−357.

Berndt, M. E., D. E. Allen, and W. E. Seyfried Jr. (1996), Reduction of CO_2 during serpentinization of olivine at 300° C and 500 bar, *Geology, 24,* 351−354.

Birch, F. (1960), The velocity of compressional waves in rocks to 10 kilobars, *J. Geophys. Research, 56,* 66.

Birch, F. (1961), The velocity of compressional waves in rocks to 10 kilobars, part 2, *J. Geophys. Res, 66*(7), 2199−2224.

Blackman, D. K., J. A. Karson, D. S. Kelley, J. R. Cann, G. L. Früh-Green, J. S. Gee, S. D. Hurst, B. E. John, J. Morgan, S. L. Nooner, D. K. Ross, T. J. Schroeder, and E. A. Williams (2002), Geology of the Atlantis Massif (Mid-Atlantic Ridge, 30 degrees N): Implications for the evolution of an ultramafic oceanic core complex, *Marine Geophysical Researchers, 23,* 443−469.

Bohnenstiehl, D., and M. Kleinrock (2000), Fissuring near the TAG active hydrothermal mound, 26°N on the Mid-Atlantic Ridge, *Journal of Volcanology and Geothermal Research, 98*(1-4), 33−48.

Bonatti, E. (1976), Serpentinite protrusions in the oceanic crust, *Earth Planet. Sci. Lett., 32,* 107−113.

Bonatti, E., and P. R. Hamlyn (1981), Oceanic ultramafic rocks, in *The Sea,* vol. 7, edited by C. Emiliani, pp. 241−283, Wiley and Sons, New York.

Boschi C., G. L. Früh-Green, A. Delacour, J. A. Karson, D. S. Kelley (2006), Mass transfer and fluid flow during detachment faulting and development of an oceanic core complex, Atlantis Massif (MAR 30°N), *Geochemistry Geophysics Geosystems, 7,* 1–39.

Bougault, H., J. L. Charlou, Y. Fouquet, H. D. Needham, N. Vaslet, P. Appriou, P. J. Baptiste, P. A. Rona, L. Dmitriev, and S. Silantiev (1993), Fast and slow spreading ridges: Structure and hydrothermal activity, ultramafic topographic highs, and CH4 output, *Journal of Geophysical Research, 98*(B6), 9643–9651.

Buck, W. R. (1988), Flexural rotation of normal faults, *Tectonics, 7*(5), 959–973.

Byerlee, J. (1978), Friction of rocks, *Pure and Applied Geophysics, 116*(4), 615–626, doi:10.1007/BF00876528.

Canales, J. P., R. A. Sohn, and B. J. deMartin (2007), Crustal structure of the Trans-Atlantic Geotraverse (TAG) segment (Mid-Atlantic Ridge, 26°10′N): Implications for the nature of hydrothermal circulation and detachment faulting at slow-spreading ridges, *Geochecm., Geophys., Geosys., 8*(8), 18 pp., Q08004, doi:10.1029/2007GC001629.

Cann, J. R., D. K. Blackman, D. K. Smith, E. McAllister, B. Janssen, S. Mello, E. Averinos, A. R. Pascoe, and J. Escartin (1997), Corrugated slip surfaces formed at ridge-transform intersections on the Mid-Atlantic Ridge, *Nature, 385,* 329–332.

Cannat, M. (1993), Emplacement of mantle rocks in the sea floor at mid-ocean ridges, *J. Geophys. Res., 98,* 4163–4172.

Cannat, M., D. Bideau, and H. Bougalt (1992), Serpentinized peridotites and gabbros in the Mid-Atlantic Ridge axial valley at 15°37′N and 16°52′N, *Earth Planet. Sci. Lett., 109,* 87–106.

Cannat, M., C. Mével, M. Maia, C. Deplus, C. Durand, P. Gentle, P. Agrinier, A. Belarouchi, G. Dubuisson, E. Humler, and J. Reynolds (1995), Thin crust, ultramafic exposures, and rugged faulting patterns at the Mid-Atlantic Ridge (22°-24°N), *Geology, 23,* 49–52.

Cannat, M., Y. Lagebrielle, H. Bougault, J. Casey, N. de Coutures, L. Dmitriev, and Y. Fouquet (1997), Ultramafic and gabbroic exposures at the Mid-Atlantic Ridge: Geological mapping in the 15°N region, *Tectonophysics, 279,* 193–213.

Carlson, R. L., and D. J. Miller (1997), A new assessment of the abundance of serpentinite in the oceanic crust, *Geophysical Research Letters, 24,* 457–460.

Chanpura, R. A. and L. N. Germanovich (2004), *Fault stability inside and near a depleting petroleum reservoir,* in Proceedings (compact disk) of 6th North American Rock Mechanics Symposium (NARMS): Gulf Rocks 2004, American Rock Mechanics Association, Alexandria, VA.

Christensen, N. I. (1966), Elasticity of ultrabasic rocks, *Journal of Geophysical Research, 71*(24), 5921−5931.

Christensen, N. I. (1978), Ophiolites, seismic velocities and oceanic crustal structure, *Tectonophysics, 47*(1-2), 131−157.

Christensen, N. I. (1996), Poisson's ratio and crustal seismology, *Journal of Geophysical Research, 101,* 3139−3156.

Christensen, N. I., and W. D. Mooney (1995), Seismic velocity structure and composition of the continental crust: A global view, *Journal of Geophysical Research, 100,* 9761−9788.

Cocco, M., and J. R. Rice (2002), Pore pressure and poroelasticity effects in Coulomb stress analysis of earthquake interactions, *J. Geophys. Res., 108*(B2), doi.10.1029/2002JB002319.

Coleman, R. G. (1971), Petrologic and geophysical nature of serpentinites, *Geol. Soc. Amer. Bull., 82,* 918−987.

Davies, J. H. (2003), Elastic field in a semi-infinite solid due to thermal expansion or a coherently misfitting inclusion, *Journal of Applied Mechanics-Transaction of the ASME, 70,* 655−660.

deMartin, B. J. (2007), Experimental and seismological constraints on the rheology, evolution, and alteration of the lithosphere at oceanic spreading centers, Ph.D. thesis, MIT-WHOI Joint Program.

deMartin, B. J., R. A. Sohn, J. P. Canales, and S. E. Humphris (2007), Kinematics and geometry of active detachment faulting beneath the Trans-Atlantic Geotraverse (TAG) hydrothermal field on the Mid-Atlantic Ridge, *Geology, 35,* 711−714.

Detournay, E. and A. H. D. Cheng (1993), *Fundamentals of poroelasticity,* Chapter 5, in *Comprehensive Rock Engrg.,* vol. 2, edited by J. Hudson, pp. 113−169, Pergamon Press, Oxford, England.

Dick, H. J. B., A. D. Saunders (Eds.), and M. J. Norry (Eds.) (1989), Abyssal peridotites, very slow spreading ridges and ocean ridge magmatism, *Magmatism in the ocean basins: Geological Society, London, Special Publication, 24,* 71−105.

Dyskin, A., L. Germanovich, and K. Ustinov (2000), Asymptotic analysis of crack interaction with free boundary, *International Journal of Solids and Structures, 37*(6), 857−886.

Dziak, R. P., C. G. Fox, R. W. Embley, J. L. Nabelek, J. Braunmiller, R. A. Koski (2000), Recent tectonics of the Blanco ridge, Eastern Blanco Transform Fault zone, *Marine Geophysical Researchers, 21,* 423−450.

Escartin, J., and M. Cannat (1999), Ultramafic exposures and the gravity signature of the lithosphere near the Fifteen-Twenty Fracture Zone (Mid-Atlantic Ridge, 14°-16.5°N), *Earth and Planetary Science Letters, 171,* 411−424.

Escartin, J., G. Hirth, and B. Evans (1997a), Nondilatant brittle deformation of serpentinites: Implications for Mohr-Coulomb theory and the strength of faults, *Journal of Geophysical Research, 102*(B2), 2897−2913.

Escartin, J., G. Hirth, and B. Evans (1997b), Effects of serpentinization on the Lithospheric strength and the style of normal faulting at slow-spreading ridges, *Earth and Planetary Science Letters, 151*(3), 181−189.

Escartin, J., G. Hirth, and B. Evans (2001), Strength of slightly serpentinized peridotites: Implications for the tectonics of oceanic lithosphere, *Geology, 29,* 1023−1026.

Faccenda, M., L. Burlini, T. V. Gerya, and D. Mainprice (2008), Fault-induced seismic anisotropy by hydration in subducting oceanic plates, *Nature, 455*(7216)*,* 1097−1100.

Francis, T. J. G. (1981), Serpentinization faults and their role in the tectonics of slow spreading ridges, *J. Geophys. Res., 86,* 11612−11622.

Früh-Green G. L., A. Plas, and C. Lecuyer (1996), Petrologic and stable isotope constraints on hydrothermal alteration and serpentinization of the EPR shallow mantle at Hess Deep (site 895), *Proc. Ocean Drilling Program Sci. Results, 147,* 255−291.

Fryer, P. (1996a), Evolution of the Mariana convergent plate margin system, *Rev. Geophys., 34,* 89−125.

Fryer, P. (1996b), An actively venting serpentine seamount on the southeastern Mariana forearc: “Shinkai 6500” Dives 280 and 281, *Jamstec J. Deep Sea Res., 12,* 247−256.

Fryer, P. and M. J. Mottl (1992), Lithology, mineralogy, and origin of serpentine muds recovered from Conical and Torishima forearc seamounts: Results from Leg 135

drilling, in Fryer, P., J. A. Pearce, J. B. Stokking, et al., *Proc. Ocean Drilling Program Sci. Results, 125,* 343−362.

Fyfe, W. S., and P. Londsale (1981), Ocean floor hydrothermal activity, in *The Sea*, vol. 7, *The Oceanic Lithosphere*, edited by C. Emiliani, pp. 589−638, Wiley and Sons, New York.

Fyfe, W. S., and A. R. McBirney (1975), Subduction and the structure of andesitic volcanic belts, *Am. J. Sci, 275*(1), 285−297.

Gillis, K., C. Mével, and J. Allan (1993), Proc. ODP Initial Rept., 147, 366 pp., Ocean Drilling Program, College Station, TX.

Goodier, J. N. (1937), On the integration of the thermo-elastic equations, *Philosophical Magazine, 23,* 1017−1032.

Hashin, Z., and S. Shtrikman (1962), A variational approach to the theory of the effective magnetic permeability of multiphase materials, *Journal of Applied Physics, 33*(10), 3125−3131.

Hilairet N., B. Reynard (2009), Stability and dynamics of serpentinite layer in subduction zone, *Tectonophysics, 465,* 24−29.

Hirauchi, K., I. Katayama, S. Uehara, M. Miyahara, and Y. Takai (2010), Inhibition of subduction thrust earthquakes by low-temperature plastic flow in serpentine, *Earth and Planetary Science Letters, 295,* 349−357.

Hyndman, R. D., and S. M. Peacock (2003), Serpentinization of the forearc mantle, *Earth and Planetary Science Letters, 212*(3-4), 417−432.

Hyndman, R. D., K. Wang and M. Yamano (1995), Thermal constraints on the seismogenic portion of southwestern Japan subduction thrust, *J. Geophys. Res., 100,* 15373−15792.

Hyndman, R. D., M. Yamano, and D. A. Oleskevitch (1997), The seismogenic zone of subduction thrust faults, *Island Arc, 6,* 244−260.

Ildefonse, B., D. K. Blackman, B. E. John, Y. Ohara, D. J. Miller, and C. J. MacLeod (2007), Oceanic core complexes and crustal accretion at slow-spreading ridges, *Geology, 35,* 623−626.

Jaeger, J. C., N. G. W. Cook, and R.W. Zimmerman (2007), Fundamentals of Rock Mechanics, 4th Edition, 475 pp., Blackwell Publishing, Oxford, England.

Janecky, D. R., and W. E. Seyfried Jr. (1986), Hydrothermal serpentinization of peridotite within the oceanic crust: Experimental investigations of mineralogy and major element chemistry, *Geochim. Cosmochim. Acta, 50,* 1357−1378.

Jaswon, M. A, and R. D. Bhargava (1961), Two-dimensional elastic inclusion problems, *Proc. Camb. Phil. Soc., 57,* 669−680.

Kamata, H., and K. Kodama (1999), Volcanic history and tectonics of the southwest Japan arc, *Island Arc, 8*(3), 393−403.

Karson, J. A., and R. M. Lawrence (1997), Tectonic setting of serpentinite exposures on the western median valley wall of the MARK Area in the vicinity of Site 920, J. A. Karson, M. Cannat, D. J. Miller, and D. Elthon (Eds.), *Proc. Ocean Drilling Program Sci. Results, 153,* 5−21.

Karson, J. A., and P. A. Rona (1990), Block-tilting, transfer faults, and structural control of magmatic and hydrothermal processes in the TAG area, Mid-Atlantic Ridge 26°N, *Geological Society of America Bulletin, 102,* 1635−1645.

Kawakatsu, H., and S. Watada (2007), Seismic evidence for deep-water transportation in the mantle, *Science, 316*(5830), 1468−1471.

Kelbert, A., A. Schultz, and G. Egbert (2009), Global electromagnetic induction constraints on transition-zone water content variations, *Nature, 460*(7258), 1003−1006.

King, G. C. P., R. S. Stein, and J. Lin (1994), Static stress changes and the triggering of earthquakes, *Bulletin of the Seismological Society of America, 84*(3), 935−953.

Kirby, S., E. R. Engdahl, and R. Denlinger (1996), Intermediate-depth intraslab earthquakes and arc volcanism as physical expressions of crustal and uppermost mantle metamorphism in subducting slabs, *Geophysical Monograph, 96,* 195−214.

Lalou, C., J. L. Reyss, E. Brichet, P. A. Rona, and G. Thompson (1995), Hydrothermal activity on a 10^5-year scale at a slow-spreading ridge: TAG area, Mid-Atlantic Ridge, *J. Geophys. Res, 100,* 17855−17862.

Lister, G. S., M. A. Etheridge, and P. A. Symonds (1986), Detachment faulting and the evolution of passive continental margins, *Geology, 14*(3), 246−250, doi:10.1130/0091-7613.

Lowell, R. P., and P. A. Rona (2002), Seafloor hydrothermal systems driven by sepentinization of peridotite, *Geophys. Res. Letters, 29*, 11, doi:10.1029/2001GL014411.

Macdonald, A. H., and W. S. Fyfe (1985), Rate of serpentinization in seafloor environments, *Tectonophysics, 116,* 123−135.

Macleod, C. J., R. C. Searle, B. J. Murton, J. F. Casey, C. Mallows, S. C. Unsworth, K. L. Achenbach, and M. Harris (2009), Life cycle of oceanic core complexes, *Earth and Planetary Science Letters, 287,* 333−344.

Matsubara, M., K. Obara, and K. Kasahara (2008), Three-dimensional P- and S-wave velocity structures beneath the Japan Islands obtained by high-density seismic stations by seismic tomography, *Tectonophysics, 454*(1-4), 86−103.

Mavko, G., T. Mukerji, and J. Dvorkin (2003), The Rock Physics Handbook: Tools for Seismic Analysis of Porous Media, Cambridge Univ. Press, Cambridge, England.

McTigue, D. (1987), Elastic stress and deformation near a finite spherical magma body: resolution of the point source paradox, *J. Geophys. Res., 92*(B12), 12931−12940.

Mével, C., and C. Stamoudi (1996), Hydrothermal alteration of the upper-mantle sections at Hess Deep, *Proc. Ocean Drilling Program Sci. Results, 147,* 293−309.

Mével, C. (2003), Serpentinization of abyssal peridotites at mid-ocean ridges, *Comptes Rendus Geoscience, 335,* 825−852.

Mindlin, R. D., D. H. Cheng (1950), Thermoelastic stress in the semi-infinite solid, *Journal of Applied Physics, 21,* 931−933.

Miranda, E. A., and Y. Dilek (2010), Oceanic Core Complex development in modern and ancient oceanic lithosphere: Gabbro-localized versus peridotite-localized detachment models, *Journal of Geology, 118,* 95−109.

Mogi, K. (1958), Relations between the eruptions of various volcanoes and the deformations of the ground surfaces around them, *Bulettin of the Earthquake Research Institute, 36,* 99−134.

Mottl, M. J., S. C. Komor, P. Fryer, and C. L. Moyer (2003), Deep-slab fuel extremophilic Archaea on a Mariana forearc serpentinite mud volcano: Ocean Drilling Program Leg 195, *Geochemistry Geophysics Geosystems, 4*(11), 9009.

Murakami, M., K. Hirose, H. Yurimoto, S. Nakashima, and N. Takafuji (2002), Water in Earth's lower mantle, *Science, 295*(5561), 1885−1887.

Muskhelishvili, N. I., 1979, *Some Basic Problems of the Mathematical Theory of Elasticity,* 768 pp., Noordhoff, Leyden, Netherlands.

Nagaoka, S., H. Maemoku, and Y. Matsushima (1991), Evolution of Holocene coastal landforms in the Miyazaki Plain, Southern Japan, *Quat. Res. (Jpn.), 30,* 59−78.

Nakada, M., M. Tahara, H. Shimizu, S. Nagaoka, K. Uehira, and S. Suzuki (2002), Late Pleistocene crustal uplift and gravity anomaly in the eastern part of Kyushu, Japan, and its geophysical implications, *Tectonophysics, 351,* 263−283.

Nicolas, A. (1989), Structure of ophiolite and dynamics of ocean lithosphere, 367 pp., Kluwer Academic Publishers, Dordrecht, Netherlands.

Nowacki, W. (1986), *Thermo-Elasticity,* 2nd edition, Pergamon Press, Oxford, England.

O'Hanley, D.S. (1992), Solution to the volume problem in serpentinization, *Geology, 20,* 705−708.

Palmer, M. R. (1996), Hydration and uplift of the oceanic crust on the Mid-Atlantic Ridge associated with hydrothermal activity: Evidence from boron isotopes, *Geophysical Research Letters, 23,* 3479−3482.

Peacock, S. M. (1990), Numerical simulation of metamorphic pressure-temperature-time paths and fluid production in subducting slabs, *Tectonics, 9*(5), 1197−1211.

Peacock, S. M. (1993), Large-scale hydration of the lithosphere above subducting slabs, *Chemical Geology, 108*(1-4), 49−59.

Pinto, F., and A. Whittle (2006), Discussion of "Elastic solution for tunneling-induced ground movements in clays" by K. H. Park, *International Journal of Geomechanics, 6,* 72.

Puzrin, A. M., J. B. Burland, J. R. Standing (2012), Simple approach to predicting ground displacements caused by tunnelling in undrained anisotropic elastic soil, *Geotechnique, 62*(4), 341.

Reston, T. J. (2009), The structure, evolution, and symmetry of the magma-poor rifted margins of the North and Central Atlantic: A synthesis, *Tectonophysics, 468,* 6−27.

Reyners, M., D. Eberhart-Phillips, and G. Stuart (2007), The role of fluids in lower-crustal earthquakes near continental rifts, *Nature, 446*(7139), 1075−1078.

Rona, P. A. (2008), The changing vision of marine minerals, *Ore Geology Reviews, 33,* 618−666, doi:10.1016/j.oregeorevv.2007.03.006.

Rona, P. A., L. Widenfalk, and K. Bostrom (1987), Serpentinized ultramafics and hydrothermal activity at the Mid-Atlantic Ridge crest near 15°N, *J. Geophys. Res., 92*(B2), 1417−1427.

Rona, P. A., M. D. Hannington, C. V. Raman, and G. Thompson (1993), Active and relict seafloor hydrothermal mineralization at the TAG hydrothermal field, Mid-Atlantic Ridge, *Econ. Geology, 88,* 1989−2017.

Ru, C. Q. (1999), Analytic solution for Eshelby's problem of an inclusion of arbitrary shape in a plane and half-plane, *Journal of Applied Mechanics, 66,* 315−322.

Ru, C. Q., P. Schiavone, and A. Mioduchowski (2001), Elastic fields in two jointed half-planes with an inclusion of arbitrary shape, *J. Appl. Math. Phys., 52,* 18–32.

Rudnick, R. L., and D. M. Fountain (1995), Nature and composition of the continental crust: a lower crustal perspective, *Reviews of Geophysics, 33*(2), 241−265.

Rudnicki, J. W., G. Vouille (Eds.) and P. Berest (Eds.) August 25-28 (1999), Alteration of regional stress by reservoirs and other inhomogeneities: stabilizing or destabilizing?, in *Proceedings of the 9th International Congress on Rock Mechanics,* vol. 3, 1629−1637*,* Paris, France.

Rüpke, L. H., J. P. Morgan, M. Hort , and J. A. D. Connolly (2004), Serpentine and the subduction zone water cycle, *Earth Planet. Sci. Lett., 223,* 17−34.

Ryder, I., A. Rietbrock, K. Kelson, R. Bürgmann, M. Floyd, A. Socquet, C. Vigny, and D. Carrizo (2012), Large extensional aftershocks in the continental forearc triggered by the 2010 Maule earthquake, Chile*, Geophys. J. Int., 1365*(246), doi:10.1111/2011.05321.

Saiga, A., S. Matsumoto, K. Uehira, T. Matsushima, and H. Shimizu (2010), Velocity structure in the crust beneath the Kyushu area, *Earth, Planets, and Space, 62*(5)*,* 449−462.

Salah, M. K. and T. Seno (2008), Imaging V_p, V_s, and Poisson's ratio anomalies beneath Kyushu, southwest Japan: Implications for volcanism and forearc mantle wedge serpentinization, *J. Asian Earth Sci., 31,* 408−428.

Schmidt, M. W., and S. Poli (1998), Experimentally based water budgets for dehydrating slabs and consequences for arc magma generation, *Earth and Planetary Science Letters, 163*(1), 361−379.

Segall, P. (2010), Earthquake and Volcano Deformation, Princeton Univ. Press, Princeton, N.J.

Segall, P., and S. D. Fitzgerald (1998), A note on induced stress changes in hydrocarbon and geothermal reservoirs, *Tectonophysics, 289,* 117−128.

Seno, T. (2005), Variation of downdip limit of the seismogenic zone near the Japanese islands: Implications for the serpentinization mechanism of the forearc mantle wedge, *Earth and Planetary Science Letters, 231*(3-4), 249−262.

Seno, T., and S. Maruyama (1984), Paleographic reconstruction and origin of the Philippine Sea, *Tectonophysics*, 102, 53−84.

Seno, T., and T. Yamasaki (2003), Low-frequency tremors, intraslab and interplate earthquakes in Southwest Japan — from a viewpoint of slab dehydration, *Geophys. Res. Lett., 30*(22), 2171.

Shimoyama, S., H. Kinoshita, M. Miyahara, Y. Tanaka, T. Ichihara, and K. Takemura (1999), Mode of vertical crustal movements during the Late Quaternary in Kyushu, Japan, deduced from heights of ancient shorelines, *Tectonophysics, 302,* 9−22.

Skelton, A., and M. Jakobsson (2007), Could peridotite hydration reactions have provided a contributory driving force for Cenozoic uplift and accelerated subsidence along the margins of the North Atlantic and Labrador Sea?, *Norwegian Journal of Geology, 87,* 21−28.

Smith, B., and D. Sandwell (2003), Coulomb stress accumulation along the San Andreas Fault system, *J. Geophys. Res, 108*(B6), 2296, doi:10.1029/2002JB002136.

Steacy, S., S. S. Nalbant, J. McCloskey, C. Nostro, O. Scotti, and D. Baumont (2005), Onto what planes should Coulomb stress perturbations be resolved?, *J. Geophys. Res, 110,* 1−14, B05S15., doi:10.1029/2004JB003356.

Svetlov, I., A. Epishin, A. Krivko, A. Samoilov, I. Odintsev, and A. Andreev (1988), Anisotropy of Poisson's ratio of single crystals of nickl alloy, *Soviet Physics Doklady, 33,* 771.

Tahara, M., K. Uehira, H. Shimizu, M. Nakada, T. Yamada, K. Mochizuki, M. Shinohara, M. Nishino, R. Hino, and H. Yakiwara (2008), Seismic velocity structure around the Hyuganada region, Southwest Japan, derived from seismic tomography using land and OBS data and its implications for interplate coupling and vertical crustal uplift, *Physics of the Earth and Planetary Interiors, 167,* 19−33.

Timoshenko, S. P., and J. N. Goodier (1970), Theory of Elasticity, 3rd edition, McGraw-Hill, New York.

Tucholke, B. E., and J. Lin (1994), A geological model for the structure of ridge segments in slow-spreading ocean crust, *J. Geophys. Res., 99*(B6), 11937−11958.

Tucholke, B. E., J. Lin, M. C. Kleinrock (1998), Megamullions and mullion structure defining oceanic metamorphic core complexes on the mid-Atlantic ridge, *Journal of Geophysical Research-Solid Earth, 103,* 9857−9866.

Yagi, Y., and M. Kikuchi (2003), Partitioning between seismogenic and aseismic slip as highlighted from slow slip events in Hyuga-nada, Japan*, Geophys. Res. Lett., 30*(2), 1087−1091, doi:10.1029/2002GL015664.

Wheat, C. G., P. Fryer, A. T. Fischer, S. Hulme, H. Jannasch, M. J. Mottl and K. Becker (2008), Borehole observations of fluid flow from South Chamorro Seamount, an active serpentinite mud volcano in the Mariana forearc, *Earth and Planetary Science Letters, 267,* 401−409.

Zhao, D., Y. Xu, D. A. Wiens, L. R. Dorman, J. Hildebrand, and S. Webb (1997), Depth extent of the Lau back-arc spreading center and its relation to subduction processes, *Science, 278*(5336), 254.

Zonenshain, L. P., M. I. Kuzmin, A. P. Lisitsin, Y. A. Bogdanov, and B. V. Baranov (1989), Tectonics of the Mid-Atlantic rift-valley between the TAG and MARK areas (26-24-degrees-N) — Evidence for vertical tectonism, *Tectonophysics, 159,* 1−23.

CHAPTER 5

CONCLUSIONS AND RECOMENDATIONS

5.1 Conclusions

This dissertation is focused on three important subjects at mid-ocean ridges: (a) development of sub-sea heat flow measuring tools, (b) heat and geochemical flux characterization at Juan de Fuca Ridge (JdF), and (c) modeling the deformation and surface uplift associated with subsurface serpentinization of mantle peridotites. Here we summarize our main results as follows:

1. We built and calibrated three unique devices to make direct measurements of focused and diffuse fluid flow and advective heat output on the seafloor. Such measurements are crucial for providing constraints on the physics of seafloor hydrothermal processes which are globally linked to magmatic and tectonic processes and biological ecosystems at mid-ocean ridges. Successful field deployments from deep submergence vehicle *Alvin* on multiple dives between July 2008 and July 2010, showed that the instruments operated reliably over two-order of magnitude range of hydrothermal fluid flow rate between 2 and 200 cm/s, which are typically encountered at various diffuse and focused venting environments along oceanic spreading centers. Being robust, relatively small, lightweight, easy and quick to operate with both for discrete and diffuse venting regimes (high- and low-temperature), they have

proven to fill an important gap in the studies of fluid flow and advective heat transfer and their quantification through existing tools and methods.

2. We deployed these flow measuring devices during the July 2008 (AT15-34), August 2008 (AT15-36), June 2009 (AT15-47), and July 2010 (AT15-67) expeditions to JdF. The measurements we performed in the Mothra and High Rise hydrothermal vent fields yielded the first estimates on this portion of the Endeavour segment, despite several decades of intensive study of Endeavour Ridge. Our reported database of 58 direct estimates of fluid velocity and heat flux yielded a total combined (high and low-temperature) heat output of 579 MW. At most, 21% of this output could be associated with high-temperature venting for the Main Endeavour vent field, based on a simple extrapolation and suggested that the high-temperature heat output may be declining after the 1999 eruption. In High Rise on the other hand, the value of total focused high-temperature heat output has escalated to 448 MW that is higher than that estimated from MEF.
3. Another important result of this dissertation is that it also reports first estimates of geochemical flux of some volatile compounds (H_2, CH_4 and $CO_{2(aq)}$) from focused and diffuse flows in the MEF and Mothra vent fields along the Endeavour segment by coupling our fluid flow measurement estimates with those from in-situ geochemical measurements. The geochemical flux from diffuse flows which significantly constrains subsurface

microbial activity is shown to represent at least half of the net geochemical flux.

4. We developed a new mathematical model of structural deformation and surface uplift due to subsurface serpentinization of distinctly shaped and aligned ultramafic inclusions. We used scaling for simple inclusion shapes such as sphere or cylinder and closed-form solutions for an elliptical inclusion of various orientation and aspect ratio undergoing homogeneous transformation strain in an elastic half-space and reported all relevant equations in detail. Our results showed that surface uplift does not recognize the shape of the intrusion if it is located at depths > ~ 1.5x the radius of the inclusion. We have also generically applied our model to two cases of topographic surface anomalies; one at the TAG hydrothermal field on the Mid-Atlantic Ridge and the other at the Miyazaka Plain above the Kyushu-Palau subduction zone in the western Pacific respectively. We suggested that the former feature might have been resulted from a deep serpentinized inclusion which is located beneath the footwall of a detachment fault and subjected to a transformation strain of 20 to 40%. Whereas the latter uplift on the Miyazaki Plain may be associated with an elongated subsurface serpentinized inclusion undergoing a transformation strain of only 2%. Careful interpretation of such topographic surface features is of critical importance to assess processes occurring at crustal depths and hence to

understand the link between serpentinization and magmatic, tectonic, and hydrothermal processes at mid-ocean ridges.

5.2 Recommendations for future work

Our recommendations for future work on the measurement and characterization of heat output at mid-ocean ridge hydrothermal sites include:

1. As yet, none of our devices incorporates electronic recording mechanisms, cameras, or internal temperature or chemical sensors. While this simplicity provides some serious advantages for determining fluid flow estimates, data recovery from video is labor intensive. Moreover, measuring temperature directly would allow an alternative way of measuring flow rate of heat loss. This way, heat flow rate could be determined by various means and cross-checks between redundant measurements may be done.
2. Determination of heat or chemical flux also requires temperature as well as the discharge area be determined independently. However estimating the size of areas of diffuse venting heavily relies on the observation of either biota or biological communities. The milieus associated with less colonization of such communities might be challenging to identify even though they may be awash by diffuse flow. Finding new means for estimating areas of diffuse flow zones could help diffuse heat output database grow faster.
3. In their present configuration, these devices cannot be used for remote data collection or long-term deployment instead, they provide instantaneous heat outputs. Obtaining time-series of heat flow data at the same site over a

certain prolonged amount of time could provide an understanding of a time scale over which flow rates may fluctuate at mid-ocean ridges.

4. Restricted number of heat flow measurements completed along the mid-ocean ridge systems up to date would heavily promote routine uses of our devices which are easy to navigate with on a regular dive, even on our absence on research vessels.
5. Extensive effort needs to be allocated for heat flow measurement studies in order to obtain a good distribution and significant amount of data. Such data could benefit from comparisons with estimates obtained through other measuring techniques or tools.

Our recommendations for future work on serpentinization-assisted deformation processes at mid-ocean ridge hydrothermal sites and subduction zones include:

1. By triggering multiple faulting and/or fracturing processes - inside or outside the serpentinized inclusions - at significantly less transformation strains (e.g., several percent) when compared to those required for massive serpentinization, serpentinization may result in the development of detachment faults or permeability paths, or assist water flow necessary for serpentinization reactions.
2. Although the surface uplift may not provide constraints on the geometry of the serpentinized inclusion at depths > ~ 1.5x the radius of the inclusion, the

pattern of faulting or fracturing can indicate the location and shape of the subsurface inclusion.